Role of sub-stoichiometric carbon content on the structural, thermal and electrochemical properties of TaC_x

A Thesis
Submitted in partial fulfilment of the
requirements for the award of degree of

DOCTOR OF PHILOSOPHY

by

Loveleen Kaur Brar
(Regn. No.: 951212001)

Under the Guidance of

Dr. O. P. Pandey
(Senior Professor)

School of Physics and Materials Science
Thapar University, Patiala-147004

(February-2017)

Declaration

I hereby certify that the work which is presented in thesis entitled ***"Role of sub-stoichiometric carbon content on the structural, thermal and electrochemical properties of TaC_x"*** in the partial fulfilment of the requirement for the award of the degree of DOCTOR OF PHILOSOPHY in the School of Physics and Materials Science, Thapar University, Patiala is an authentic record of my own work carried out under the supervision of Dr. O. P. Pandey. The matter embodied in this thesis has not been submitted in part or full to any other university or institute for the award of any degree.

Loveleen Kaur Brar

This is to certify that the above statement made by the candidate is true to the best of my knowledge.

Dr. O. P. Pandey

Senior Professor
School of Physics and Materials Science
Thapar University, Patiala.

Contents

Acknowledgement

This thesis has been kept on track and been seen through to completion with the support and encouragement of numerous people including my supervisor, colleagues, friends and various institutions. It is my pleasure to express my deep sense of thanks to several individuals who journeyed with me and helped me to reach my destination.

My first and foremost offering of thanks goes to my supervisor **Dr. O. P. Pandey** for his excellent guidance, constant encouragement, valuable suggestions, blessings, extreme care and providing me with an excellent atmosphere for doing research and preparation of the thesis. I especially thank him for keeping faith in me when I lost all of mine. I would like to take this opportunity to thank **Dr. Gourav Singla** for introducing me to the fields of autoclave synthesis and electro catalysis. His dedication and attitude towards research has always inspired me to work hard. The new insights and references which he bought to discussions were always very fruitful.

It is my privilege to thank **Prof. Prakash Gopalan,** Director, Thapar University, Patiala for providing me resources in the university and needful help during the various stages of my work.

I am also like to express my thanks to current and previous **Head, SPMS** for their continuous support and encouragement. I would like to express my whole-hearted thanks to the members of my **doctoral committee** for their constant encouragement, insightful comments and fruitful criticisms. My special thanks to all my colleagues at **SPMS** who always supported and encouraged me. I would also like to thank **Mr. Indermani Mishra**, **Mrs. Neelam Sadana, Mrs. Parveen Kumari, Mr. Purshottam Singh, Mr. S. P. Verma, Mr. V. Kothari, Mr. Jant Singh**, **Mr. Lal Ji**, **Mr. Sriom Pundir** and **Mr. Pardeep Singla** for their timely help at various times. I would like to extend my thanks to **Mr. Ghanshyam Morya** and **Mr. Mukesh Aggarwal** at SAI labs for their continuous help over the years.

I believe this is a very opportune time to thank all my lab mates (past and present) at the Functional Materials Lab, Ceramic Materials Lab and the erstwhile Thermal Lab. This journey would have been very boring and joyless w/o you all. The encouraging and helpful atmosphere made my time in the lab a very interesting

learning experience. The new techniques and fields to which I was introduced and was helped to master have all contributed to my growth as a researcher.

I find this is a good time to acknowledge all my friends who have not let obstacles like distance and time from keeping my life full of joy and positivity.

I really cannot find words which can express my love, regard and thanks to my family for standing by me in this long (sometimes too long) journey. I would especially like to thank my mother **Amarjeet Kaur** and my niece **Aviroop Kaur** for keeping me grounded and focused on important things in life: good food, ludo and laughter with family.

Above all I would like to acknowledge the Almighty for blessings and positive energy which sustained me during all stages of this work. I am especially grateful for the gift of all the special people that surround me.

Loveleen Kaur Brar

List of Publications from PhD work:

1. Loveleen K. Brar, Gourav Singla, Navjot Kaur and O. P. Pandey, Thermal stability and structural properties of Ta nanopowder synthesized via simultaneous reduction of Ta_2O_5 by hydrogen and carbon, *J. Therm. Anal. Calorim.* **119** (2015) 175.
2. Loveleen K. Brar, Gourav Singla and O. P. Pandey, Evolution of structural and thermal properties of carbon-coated TaC nanopowder synthesized by single step reduction of Ta-ethoxide, *RSC Adv.* **5** (2015) 1406.
3. Loveleen K. Brar, Gourav Singla and O. P. Pandey, The role of carbon in structural evolution during single step synthesis of nano tantalum carbide, *RSC Adv.* **6 (2016)** 109174
4. Loveleen K. Brar and O. P. Pandey, Synthesis of ultra-small tantalum carbide and significance of powder characteristics in electrochemical HER. (manuscript under preparation)

List of Figures

Chapter 5

Chapter 7

List of Tables

Chapter 6

Chapter 7

Preface

Interstitial transition metal carbides (ITMCs) display unique mechanical, thermal (high melting point) and electromagnetic properties. ITMCs of group IV and V metals show strong non-stoichiometric character i.e. the composition of the carbide can vary over a wide range without any change in the crystal structure. The change in composition of strongly nonstoichiometric compounds is a very important parameter in determining the properties of these materials. These materials are extremely hard, have the highest known melting points and are also radiation resistant. Out of the entire group V ITMCs Tantalum Carbide (TaC) finds its industrial applications because of its high temperature stability. Synthesis of nano sized powders of TaC with large specific surface area and their complete characterization is of paramount importance for ultra- high temperature (UHT) as well as catalytic applications. Apart from the precursors, the synthesis method and processing parameters like temperature, time, pressure, and catalyst *etc.* play very important role in determining the properties of the final powders and hence their performance. The stoichiometry of TaC plays an important role in determining its properties in UHT as well as electro catalytic applications.

The present work deals with the synthesis and characterization of nano sized cubic TaC by single step chemical reaction synthesis route. Further, the prepared materials have been tested as electrocatalyst for HER in acidic media. The entire work of the thesis is divided into eight chapters.

Chapter 1 deals with the interstitial transition metal carbides (ITMCs). Properties and industrial applications of ITMCs are discussed taking into consideration their crystal structure and bonding. Non stoichiometric nature of the group IV and V ITMCs and its influence on property determination is described. Among the ITMCs, the significance of TaC, its industrial applications, especially as ultra-high temperature material (UHTM), are discussed. The tantalum-carbon binary system with all possible structures (γ-TaC, α-Ta2C, β-Ta2C, ζ-

Ta4C3) is presented. The variation in nature of bonding within the TaC phase at sub-stoichiometric carbon concentrations is discussed. Bulk synthesis methods for TaC are briefly described. The need for development of well characterized nano TaC for mechanical, UHT and electrocatalytic applications is discussed.

Chapter 2 describes the literature available on the work being done in the field of synthesis and characterization of nano-sized TaC. Prevalent methods for the synthesis of single phase cubic-TaC and their salient features are presented. The understanding about the details of different parameters which affect the final powder characteristics such as precursor for tantalum, carbon source, their characteristics, their mixing ratios, temperature regime for synthesis, atmosphere during heating, presence/absence of catalysts, etc. have been described. The work done on electrochemical activity and properties of TaC for HER are also presented.

Chapter 3 includes the protocols followed in the present investigation for the synthesis of TaC nanopowders from different Ta precursors. Basics of different characterization techniques, sample preparation for the same and data analysis methods used for the characterization of the synthesized nano-powders are also discussed in this chapter. The techniques discussed are: X-ray diffraction (XRD), Thermal analysis (DSC/TGA/DTG), Field-Emission Scanning Electron Microscope (FE-SEM), Transmission electron microscopy (TEM), BET analysis and Electrochemical measurements.

Chapter 4 deals with the synthesis and characterization of nano TaC from tantalum-ethoxide precursor. The XRD results of the synthesized samples have been analysed and discussed. The carbon content of the lattice of TaC nanopowders, size and strain has been used to determine the evolution of the nanopowders with time as well as temperature. Based on XRD results the formation mechanism of the nano TaC has been proposed. From the thermal analysis results, the stability of the synthesized powders over range of temperature(s) as well as the external carbon content of the powders has been evaluated. FE-SEM and TEM results

have been presented and discussed to analyse the microstructure of the synthesized powders and to confirm the crystal structure of product phase by measuring the lattice spacing using HR-TEM. Surface area and pore size distribution of the synthesized samples has been analysed by BET technique.

Chapter 5 gives the details for the synthesis and characterization of nano TaC from Ta_2O_5 precursor using acetone as reducing and carburization agent. The effect of Mg and acetone in the initial mixture as well as the effects of time and temperature on the final product are studied. The powders obtained have been characterized using XRD, DSC-TG, FE-SEM, HRTEM and BET. Based on XRD results and thermodynamic parameters, the formation mechanism of the TaC has been proposed. The strain and size evolution of the powders with time has been used to explain the grain growth mechanism in the system. The role of carbon in structural evolution has been analysed and discussed.

Chapter 6 comprises of the results obtained for the synthesis and characterization of the nano cubic TaC from $TaCl_5$ precursor using acetone as reducing and carburization agent. The XRD and thermal analysis results of the synthesized samples have been analysed and discussed. The carbon content of the TaC nanopowders, size and strain has been used to determine the evolution of the nanopowders with time as well as temperature. Based on XRD results and thermodynamic parameters, the formation mechanism has been proposed. From the thermal analysis results, the stability of the synthesized powders over range of temperature(s) as well as the external carbon content of the powders has been evaluated. FE-SEM and TEM results have been presented and discussed to analyse the microstructure of the synthesized powders and to confirm the crystal structure of product phase. Surface area and pore size distribution of the synthesized samples has been analysed by BET technique.

Chapter 7 deals with the results related to the suitability of the obtained product as electrocatalyst in acidic media for HER. The effect of particle characteristics such as carbon content, strain etc. on the electrocatalytic activity has been analyzed and discussed in this chapter.

Chapter 8 summarizes the entire work done in the present study. The work done shows that tailored cubic phase TaC nano powders can be synthesized in single step from Ta-Ethoxide, Ta_2O_5 and $TaCl_5$. The results obtained from the electrochemical study of prepared powders have also been concluded in this chapter. The influence of various powder characteristics like strain, carbon content etc. on the HER electrocatalytic activity is summarized.

CHAPTER 1

Introduction

Overview

In this chapter the interstitial transition metal carbides (ITMCs) are introduced. Industrial applications and properties of ITMCs are discussed taking into consideration their crystal structure and bonding. Non stoichiometric nature of the group IV and V ITMCs and its significance in property determination is introduced. Among the ITMCs, the significance of tantalum carbide (TaC), its industrial applications, especially as ultra-high temperature material (UHTM), are discussed. The tantalum-carbon binary system with all possible structures (γ-TaC, α-Ta_2C, β-Ta_2C, ζ-Ta_4C_3) is presented. The variation in nature of bonding within the TaC phase at sub-stoichiometric carbon concentrations is discussed. Bulk synthesis methods for TaC are briefly introduced. The need for development of well characterized nano TaC for mechanical, UHT and electrocatalytic applications is also discussed.

Carbides are a versatile group of materials consisting of carbon and some atom having equal or less electronegativity. Based on the differences in electronegativity, size and bonding characteristics, the carbides are categorized as interstitial (transition metals of Grp IV, V, VI), covalent (B, Si), intermediate (transition metals of Grp VII, VIII) or salt-like (elements of Grp I, II, III) [1]. Interstitial transition metal carbides (ITMCs) display unique mechanical (hard, strong and some-what brittle), thermal (high melting point) and electromagnetic (metal like) properties. Due to their high melting points and chemical stability ITMCs form an important subgroup of refractory materials. ITMCs find technological applications in multiple and diverse fields such as space craft nozzles, high speed drill bits, snow tires, electrical contacts, optical coatings and as electro catalysts in fuel cells. These applications are due to the higher strength, durability and hardness of the ITMCs coupled with interesting, optical, electrical and magnetic properties [2].

1.1 Interstitial Transition metal carbides (ITMCs)

ITMCs are formed when the electronegativity and the size difference between the transition metal and carbon is large. In comparison with the carbon atom (atomic radius = 0.078 nm and electronegativity = 2.5), the transition metals of Grp. IV, V, VI having large sizes (0.1267-0.1597 nm) and small electronegativities (1.3-1.8) are good candidates for forming ITMCs [3]. As a consequence of the large difference in size, the carbon atom is accommodated in the interstices of the host metal lattice. Due to the difference in electronegativity, sp^3 hybridization of the carbon atom and its interstitial location within the host metal lattice, the bonding for ITMCs is partly covalent and ionic, but mostly metallic. As a result of the host metallic lattice they often have indeterminate composition (like metallic alloys), high density and high electrical and thermal conductivities. Ionic and covalent contributions to bonding in ITMCs lead to high melting points, hardness and chemical inertness [1]. Melting points of ITMCs are some of the highest among any type of materials. Hardness and Young's Modulus of ITMCs is comparable to that of ceramic materials. The conductivity though reduced than the pure metals is still in the range of good electrical conductors.

1.2 Crystal structure of ITMCs

Formation of the ITMCs involves the adjustment of carbon atom in the interstitial sites of the host metal lattice. For the stable carbide formation the metal lattice in ITMCs is altered to a

structure in which the carbon atom can be accommodated in the interstitial sites. The final crystal structure of the ITMCs is governed by the carbon to metal atom radius ratio (r_c/r_m). The possible lattice structures are hcp or fcc with octahedral voids ($r_c/r_m \leq 0.59$) or hexagonal lattice with trigonal prismatic voids ($0.53 < r_c/r_m < 0.59$). For $r_c/r_m > 0.59$ more complex structures are formed, e.g., Cr. The change in the structure of the host metal lattice also results in an increase in the metal-metal atomic spacing (Table 1.1) [1, 3]

.

Table 1.1: Table listing the properties of the parent metal and the transition metal carbides.

Transition metal	**Ti**	**Zr**	**Hf**	**V**	**Nb**	**Ta**	**Cr**	**Mo**	**W**
Electronegativity	1.5	1.4	1.3	1.6	1.6	1.5	1.6	1.8	1.7
E. Config.	[Ar] $3d^2 4s^2$	[Kr] $4d^2 5s^2$	[Xe]$4f^{14}$ $5d^2 6s^2$	[Ar] $3d^3 4s^2$	[Kr] $4d^4 5s^1$	[Xe]$4f^{14}$ $5d^3 6s^2$	[Ar] $3d^5 4s^1$	[Kr] $4d^5 5s^1$	[Xe]$4f^{14}$ $5d^4 6s^2$
Host metal lattice	hcp, bcc	hcp, bcc	hcp, bcc	bcc	bcc	bcc	bcc	bcc	bcc
r_c/r_m	0.526	0.483	0.486	0.576	0.530	0.529	0.609	0.556	0.553
Carbide Lattice	TiC fcc	ZrC fcc	HfC fcc	VC fcc	NbC fcc	**TaC** fcc	Cr_3C_2 orthor	Mo_2C hex	WC hex
Coordination No.	6	6	6	6	6	6	6	6	6
Change in host metal-metal bond length (%)	4.5	3.9	3.8	8.8	7.5	6.9	12.3	10.3	5.8
Hardness (GPa)	28-35	25.5	26.1	27.2	19.6	16.7	10-18	16-24	22
Melting Point (°C)	3067	3420	3928	2830	3600	3950	1810	2520	2870

1.3 Bonding and Properties of ITMCs

The ITMCs have physical and mechanical properties resembling to those of ceramics. In contrast, the electronic and magnetic properties of the ITMCs are similar to that of the metals. There are only metal-metal and metal-carbon bonds in ITMCs. The direct interaction between carbon atoms is absent due to the interstitial location of carbon atoms. Metal-metal interaction is mainly metallic and results in finite density of states at the Fermi level and other metal like properties of the ITMCs. Partially filled d orbital electrons for the transition metal also results in some covalent contribution to the metal-metal bond [3]. The metal-carbon bonds have an ionic contribution due to transfer of electrons from the metal to the carbon atom and covalent contribution due to bonding between metal d-state and p-state of the

carbon. Calculations show that the metal-carbon bonds in ITMCs are more covalent than ionic.

1.4 Electrocatalytic properties of ITMCs

Fuel cells with their inherent higher efficiency (as compared with Carnot cycle devices), low emission rates and usage of clean and renewable fuels are expected to play an important role in meeting the energy needs of the future. Fuel cells are classified based on their fuel type, electrolyte and operating temperature. For low temperature (< 373 K) fuel cells like PEMFC and DMFC the electrocatalysts stable under strongly acidic conditions (pH<2) are required [4]. Noble metals like Pt and Ru are the most commonly used electro catalysts in the fuel cells. Limited supply and high cost of Pt limits the large scale commercial usage of fuel cells. To achieve the similar performance of fuel cells with either reduced Pt content or replacing it completely with a low cost material depicting similar performance is an important area of research. ITMCs are chemically stable and show high corrosion resistance. They have shown similar electro catalytic properties as the noble metals like Pt in a wide variety of reactions [4]. Physicochemical properties of ITMCs are related to their electronic structure. The expansion of metal lattice during the formation of carbides (Table 1.1) causes the metal d-band to contract. This d-band contraction increases the density of states at the Fermi level as compared to the parent metal. This contributes to ITMCs having noble materials like catalytic properties [4].

1.5 Nonstoichiometric character of ITMCs

ITMCs of group IV and V metals show strong non nonstoichiometric character i.e. the composition of the carbide can vary over a wide range without changing the crystal structure. The existence of nonstoichiometric compositions in group IV and V carbides is due to the cubic symmetry of the host metal lattice [5]. A high concentration of structural vacancies is one of the most significant properties of strongly nonstoichiometric carbides. The change in composition of strongly nonstoichiometric compounds is a very important parameter in determining the properties of these materials. These materials are extremely hard, have the highest known melting points and are also radiation resistant. Out of the entire group V ITMCs Tantalum Carbide finds the most industrial applications [1].

1.6 Tantalum carbide (TaC) – applications and properties

Ultra high-temperature (UHT) applications such as handling of molten metals, electrodes for electric arc furnaces, and aerospace applications require materials capable of operating at temperatures exceeding 2000 °C. Apart from these, the other beneficial mechanical and thermochemical properties are namely, high strength, high fracture toughness, and increased oxidation resistance. Large negative free energy of formation, ΔG (~ -143 kJ) results in TaC to have good chemical and thermal stability even in extreme conditions [6]. The B1 phase of TaC has a melting temperature near 3950 °C [7] and exhibits plasticity at temperatures greater than 1500 °C [8]. These attributes make TaC a prime candidate material for UHT structural applications and thermo-mechanical applications like automotive wear resistant liners etc. Resistance to chemical attacks and oxidation also make it a good catalyst or a catalyst support material [9-11]. High electrical and thermal conductivity make it a candidate for electrical contacts [12-14]. Figure 1.1 shows the important industrial applications for TaC and Table 1.2 lists its main properties [1,2].

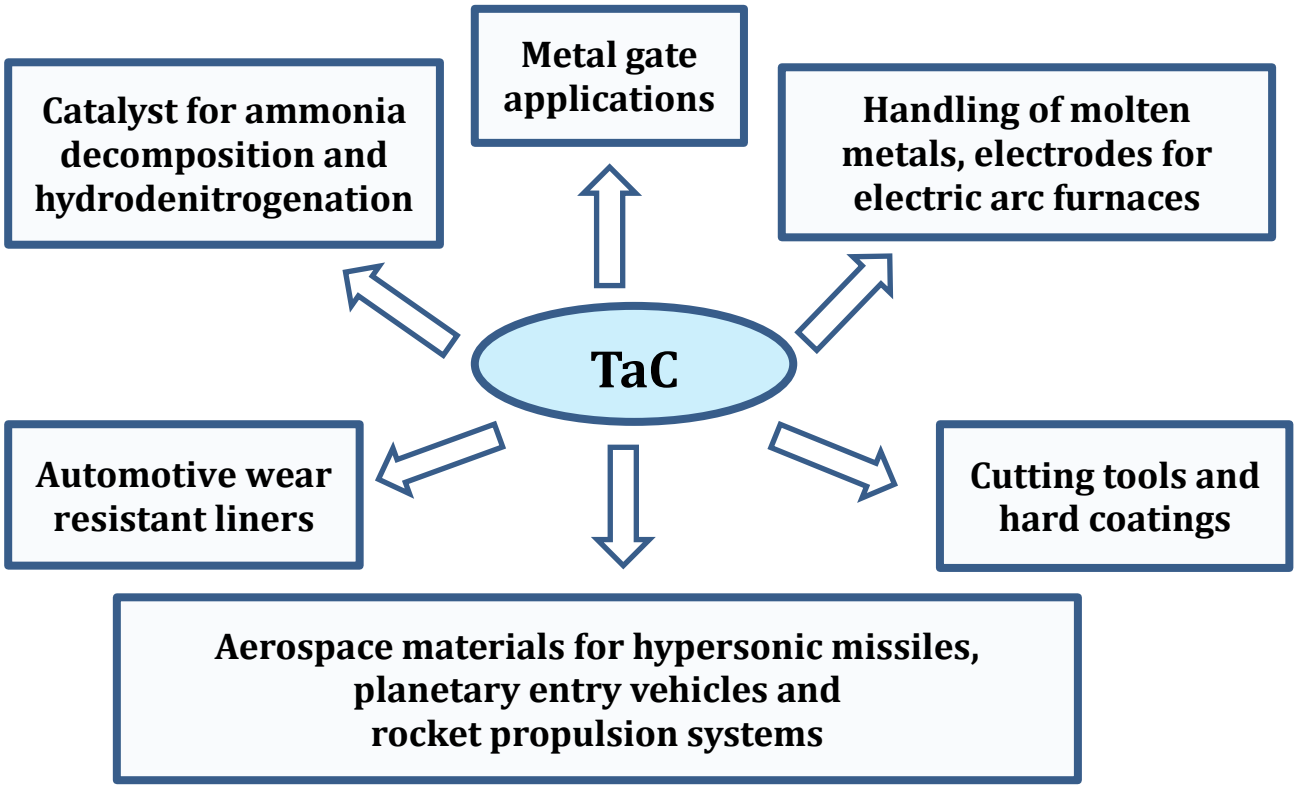

Figure 1.1: Important industrial applications of TaC.

Table 1.2: Physical and mechanical properties of TaC .

S. No.	Property	Value
1.	Structure, Space Group	NaCl (B1), $Fm\bar{3}m$
2.	Lattice constant	0.44555 nm
3.	Composition	$TaC_{0.73} - TaC_{1.0}$
4.	Molecular Weight	192.96 g/mol
5.	Density	14.8 g/cm^3
6.	Melting point	3950 °C (melts without decomposition)
7.	Heat of Formation ($-\Delta H_f$)	142.7 kJ/g-atom metal (at 298 K)
8.	Electrical Resistivity	25 μΩ-cm
9.	Thermal Conductivity	22.1 W/m-°C
10.	Bond Energy	16.95 eV
11.	Thermal Expansion Coefficient	6.3 x 10^{-6} / $^{\circ}$C
12.	Superconductive Transition	10.3 K
13.	Hall Constant	-1.1 x 10^{-4} cm^3/A-s
14.	Magnetic Susceptibility	+ 9.3 10^{-6} emu/mol
15.	Vickers Hardness	16.7 GPa
16.	Modulus of Elasticity	285-560 GPa

Bulk samples of TaC oxidize rapidly in air at 800 °C but decarburize at very high temperatures (3000 °C) when heated in hydrogen. TaC does not react with nitrogen up to 2700 °C. TaC is one of the most chemically stable carbides. It is stable in nonoxidizing acids, but is attacked easily by HNO_3 and HF, and by melts of oxidizing salts [1].

1.7 Tantalum - Carbon binary system

TaC belongs to the group of strongly nonstoichiometric ITMCs. Figure 1.2 gives the phase diagram for the binary Tantalum-Carbon system [1,15]. Main phases are TaC and Ta_2C. The TaC phase has rock-salt structure (B1 compound) with homogeneity interval of $TaC_{0.75}$ to TaC (Figure 1.3 (a)). Hexagonal Ta_2C has two possible structures: α-Ta_2C (CdI, antitype, carbon ordered sublattice) or β- Ta_2C (L"3, carbon disordered sub-lattice) (Figure 1.3 (b)). It has been speculated that δ-Ta_4C_3 phase, which is a metastable phase with rhombohedral lattice, is formed on cooling when the temperature is too low to transform TaC directly into Ta_2C (Figure 1.3 (c)).

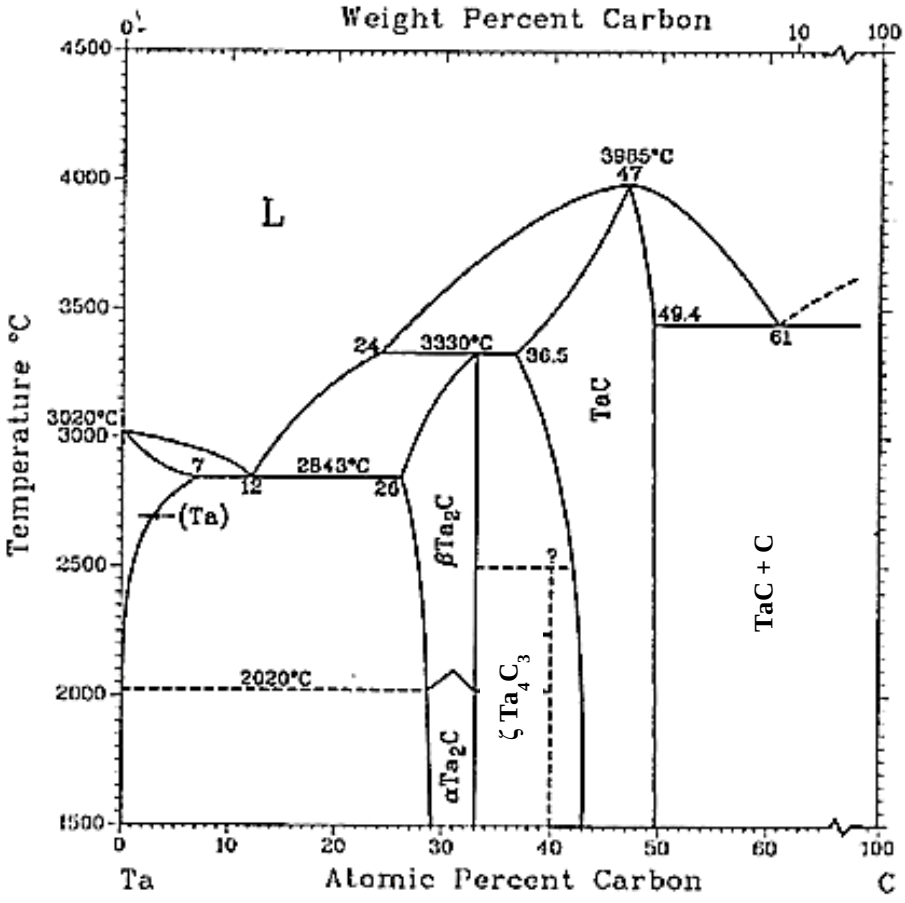

Figure 1.2: Phase diagram of Ta-C system [1, 15].

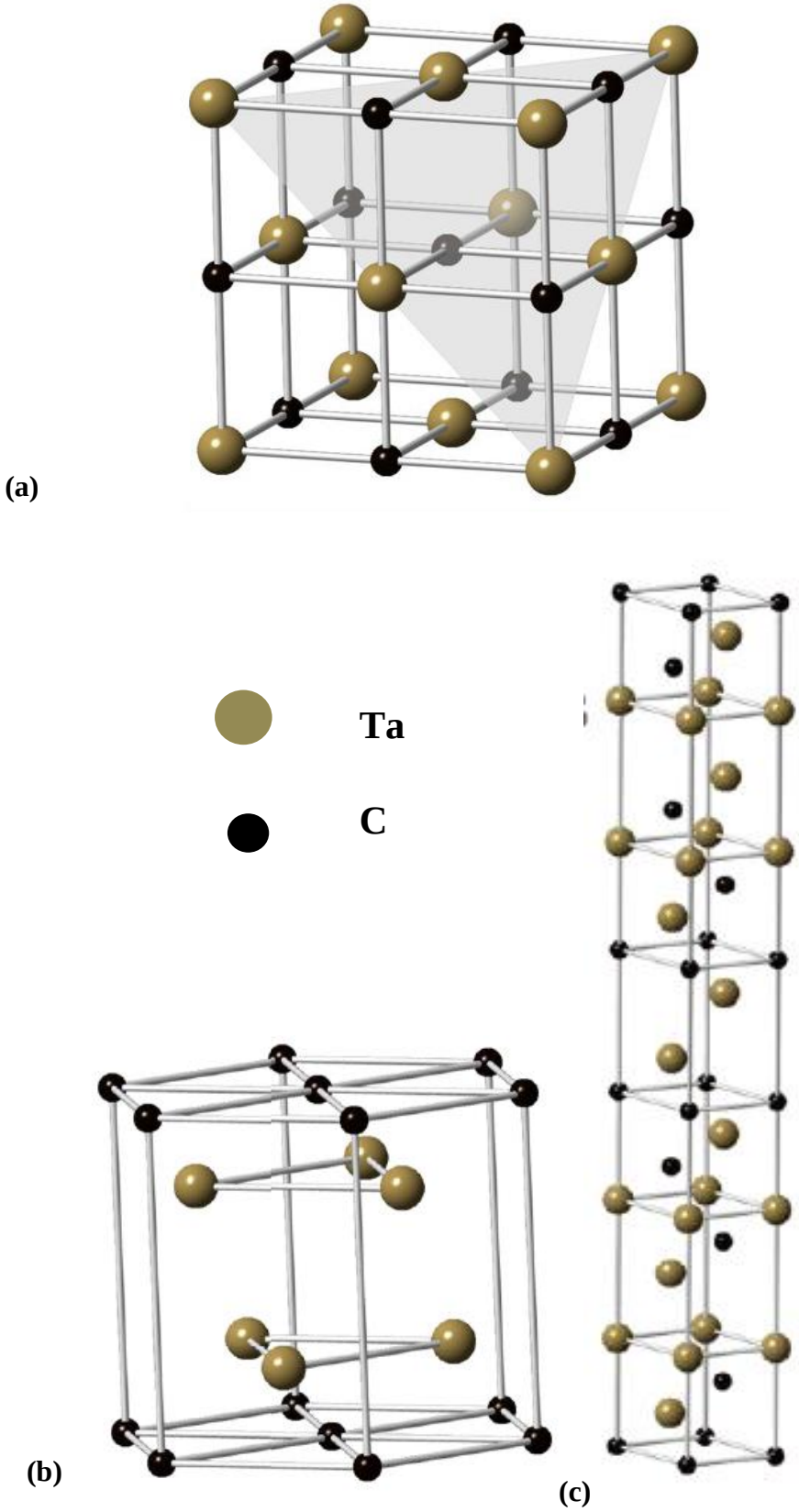

Figure 1.3 (a) Crystal structure of TaC [15,16], Carbon deficient phases of TaC: (b) β-Ta_2C, (c) ζ – Ta_4C_3 [15].

1.8 Bonding in TaC

Bonding in ceramics exhibiting rock-salt structure is primarily ionic. Existence of non-stoichiometric compositions for TaC is a clear signature that ionic contribution to bonding is not dominant. Phase diagram for Ta-C system (Figure 1.2) clearly shows that for $TaC_{0.89}$ there is a sharp solidus maximum near ~3985 °C. TaC is one of the highest melting substance known at ambient pressure. High melting point of TaC qualitatively indicates dominant covalent bonding in the system. The tantalum 5d electrons and the carbon 2p electrons overlap to form strong sigma bonds. Density function theoretical studies indicate that for sub stoichiometric TaC the density of states (DOS) at Fermi level decreases. The decrease in DOS indicates that the covalent nature is becoming more dominant at the cost of metallic bonds. This is confirmed with an increase in melting point for sub stoichiometric compositions. The DOS has a minimum at C ~ 0.89. It is believed that at this C concentration loss of carbon in B1 structure leads to optimal bonding between the Ta having 5 valence electrons and carbon which prefers 4 electrons [17]. The metal-metal bond for TaC is formed through the overlap of valence d-electrons of neighbouring tantalum atoms. As the C loss in TaC happens the lattice parameter of the TaC shrinks linearly [18]. The decrease in melting point for C<0.89 indicates that the overlap and hence the metallic character increases on decrease in C beyond 0.89. Variation in the nature of the bonding in TaC with stoichiometry makes the characterization of carbon content within the TaC phase extremely important for understanding the behaviour of the material.

1.9 Nano crystalline Tantalum carbide

The important properties of UHTCs (e.g.Young's Modulus, fracture toughness, flexural strength, and oxidation resistance etc.) after processing are related to density and microstructure of the final product [19]. Lack of proper densification is a very crucial issue for TaC processing. Factors such as low self-diffusion coefficient, highly covalent bonds, oxide impurities on the surface and rapid grain growth at high temperatures etc., all contribute to requirements of extremely high temperatures (>2000 °C) for obtaining fully dense pure TaC [20]. During the liquid phase sintering of TaC in presence of transition metals full density is never reached [21]. The formation of solid solutions between TaC and other carbides (ZrC and HfC) has been shown to improve densification by hot pressing [5, 22]. The reactive additives such as TaB_2, C and B_4C remove the oxygen impurities and promote densification [19,20,23,24]. Active carbon additives either in the form of carbon

black or graphite, or even CNTs and graphene, promote the sintering of pure nano-TaC without hot isostatic pressing (HIP) [25-31]. Using elemental silicon as the sintering aid > 96.7% theoretical density along with good flexural strength can be achieved [32]. The density of the final product is also improved by using fine grained powders [33,34]. Nano-powders as starting materials give better properties to the final phase. Powder metallurgical methods traditionally used for TaC synthesis involve 2 stages: direct carburizing followed by diffusion process involving diffusion of carbon through TaC compound layer requiring higher temperatures and proper carbon concentration gradient [35-37]. On an industrial scale, TaC is primarily obtained by heating Ta_2O_5 at high temperatures under vacuum, followed by carburization for long time in the presence of carbon source at high temperatures [38]. These methods are energy intensive and also the high synthesis temperatures required result in coarsening of grains. Synthesis of pure phase nano-TaC with large specific surface area is of paramount importance for catalytic as well as for the traditional applications. TaC is strongly nonstoichiometric so the carbon content in the initial as well as the final phase determines the mechanical properties of the material and also the surface stoichiometric properties which ultimately affect the catalytic response of the material [11,39]. So the TaC nano-powders need to be characterized for size, specific surface area as well as stoichiometry [40]. In the next chapter the advancements in the synthesis of nano-TaC are discussed. Further, some of the latest advancements in the sintering methods for TaC as well as the property variations with carbon content and applications are also presented.

References:

[1]. H.O. Pierson, *Handbook of refractory carbides and nitrides*, Noyes Publications, New Jersey, USA (1996).

[2]. S.T. Oyama, *The chemistry of transition metal carbides and nitrides*, Blackie Academic & Professional, Glasgow, NZ (1996).

[3]. V. Raghavan, *Materials Science and Engineering*, PHI learning Pvt. Ltd, Delhi, India (2015).

[4]. D.J. Ham, J.S. Lee, *Energies* **2** (2009) 873-899.

[5]. A.I. Gusev, A.A. Rempel, A.J. Magerl, *Disorder and Order in Strongly Nonstoichiometric Compounds - Transition metal carbides, nitrides and oxides*, Springer-Verlag Berlin Heidelberg, New York, USA (2001).

[6]. B.C. Schulz, *Processing and Characterization of Tantalum-Hafnium Carbides*, M.Sc. Thesis, The University of Alabama, (2011) 1-14.

[7]. R.A. Andrievskii, N.S. Strel'nikova, N.I. Poltoratskii, E.D. Kharkhardin, V.S. Smirnov, *Powder Metall. Mater. Ceram.* **6** (1967) 65-67.

[8]. C. Kim, G. Gottstien, D.S. Grummon, *Acta Metall. Mater.* **7** (1994) 2291-2301.

[9]. N.S. Alhajri, H.Yoshida, D.H. Anjum, A.T. Garcia-Esparza, J. Kubota, K. Domen, K. Takanabe, *J. Mater. Chem. A* **1** (2013) 12606-12616.

[10]. E.J. Rees, K. Essaki, C.D.A. Brady, G.T. Burstein, *J. Power Sources* **188** (2009) 75-81.

[11]. J.-G. Choi, *J. Porous Mater.* **20** (2013) 1059–1068.

[12]. Y.-J. Chen, J.-B. Li, Q.-M. Wei, H.-Z. Zhai, *Mater. Lett.* **56** (2002) 279-283.

[13]. Y. Asaoka, T. Kaneko, N. Sano, US Patent EP1666413 A1, (2006).

[14]. K. Tuokedaerhan, R. Tan, K. Kakushima, P. Ahmet, Y. Kataoka, A. Nishiyama, N. Sugii, H. Wakabayashi, K. Tsutsui, K. Natori, T. Hattori, H. Iwai, *Appl. Phys Lett.* **103** (2013) 111908 1-3.

[15]. R.A. Morris, *Microstructural formations and phase transformation pathways in Tantalum carbides*, Doctoral Thesis, The University of Alabama, (2010).

[16]. E.K. Storms, *The refractory carbides*, Academic Press Inc., New York, USA, (1967).

[17]. W.G. Fahrenholtz, E.J. Wuchina, W.E. Lee, Y. Zhou, *Ultra-High temperature ceramics - materials for extreme environment applications*, John Wiley & Sons, Inc., Hoboken, New Jersey (2012).

[18]. A.L. Bowman, *J. Phys. Chem.* **65** (1961) 1596-1598.

[19]. X. Zhang, G.E. Hilmas, W.G. Fahrenholtz, *Mater. Sci. Eng., A* **501** (2009) 37–43.

[20]. X. Zhang, G.E. Hilmas, W.G. Fahrenholtz, *J. Am. Ceram. Soc*. **90** (2007) 393–401.

[21]. S. Scholz, *Special Ceramics 1962, Proc. Symp. by the Br. Ceram. Res. Assoc.*, Academic Press Inc., New York, (1963) 293–307.

[22]. L. Silvestroni, A. Bellosi, C. Melandri, D. Sciti, J.X. Liu, G.J. Zhang, *J. Eur. Ceram. Soc.* **31** (2011) 619–627.

[23]. X. Zhang, G.E. Hilmas, W.G. Fahrenholtz, *J. Am. Ceram. Soc*. **91** (2008) 4129–4132.

[24]. K. Balani, S.R. Bakshi, T. Mungole, A. Agarwal, *J. App. Phys.* **111** (2012) 0635211-3.

[25]. I.G. Talmy, J.A. Zaykoski, M.M. Opeka, *J. Eur. Ceram. Soc.* **30** (2010) 2253–2263.

[26]. B.-R. Kim, K.-D. Woo, J.-M. Doh, J.-K. Yoon, I.-J. Shon, *Ceram. Int.* **35** (2009) 3395–3400.

[27]. S.R. Bakshi, V. Musaramthota, D.A. Virzi, A.K. Keshria, D. Lahiri, V. Singh, S. Seal, A. Agarwal, *Mater. Sci. Eng., A* **528** (2011) 2538–2547.

[28]. A. Nieto, D. Lahiri, A. Agarwal, *Mater. Sci. Eng. A* **582** (2013) 338–346.

[29]. A. Gubernat, *J. Eur. Ceram. Soc.* **33** (2013) 2391–2398.

[30]. D. Lahiri, E. Khaleghi, S.R. Bakshi, W. Li, E.A. Olevsky, A. Agarwal, *Scripta Mater.* **68** (2013) 285–288.

[31]. A. Nieto, D. Lahiri, A. Agarwal, *Scripta Mater.* **69** (2013) 678–681.

[32]. L. Zhong, L. Liu, C. Worsch, J. Gonzalez, A. Springer, F. Ye, *Mater. Chem. Phys.* **149-150** (2015) 505-511.

[33]. W.C. Ruoff, A.L. Yohe, *Am. Ceram. Soc. Bull*. **12** (1978) 647-651.

[34]. M.H. Becher, P.F. Leipold, *Ceram. Bull*. **49** (1970) 647-651.

[35]. J.A. Nelson, M.J. Wagner, *Chem. Mater.* **14** (2002) 1639-1642.

[36]. B.H. Eckstein, R. Forman, *J. Appl. Phys.* **33** (1962) 82-86.

[37]. A. Rubinshtein, R. Shneck, A. Raveh, J.E. Klemberg-Sapieha, L. Martinu, *J. Vac. Sci. Technol. A*, **18** (2000) 2017-2022.

[38]. E. K. Stroms, *The Refractory Carbides*, Academic Press, New York, (1967).

[39]. M. Ali, M. Urgen, M.A. Atta, A. Kawashima, M. Nishijima, *Mater. Chem. Phys.* **138** (2013) 944–950.

[40]. J.P. Kelly and O.A. Graeve, *J. Am. Ceram. Soc.* **94** (2011) 1706–1715.

CHAPTER 2

Literature Review

Overview

In this chapter, the work being done in the field of synthesis and characterization of nano-sized TaC is discussed. Prevalent methods for the synthesis of single phase cubic-TaC and their salient features are presented. The details of different parameters which affect the final powder characteristics such as precursors for tantalum as well as carbon, their characteristics, their mixing ratios, temperature regime for synthesis, atmosphere for heating, presence/absence of catalysts, etc. have been identified and described. The electrochemical activity and properties of TaC for hydrogen evolution reaction (HER) are also presented.

Synthesis of nano sized powders of TaC with large specific surface area and their complete characterization is of paramount importance for UHT as well as catalytic applications. The synthesis method and parameters such as starting material, carbon source, temperature, time, pressure, and catalyst *etc.* play very important role in determining the properties of the final powders and hence the performance of the final product. Many groups are active in the synthesis of TaC nanopowders for various applications. The most common starting materials in use are Tantalum oxide (Ta_2O_5) and tantalum chloride ($TaCl_5$), though the use of derived organic precursors cannot be ignored. The role of metal and metal halide catalysts on the final product and synthesis parameters has also been investigated. The synthesis methods investigated are wide ranging from direct carburization using methane to spray drying assisted mechano-chemical synthesis to solvothermal synthesis. The following section gives the overview of the work done in the synthesis of TaC nanopowders over last 15 years.

2.1 Synthesis techniques for nano TaC

2.1.1 Temperature programmed reduction

Temperature programmed reduction of the transition metal oxides for the formation of the respective carbides is one of the earliest used methods for carbide formation. **Claridge *et al.*** [1] and **Choi *et al.*** [2] studied the formation of TaC from the temperature-programmed reaction of Ta_2O_5 with methane and ethane. Claridge *et al.* [1] found that with methane TaC powder was formed at 950 °C whereas there is no reaction with ethane even at 1000 °C. Choi *et al.* [2] studied the effect of heating rate and the molar hourly space velocity of CH_4 on the final product formed at 1027 °C. Analysis showed that as the heating rate was decreased or molar velocity of CH_4 increased the surface area of tantalum carbides increased.

2.1.2 Solid state synthesis

Solid state synthesis involves reaction between solid species. Various groups have synthesized TaC using this route. For most of the cases the Ta_2O_5 is the Ta precursor whereas the carbon source used vary from activated carbon [3-6], MWCNTs [7], C_3N_4[8-10], cynamide [11] and melamine [12]. The precursor and the carburization agent with/without catalyst are mixed together thoroughly and heated either in vacuum or Ar atmosphere to the desired temperature. **Chen *et al.*** [3] studied the reaction involving Ta_2O_5 with activated carbon, Ni catalyst and halogen precursors NaCl or KCl or NaF. In the final product the TaC_x ($x<1$) whiskers were observed whose morphology could be altered with the halogen

precursor. **Fukunaga *et al.*** [7] heated a mixture of MWCNTs, Ta and iodine in Ar filled quartz ampoules at 1100 °C for 168 - 215 h. The final product was single phase cubic-TaC with a mixture of faceted crystals (of mean size 250 nm) and spheres (with average size 100 nm). **Li *et al.*** [8,11] and **Du *et al.*** [9] pellatized Ta_2O_5 with graphite like C_3N_4 (g- C_3N_4), cynamide precursor (CH_2N_2) and amorphous C_3N_4 (a- C_3N_4) carbon precursors respectively. The pellets were placed in an evacuated silica ampule and heated at 1150 ^{0}C for an hour. Average particle size of 35 nm, 9 nm and 10 nm was achieved respectively. An important fact to emerge from this work was that C_3N_4 acted as a carbothermal reduction reagent as well as carbonizing reagent.

Alhajri *et al.* [10] heated Ta precursor ($TaCl_5$ dissolved in Ethanol) soaked Mesoporous-graphitic (mpg) C_3N_4 in a semi-closed crucible at 750 °C to 1300 °C for 4 hours under different atmospheres (N_2, Ar or NH_3). The high C_3N_4/Ta precursor ratio resulted in high carbide.The crystallite size was 3 - 19 nm which increased with increasing synthesis temperature. One of the main benefits of this method was the ability to tune the particle size, depending on the pore size of mpg-C_3N_4 reactive template. **Lei *et al.*** [12] sealed the pellets of melamine ($C_3H_3(NH_2)_3$) and Ta_2O_5 (4:1 molar ratio) in an evacuated silica ampule and heated at 1100 °C for half an hour. The final product was single phase cubic TaC powder consisting of crystallites having average size of 13 nm embedded in amorphous carbon.

In recent years the microwave processing of carbides has been gaining attention due to shorter processing times (consequently saving time and energy) as well as an enhancement in chemical reaction [4]. **Rees *et al.*** [5] established that the synthesis of TaC from Ta_2O_5 and carbon by microwave heating was possible. The reaction reached 75% completion after 16 min of microwave heating. The final powders had a grain size of 60 - 400 nm. The authors also established that the use of metal (Ni) and metal chloride (KCl) catalysts was also feasible during the microwave synthesis.

Solar furnace concentrates the solar radiations, using optics, into a small cavity to obtain very high temperatures. It couples relatively simple design with high thermal flux and allows for heating without contamination and in controlled atmosphere. **Amaral *et al.*** [6] studied the formation of TaC in a solar furnace using pellets prepared from a mixture of metallic tantalum with either graphite (G) or amorphous carbon (aC) as a carburising medium. Heating upto 30 minutes resulted in the formation of pure phase TaC through carburisation in either Ar or N_2 atmosphere when G is used.

2.1.3 Self-propagating high temperature synthesis

Self-propagating high temperature synthesis (SHS) involves synthesis via exothermic reactions involving metals or their salts which result in a wave of energy propagating through the material which sustains and propagates the reaction. The products formed in this process are generally large in size due to uncontrolled combustion reaction. The recent work with addition of catalysts and additives has helped to extend the use of this method for nano powder synthesis. **Kim and Wooldridge** [13,14] studied the synthesis of TaC using equimolar pellets of metallic Ta and C with Iodine or CO_2 (in gas phase) as transport agents which enhanced the burning velocities. The final product particle morphology was similar to starting tantalum particles but had significantly larger specific surface area. Carbon stoichiometry of the final samples was > 0.9 and strongly dependent on mole ratio of the transport agent for CO_2. **Yeh and Liu** [15] studied the effect of initial temperature of the pellet, variation of Ta:C ratio and compaction of the pellet for catalytically assisted SHS. Increasing the green density of the starting pellet and preheating of the sample increased the flame-front velocity as well as enhanced the formation of stoichiometric TaC. The activation energies associated with SHS for TaC and Ta_2C were determined. Complete conversion to TaC was achieved for the pellet with compaction of 45% theoretical maximum density. **Won *et al.*** [16] synthesized nano-TaC by igniting a pellet of milled mixture of Ta_2O_5, Mg, carbon black and NaF in Ar atmosphere. The single phase cubic TaC is formed only for samples with both Mg and NaF. The final powders had particle size of 700 nm -3 μm with low free carbon concentration. **Lee *et al.*** [17] used the silicothermic reduction of potassium fluoro tantalate (K_2TaF_7) in the presence of carbon and poly tetra fluoroethylene (Teflon, $(C_2F_4)_n$). Addition of Teflon improved the ignitabiliy and also made the reaction self-sustaining. The final samples were single phase cubic TaC with mean particle size < 20 nm.

2.1.4 Solid state metathesis

Solid state metathesis (SSM) reactions are fast, self-energetic reactions involving the exchange of reacting partners, driven by the difference in lattice energy of coproduced salts. The reactions are extremely exothermic and flame/energy produced can vaporize most of the salts so only thermally robust materials can be isolated from these reactions. **Nartowski *et al.*** [18] used solid state metathesis route for the formation of TaC. Mixture of Ta_2O_5 or $LiTaO_3$ and calcium carbide was sealed in an evacuated quartz tube and heated. The reaction started at around 480 °C to 650 °C and finishes in 20-30 s but the crystalline carbide product was

obtained only after annealing for at least 6 hrs at 1000 °C. Tantalum carbide had agglomerates of average size 400 nm with the crystals varying in size from 20–120 nm.

2.1.5 Spray drying and mechano-chemical synthesis

Spray drying technique involves atomization of the fluid (solution or colloidal dispersion of particles) followed by solvent evaporation. The resulting powders are monodispersed and free flowing [19]. **Kwon *et al.*** [20] synthesized nanostructured Ta_2O_5 from spray dried tantalum oxalate precursor solution. This nanostructured oxide powder was milled with carbon to get a carbon-oxide composite. The formed composite when heated under hydrogen atmosphere underwent carbothermal reaction at 1050 °C to form TaC. The average crystallite size was 44-46 nm but the particle size distribution in the final powder was not uniform.

2.1.6 RF induction plasma

Thermal plasma processing is an often used method for the production of nanopowders. High temperature and high energy density of the plasma ensures that the precursors rapidly vaporize followed by homogeneous nucleation and grain growth. **Ishigaki *et al.*** [21] introduced atomized tantalum ethoxide in r. f. thermal plasma to get nano sized TaC. Addition of H_2 improved the powder quality. Increasing the plasma generating pressure resulted in larger particle size as well as size distribution.

2.1.7 Reduction of derived precursors

One of the established methods in materials synthesis for lowering the reaction temperature is to use organic precursors derived from oxide and/or other inorganic salts. **Preiss *et al.*** [22] used metal alkoxides or peroxo acid xerogels as precursors for the formation of TaC while using saccharose or the carbonaceous sol prepared from the coal tar pitch as carbon source. TaC formation started at 1000 °C but complete single phase was obtained only at 1500 °C. **Souza *et al.*** [23] synthesized ammonium tantalum oxalate complex ($(NH_4)_3[TaO(C_2O_4)_3].1.5H_2O$) from Ta_2O_5 and studied its pyrolysis in hydrogen and methane atmosphere at 1000 °C. The SEM micrographs show sponge like agglomerates of size <10 μm.

Xiang *et al.* [24] combined tantalum chloride with furan resin to form a liquid polymer precursor with variable C/Ta ratios. The dried precursor was crystallized into nano-structured T_2O_5 at 900 °C. At temperatures higher than 1600 °C the oxide was completely transformed

into cubic TaC uniformly embedded in carbon matrix with diverse grain distribution. The particle size varied from 10-100 nm.

Yosida and Oguro [25] prepared the TaC nanoparticles using dc arc discharge (30 V, 120 A, He, 100–300 Torr) with a homogeneous mixture of carbon powder (particle size of 400 mesh) and tantalum standard solution (1 mg/cc, atomic absorption spectrometry grade). The final samples consist of TaC_x nano-crystals (42-93 nm) encapsulated in multiwall carbon nanotubes.

Sevast'yanov *et al*. [26] formed transparent tantalum–carbon containing gel by hydrolization of tantalum alkoxide ($Ta(OC_5H_{11})_5$) with ethanol solution in the presence of LBS-1 bakelite lacquer. The Ta_2O_5 + 7C mixture, obtained by vacuum pyrolization of the gel at 450 °C, was heated and the single phase TaC is obtained only at 1050 °C. Particles were almost spherical with uniform size of 20 nm. **Ma *et al*.** [27] used a liquid precursor formed by ultrasonicating activated carbon nanopowders and tantalum ethylate to form films on crucible. Complete conversion to TaC occured at 1300 °C for 0.5 h heating in a graphitization furnace. The particles have an average size of < 50 nm. **Lima *et al.*** [28] synthesized solid precursor Tris (oxalate) hydrate ammonium oxitantalato from Ta_2O_5. The precursor is heated in alumina fixed bed reactor resistive furnace in H_2 (95%) and CH_4 (5%) atmosphere at 1000 °C for 120 minutes. The final product is single phase cubic-TaC powder consisting of agglomerates of nanoparticles (average size of ~ 12.9 nm). **Lu *et al.*** [29] synthesized polytantaloxanesal which is blended with allyl-functional novolac (AN) resin in various ratios and cured. The formation of single phase cubic TaC took place at 1400 °C. Final samples consisted of nearly spherical particles of diameter < 30 nm embedded in 5-10 nm thick turbostratic carbon layer.

2.1.8 Solvothermal

Kelly *et al.* [30-31] used pressure-less solvothermal synthesis involving thermal and chemical ignition techniques. $TaCl_5$ mixed with lampblack and one of the 3 reductants: lithium, magnesium and calcium are placed in a test tube with loosened stopper and lowered into the furnace maintained at the self-ignition temperature of the reductant. Once the reductant ignited, the sample was allowed to air quench. Ca was the most effective and Mg the least effective reducing element. High reductant stoichiometry favours smaller crystallite sizes. Carbon stoichiometry affects the conversion to final phase.

2.1.9 Autoclave

Ma *et al.* [32] synthesized pure phase TaC particles at 600 °C in autoclave. Precursors were tantalum pentachloride and sodium carbonate with metallic magnesium as reductant. The reduction of $TaCl_5$ by Mg is highly exothermic so it produced nascent Ta as well as high local temperatures which in turn decomposed sodium carbonate to produce nascent C. The high local temperature also helped improve the diffusivity of C in Ta and resulted in pure cubic phase TaC. The particle size of 40 nm was achieved and the powders have good thermal stability and oxidation resistance below 450 °C in air.

In the present work the focus is on synthesis of TaC and its applications as an electro catalyst for hydrogen evolution reaction (HER). Below are the details of literature pertaining to HER activity of TaC.

2.2 HER electro chemical studies

Carbon-free energy systems are expected to play a dominant role in fulfilling the needs in near future for production as well as storage of energy. Electrochemical and photoelectrochemical energy conversions are at the forefront among the technologies under study. These reactions find use in energy storage, energy production as well as fuel production. The bottleneck for reducing the cost and hence enhancing the spread of devices based on these reactions is due to lack of a low cost material which can either replace Pt or reduce its loading in the Hydrogen evolution reaction (HER) at the cathode [33]. A good material should have low activation energy, large specific surface area, support large current densities and high stability in the highly acidic and basic conditions which usually exist. Transition metal carbides of IV-VI have emerged as suitable candidate as electro catalyst for HER due to their unique properties [34]. Though most of the work has been done for carbides of tungsten and molybdenum, other transition metal carbides including TaC have also been studied for their suitability as electro catalyst for HER.

Li *et al*. [35] studied the catalytic dissociation of H_2 on a tantalum carbide filament during the hot-filament chemical vapour deposition (HFCVD) of diamond thin films at 2000 - 3000 °C filament temperature. Results show that catalytic dissociation of H increases with temperature. **Rees *et al***. [5] studied the electrocatalytic activity of TaC samples synthesised using microwave heating. The observed Tafel slope was 95 mV/dec for HER.

Choi [2] studied the production of H_2 from ammonia using TaC and explored the relationship between surface stoichiometry (***x***, TaC_x) and size of TaC with its catalytic activity. The NH_3 decomposition activity decreased with size of TaC. The highest activity measured was for ***x*** = 0.85. But for particle size for ***x*** = 0.85 sample was also the smallest among all measured samples. While discussing the final results the size and stoichiometric effects have not been separated. The state of the tantalum valence electrons have been measured using XPS and it was found that for sub stoichiometric TaC, there are electrons available in the d shell of Ta which may contribute to enhanced electro catalytic activity.

Alhajri *et al*. [10] studied the hydrogen evolution under acidic conditions (pH 1) for TaC particles embedded in the matrix of the carbonaceous species. The higher current density observed for the samples has been attributed to the high surface area as well as the carbonaceous residue in contact with the nanoparticles which provide an electronic bridge to improve electronic conductivity. The rate determining step is the Volmer discharge reaction.

He *et al*. [36] evaluated the activity of hybrid TaC nanosheets on reduced graphene oxide as an efficient and stable electrocatalyst for water splitting step. The samples show high current density with Tafel slope of 58 mV/dec which indicated that the rate determining step was the electrochemical desorption of H_{ads} and H_3O^+ to form H_2. XPS studies revealed that there is a negative charge-transfer from tantalum to carbon within the RGO-supported TaC which could lead to higher HER activity.

2.3 Goal of this work

The literature survey of the synthesis of nano sized TaC reveals that Ta_2O_5 is the most common precursor used for reduction reactions. Decrease in size of Ta_2O_5 leads to reduction in reaction temperature due to increase in reactivity. The nanosized-Ta_2O_5 can be used either as a starting material or it can be produced in one of the intermediate steps. The latter is preferred because it is generally accompanied by the Ta_2O_5 particles being well dispersed in a C matrix and hence improving the reaction kinetics. $TaCl_5$ is the other most commonly used precursor especially as a starting material to form various derived precursors due to its high reactivity. Apart from these another promising precursor is Ta-Ethoxide. The decomposition of Ta-Ethoxide happens at ~ 450 °C so it is easier to reduce and can also be used as a precursor for the formation of nano-particles of Ta_2O_5. $TaCl_5$ and Ta-Ethoxide both need stringent handling to prevent reaction with moisture in air and oxide formation. The size and reactivity of the tantalum precursor plays a vital role in determining the reaction kinetics as

well as the final powder properties but not limited to specific surface area (size) and composition. The carbon sources used for the reactions vary from activated carbon to CNT's to specialized gel to mesoporous templates. For almost all the cases the carbon source acts as a reductant (where needed) as well as the carburization agent. Activated carbon is the most popular carbon source finding its use in solid state reactions as well as SHS and gels. Organic compounds with their low decomposition temperatures are also used. One of the advantages of using organic compounds is that the nascent carbon produced is highly reactive and since it is produced *in situ* it is generally more homogeneously distributed and hence improves the reaction kinetics and results in lowered reaction temperatures as well as shorter reaction times [22]. An important parameter for the final powder characteristics is the Ta:C ratio in the starting powder. Larger concentration of C moves the reaction forward but at the same time results in the formation of strong carbonaceous network in which the particles are embedded. As a result there is a critical stoichiometry above which the diffusive processes get kinetically limited [31]. The role of catalysts (metal as well as metal halides) is deemed very important for reducing the reaction temperatures as well as the final powder characteristics. But the exact role of the catalyst changes with synthesis method and needs to be closely looked into. The temperature range for the formation varies from 600 °C to 1500 °C with the maximum work being done at ~ 1000 °C. The atmosphere used also varies from reactive methane to inert argon to high pressure in an autoclave depending on the synthesis procedure. The heating though mostly limited to furnace with programmed heating rates can be done with microwave oven as well as a solar furnace.

The literature survey revealed that the process of formation of single phase, uniform sized, high specific area TaC nanoparticles has not been completely understood. Moreover, all the synthesis routes adopted so far require high temperature and/or complex monitoring processes. Solvothermal synthesis in autoclave [32] provides a single step route for synthesis of fine powder at low temperatures (600 °C). But the reaction kinetics as well as the parameters which control the size, stoichiometry and phase formation of TaC from this process still needs to be understood. The stoichiometry of TaC plays an important role in determining its properties in UHT as well as electro catalytic applications. Though some work has been done but the effect of processing parameters on reaction kinetics have not been studied in detail.

The goal of this study is to optimize the synthesis conditions of TaC using solvothermal synthesis route in an autoclave from three different commercially available Ta precursors,

namely, Ta-Ethoxide, Ta_2O_5 and $TaCl_5$. Acetone has been used as the carbon source and Mg as a catalyst. The effect of initial carbon concentration, temperature and time is studied. The synthesis protocol for obtaining the product with different carbon content has been studied. The synthesized carbides are characterized for structure, strain, stoichiometry, thermal stability, specific surface area and electro catalytic activity. The data obtained has been analysed to determine the reaction pathways for the TaC formation for all the Ta precursors in present investigation.

References:

[1]. J.B. Claridge, A.P.E. York, A.J. Brungs, M.L.H. Green, *Chem. Mater.* **12** (2000) 132-142.

[2]. J.-G. Choi, *J. Porous. Mater.* **20** (2013) 1059-1068.

[3]. Y.-J. Chen, J.-B. Li, Q.-M. Wei, H.-Z. Zhai, *Mater. Lett.* **56** (2002) 279-283.

[4]. N.A. Hassine, J.G.P. Binner, T.E. Cross *Int. J. Refract. Met. Hard Mater.* **13** (1995) 353-358.

[5]. E.J. Rees, K. Essaki, C.D.A. Brady, G.T. Burstein, *J. Power Sources* **188** (2009) 75-81.

[6]. P.M. Amaral, J.C. Fernandes, L.G. Rosa, D.Martinez, J. Rodriguez, N. Shohoji, *Int. J. Refract. Met. Hard Mater.* **18** (2000) 47-53.

[7]. A. Fukunaga, S. Chu, M.E. McHenry, *J. Mater. Sci. Lett.* **18** (1999) 431-433.

[8]. P.G. Li, M. Lei, Z.B. Sun, L.Z. Cao, Y.F. Guo, X. Guo, W.H. Tang, *J. Alloys. Compd.* **430** (2007) 237-240.

[9]. D.U. Yinxiao, L. Ming, Y. Hui, W. Xuefei, *J. Wuhan Univ. of Tech.-Mater. Sci. Ed.* **23** (2008) 779-782.

[10]. N.S. Alhajri, H.Yoshida, D.H. Anjum, A.T. Garcia-Esparza, J. Kubota, Kazunari Domen, K. Takanabe, *J. Mater. Chem. A* **1** (2013) 12606-12616.

[11]. P.G. Li, M.Lei, W.H. Tang, *Mater. Res. Bull.* **43** (2008) 3621-3626.

[12]. M. Lei, H.Z. Zhao, H. Yang, B. Song, W.H.Tang, *J. Eur. Ceram. Soc.* **28** (2008) 1671-1677.

[13]. T. Kim and M.S. Wooldridge, *J. Am. Ceram. Soc.* **84** (2001) 976-82.

[14]. T. Kim and M.S. Wooldridge, *Combust. Flame* **125** (2001) 965-973.

[15]. C.L. Yeh , E.W. Liu, *J. Alloys Compd.* **415** (2006) 66-72.

[16]. H.I. Won, N. Hayk, C.W. Won, H.H. Lee, *J. Mater. Sci.* **46** (2011) 6000-6006.

[17]. Y.-J. Lee, S.H. Kim, T.-H. Lee, H.H. Nersisyan, K.-H. Lee, M.-H. Han, S.-U. Jeong, K.-S. Kang, K-K. Bae, J.-H. Lee, *Chem. Eng. Sci.* **107** (2014) 227-234.

[18]. A.M. Nartowski, I.P. Parkin, M. Mackenzie, A. J. Craven, *J. Mater. Chem.* **11** (2001) 3116-3119.

[19]. K. Okuyama, I.W. Lenggoro, *Chem. Eng. Sci.* **58** (2003) 537- 547.

[20]. D.-H. Kwon, S.-H. Hong, B.-K. Kim, *Mater. Lett.* **58** (2004) 3863– 3867.

[21]. T. Ishigaki, S.-M. Oh, J.-G. Li, D.-W. Park, *Sci. Tech. Adv. Mater.* **6** (2005) 111-118.

[22]. H. Preiss, D. Schultze, P. Klobes, *J. Eur. Ceram. Soc.* **17** (1997) 1423-1435.

[23]. C.P. Souza, C. Favotto, P. Satre, A.L' Honore, M. Roubin, *Braz. J. Chem. Eng.* **16** (1999) 1-6.

[24]. H. Xiang, Y. Xu, L. Zhang, L. Cheng, *Scripta Mater*. **55** (2006) 339–342.

[25]. Y. Yosida, I. Oguro, *Physica C* **434** (2006) 138-140.

[26]. V.G. Sevast'yanov, E.P. Simonenko, N.A. Ignatov, Y.S. Ezhov, N.T. Kuznetsov, *Inorg. Mater.* **46** (2010) 495-500.

[27]. M. Ma, W. Shen, P. Zhang, J. Zhang, Q. Wang, C. Ge, *Mater. Lett.* **65** (2011) 96-99.

[28]. M.J.S. Lima, M.V.M. Souto, A.S Silva, U.U. Gomes, C. Pereira de Souza, *Tecnol. Metal. Mater. Miner.* **12** (2015) 304-309.

[29]. Y. Lu, L. Ye, W. Han, Y. Sun, W. Qiu, T. Zhao, *Ceram. Int.* **42** (2015), 12475-12479.

[30]. J.P. Kelly, R. Kanakala, O.A. Graeve, *J. Am. Ceram. Soc.* **93** (2010) 3035–3038.

[31]. J.P. Kelly, O.A. Graeve, *J. Am. Ceram. Soc.* **94** (2011) 1706-1715.

[32]. J. Ma, Y. Du, M. Wu, M.C. Pan, *Mater. Lett.* **61** (2007) 3658-3661.

[33]. D.J. Ham, J.S. Lee, *Energies* **2** (2009) 873-899.

[34]. Y. Zhong , X. Xia, F. Shi , J. Zhan , J. Tu, H.J. Fan, *Adv. Sci.* **3** (2016) 1500286 1-28.

[35]. D.M. Li, R. Hernberg, T. Mantyla, *Diamond Relat. Mater.* **7** (1998) 1709-1713.

[36]. C. He, J. Tao, *Chem. Commun.* **52** (2016) 8810-8813.

CHAPTER 3

Materials and Methods

Overview

The protocols followed for the synthesis of TaC nanopowders from different precursors are presented in this chapter. Details of different characterization techniques along with the procedure adopted to characterize the samples have been described. The commonly used techniques in the present investigation are: X-ray diffraction (XRD), Thermal analysis (DSC/TGA/DTG), Field-Emission Scanning Electron Microscope (FE-SEM), Transmission electron microscopy (TEM), BET analysis and Electro chemical measurements.

3.1 TaC powder synthesis

3.1.1 Precursors

For the synthesis of TaC nano particles, Ta-Ethoxide (Ta-E, $Ta_2(C_2H_5O)_5$, 99.99%, Sigma Aldrich), Tantalum (V) Oxide (Ta_2O_5, 99.99%, Sigma Aldrich), Tantalum Chloride ($TaCl_5$, 99.99%, Sigma Aldrich), Mg (99%, Loba Chemie), acetone (99%, Loba Chemie), HCl (99%, S.D. Fine Chemicals) are used as per the requirement without any further purification.

3.1.2 Methodology

The synthesis route followed in the present work was the single step chemical reaction method inside a specially designed 20 ml steel autoclave [1-4]. The precursor in each case was mixed with the desired amount of magnesium and acetone (if required) and the autoclave was sealed. The entire assembly was placed inside the resistance heating furnace. The temperature of the furnace was raised from room temperature to the required temperature slowly (5 °C/min). After soaking at the final temperature for the required time, the autoclave was then allowed to cool to room temperature slowly inside the furnace. In some of the experiments autoclave was removed from furnace and cooled in air (quench cooled). The resultant product was collected and leached with diluted HCl (1:1) to remove magnesium oxide (MgO) and/or magnesium chloride ($MgCl_2$) and unreacted Mg. After leaching, the powder was washed several times with double distilled water to remove any traces of unreacted acid. Finally, the powder was washed with acetone and dried in vacuum at 100 °C.

3.1.2.1 Tantalum ethoxide precursor

In this case the Ta-E has been used as Ta precursor as well as carbon source. Here the *in situ* carbon, produced during the decomposition of Ta-E, has been utilized for the reduction and carburization in the presence of reducing agent Mg to get TaC nanopowder. For the synthesis of TaC nano powder, Ta-E and Mg in molar ratios of 1:7 are mixed. The autoclave was maintained at the final temperature of 800 °C for 2, 5, 8, 10 and 12 hrs. Some low temperature studies were also carried out in conjunction with the above for the determination of reaction pathways.

3.1.2.2 Tantalum (V) oxide precursor

For the Ta_2O_5 precursor acetone was used as the carbon source. The *in situ* hydrogen and carbon, produced during the decomposition of acetone, have been utilized for the reduction

and carburization in the presence of reducing agent Mg at 800 °C to get TaC nanopowder. For the synthesis of TaC nano powder, Ta_2O_5, Mg and Acetone in molar ratios of 1:12:y were mixed and sealed in the autoclave. The amount of acetone (y) in the initial mixture was fixed such that tantalum to carbon ratio varied from 1 to 90. The furnace was maintained at the extreme temperature for different durations (1 - 15 h). Low temperature studies were also carried out in conjunction with the above for the determination of formation mechanism for the carbide nano particles.

3.1.2.3 Tantalum (V) chloride precursor

The mixture in the autoclave for this case was $TaCl_5$, Mg and acetone in molar ratios of 1:9:1. The autoclave is maintained at the desired temperatures (650 °C, 700 °C, 800 °C) for different durations (1 - 12 h). The low temperature studies carried out in conjunction with the above allowed for the determination of conversion mechanism for the carbide nano particles.

3.2 Materials characterization

3.2.1 X-ray diffraction (XRD) study

The XRD study of the synthesized products was done to identify and structurally characterize the existing crystalline phases. In this technique the intensity of the scattered X-ray is measured as a function of the angle between X-ray source and the sample, wavelength as expressed according to Bragg´s law [5]:

$$n\lambda = 2d\,\mathrm{Sin}\theta \qquad (3.1)$$

where, n is an order of reflection, λ is wavelength of the incident X-ray, d is the spacing between the lattice planes, and θ is the angle between the incident ray and set of parallel atomic planes.

The XRD of the samples was performed using PANalytical Xpert-Pro with CuKα radiation (λ = 1.5406 Å) obtained from the copper target using an inbuilt Ni filter. The X-ray powder diffraction data were collected for all samples at room temperature between 20 °≤ 2θ ≤ 80 ° with a step size of 0.0130 ° (2θ). Phase identification from the ICDD data base was further confirmed by Rietveld refinement of the XRD patterns.

Line profile analysis of XRD data allows for meaningful determination of size and strain of the product which can be used to correlate the microstructure and properties of the synthesized powders [6]. Scherrer relation is still the most commonly used method for the determination of domain size for coherent scattering in the given sample. The domain size obtained from the Scherrer relation is a volume weighted quantity. Scherrer relation uses full width at half maxima (FWHM) of the XRD peaks for the determination of domain size, t:

$$t = \frac{K\lambda}{FWHM\ Cos\theta} \tag{3.2}$$

Where, K: Shape factor, θ: Bragg angle, λ: X-ray wavelength.

Wilson defined "integral breadth apparent size" where the integral breadth, β (A/I_0, A: Area of the peak, I_0: Maximum Intensity) is used instead of FWHM to define the volume weighted crystallite size, $<D_v>$ [7]:

$$\langle D_V \rangle = \frac{K\lambda}{\beta\ Cos\theta} \tag{3.3}$$

For both the above cases the peak broadening is attributed to the coherently diffracting domain size. Stokes and Wilson gave the relation for broadening solely due to strain [7]. The maximum strain, e, is given by:

$$\beta = 4\ e\ tan\theta \tag{3.4}$$

Willamson-Hall plot is used extensively to separate the size and strain effects [7,8]:

$$\beta\ Cos\theta = \frac{K\lambda}{\langle D_V \rangle} + \text{ e } 4\text{Sin}\theta \tag{3.5}$$

In the above equation it is assumed that the strain and size broadening functions are Lorentzian in nature. Since Lorentzian or Gaussian functions cannot satisfactorily model the specimen broadening exclusively, it is assumed that both size and strain effects are approximated by either Voigt or its approximation - pseudo-Voigt function [6]. In the present case individual peaks have been fitted with pseudo-Voigt function which is a linear combination of Lorentzian (L(x)) and Gaussian (G(x)) functions [6, 9]:

$$F(x) = \eta\, L(x) + (1-\eta)\, G(x) \tag{3.6}$$

Where, η: mixing parameter.

For the peak fitting the peak shape is assumed to be symmetrical. The split pseudo-Voigt function is known to provide better fits. Here, the results after best-fit were chosen taking into account the minimum error as well as realistic values for the fitting parameters. The obtained integral breadths are a combination of instrumental and specimen broadening so the instrumental corrected integral breadths were estimated from the measured data [11].

Single line analysis: De Keijser et al. [9] in the case of a single line analysis, assumed that the Lorentz component of the line profile is solely due to the crystallite size and that the Gaussian contribution arises from the strain. Hence the apparent domain size for a *hkl* reflection can be deduced using the relation (3.3) replacing β by β_L and the strain is obtained using the relation (3.4) replacing β by β_G, β_L and β_G being the Lorentzian and Gaussian parts of the integral breadth. For the case of a Gaussian micro-strain distribution it is possible to calculate the local root-mean-square strain [11]:

$$\langle \epsilon^2 \rangle^{1/2} = \sqrt{\frac{2}{\pi}}\, e \tag{3.7}$$

Voigt multiple-line integral-breadth methods: The Lorentzian and Gaussian components of the size and strain integral breadths follow the convolution principle and the various components can be separated. Warren definition of mean-square strain requires that the Lorentz and Gauss distortion integral breadths depend differently on s ($= \frac{2\,Sin\theta}{\lambda}$) and the multiple-line Voigt method by Langford becomes [9, 12]:

$$\beta_L = (\beta_{SL} + \beta_{DL}\, \frac{s^2}{s_0^2}) \tag{3.8}$$

$$\beta_G^2 = \left(\beta_{SG}^2 + \beta_{DG}^2\, \frac{s^2}{s_0^2}\right) \tag{3.9}$$

Where,

β_{SL} , β_{DL} are modified Lorentzian components of size and strain integral breadth.

β_{SG} , β_{DG} are modified Gaussian components of size and strain integral breadth.

and, $$Modified\ \beta = \frac{\beta(2\theta)\ Cos\theta}{\lambda} \quad (3.10)$$

This method is called "Double–Voigt" method. β_L and β_G^2 are plotted *w.r.t.* s^2 and the corresponding strain and size components β_{SL}, $\beta_{DL}(hkl)$, β_{SG} , $\beta_{DG}(hkl)$ are obtained. The analytical expressions for the volume weighted domain size, $<D_v>$, strain, $<\varepsilon^2>^{1/2}$ and size coefficients, $A_s(L)$ are [6,7]:

$$< D_V >= \left[\frac{\beta_{SL} + (\beta_{SL}^2 + \beta_{SG}^2)^{1/2}}{2}\right]^{-1} \quad (3.11)$$

$$< \varepsilon^2(L) >= \frac{1}{s^2}\left[\frac{\beta_{DG}^2}{2\pi} + \frac{\beta_{DL}}{\pi^2}\frac{1}{L}\right] \quad (3.12)$$

$$A_s(L) = \exp(-2L\beta_{SL} - \pi L^2\beta_{SG}^2) \quad (3.13)$$

Equation 3.11 is used to determine the r.m.s. strain distribution *w.r.t.* size (L) and direction. The initial slope of the $A_S(L)$ vs L graph is used to determine the surface weighted domain size, $<D_s>$ [8,6]. Surface weighted domain size determination of the powder is important for the applications where the active surface area is important e.g. catalysis [11].

Rietveld refinement of XRD data: The Wyckoff positions used for Rietveld refinement of XRD data are 4a (0,0,0) for Ta and 4b (0.5, 0.5, 0.5) for C. The XRD data is best fitted with cubic space group Fm-3m. The lattice parameter of the synthesized samples from the Rietveld refinement have been used to determine ***x***, the fraction of C in the TaC_x for all the synthesized powders [12]:

$$\text{a (Å)} = 4.3007 + 0.1563\ \text{x} \quad (3.14)$$

3.2.2 Thermal analysis

Thermal analysis of the specimen involves the monitoring of the changes in the properties of the material with predetermined change in the temperature in a controlled atmosphere [13]. In the present work the simultaneous differential scanning calorimetry (DSC) and thermo

gravimetric analysis (TGA) (DSC/TG) have been employed to determine the thermal stability and oxidation resistance of the obtained powder. In TGA the amount and rate of change in the weight of the material is determined as a function of temperature or time. The technique is mainly used to characterize materials which exhibit weight loss or gain in the prescribed temperature regime. TGA is used primarily to determine the composition, predict thermal and/or oxidative stability, moisture and volatiles content, decomposition kinetics and the effect of reactive or corrosive atmospheres on the materials. TGA can provide information in two forms: mass loss/gain as a function of either temperature or time which is a direct indication of mass loss/gain and the derivative of mass change (DTG) as a function of temperature or time which helps to pinpoint any shoulders present [14,15]. DSC measures the energy flow into a substance in comparison with a reference material as a function of temperature while the substance and reference are subjected to a controlled temperature program. It allows for the determination of temperature at which any event either absorbs or releases heat. The area under the endotherm or exotherm peak is also related to the enthalpy (ΔH) of the thermal event. DSC is used primarily to determine the phase transition temperatures, study of order disorder transitions, chemical reactions and for heat capacity measurements. DSC/TG allows for the simultaneous measurement of these two material properties and this not only improves productivity but also simplifies interpretation of the results [13,16]. The complimentary information obtained allows differentiation between endothermic and exothermic events which have no associated weight loss (e.g., melting and crystallization) and those which involve a weight loss (e.g., degradation). The DSC/TG analysis of the synthesized powder samples was done at heating rate of 5 °C/min in the temperature range 50-900 °C in air atmosphere by NETZSCH STA 449F3 using alumina crucible.

3.2.3 Field Emission Scanning Electron Microscopy (FE-SEM)

In electron microscopy the specimen is illuminated with a beam of electrons. The strength of electron microscopy techniques lies in the fact that the electrons can be focused using electromagnetic lenses and the resolution is no longer limited by the diffraction. In Scanning Electron Microscope (SEM) a focused beam of electrons accelerated at moderately high energy (few hundred eV to 40 keV) is positioned accurately (0.4 nm to 5 nm) and then raster scanned on the sample by electromagnetic fields. When the beam impinges at a point on the surface it interacts via a variety of mechanisms which could be either elastic or inelastic.

Inherent versatility of the SEM is due to these multiple signals generated as well as the wide magnification range and excellent depth of field [17]. Depending on the output signal being monitored the SEM can provide information related to topographical features, morphology, phase distribution, compositional differences, crystal structure, crystal orientation and the presence and location of electrical defects. For the Field Emission SEM (FE-SEM) the electron source is a field emission gun. The field emission gun produces an electron beam which is smaller in diameter, more coherent and has up to three orders of magnitude greater current density as compared to conventional thermionic electron gun. This results in significantly improved signal-to-noise ratio and spatial resolution. For FE-SEM analysis, the powder samples were dispersed in ethanol by ultra-sonication for 20 min. One drop of the suspension was dropped on the carbon coated copper TEM grid and the ethanol is allowed to evaporate at room temperature. The sample coated grid is further gold coated before imaging. The Ta-E precursor samples were analyzed with QUANTA 200 FEG FE-SEM operating at 20 kV. The Ta_2O_5 precursor samples were analyzed with SIGMA Carl Zeiss FE-SEM operating at 5 kV and the $TaCl_5$ precursor samples were analysed with Hitachi SU 8010 FE-SEM operating at 15 kV.

3.2.4 Transmission Electron Microscopy (TEM)

For Transmission Electron Microscopy (TEM) the beam of electrons is transmitted through the ultra-thin (<100 nm) specimen. This facilitates to increase the spatial resolution in imaging (down to individual atoms) as well as the possibility of carrying out diffraction from nano-sized volumes. The signal due to un-scattered electrons and elastically scattered electrons is used to produce the magnified image and the diffraction pattern respectively. High resolution transmission electron microscopy (HRTEM) provides information about the structural defects, interfaces as well as individual grains having diameter of a few nanometres and lattice spacing [18]. For TEM analysis, the powder samples were dispersed in ethanol by ultra-sonication for 20 min. One drop of the suspension was dropped on the carbon coated copper TEM grid and allowed to evaporate the ethanol at room temperature. The microstructural features of the synthesized powder samples were analysed with JEOL 2100F operating at 200 kV. The TEM/HR-TEM data was analysed using the Carl Zeiss Axio Vision 4 software.

3.2.5 N_2 Physisorption

Apart from phase and size/morphology, the properties of the powder are significantly influenced by specific surface area (surface area per unit mass), and porosity (fraction of the total void volume with respect to the volume of the material). For a powder the surface area, particle size, morphology, surface texture (pore size, pore size distribution and pore shape) and porosity are all interrelated properties and are studied. Reversible gas adsorption or physical adsorption method is generally used for characterization of the above stated properties for powders [19]. The powder is exposed to an absorptive gas at specific conditions and amount of a gas absorbed on the surface is measured as a function of the pressure of the gas (adsorption isotherm). Nitrogen gas (due to its permanent quadrupole moment) forms well defined monolayers/multilayers on most surfaces with the multilayer structure being rather insensitive to the nature of the adsorbent and hence is the most popular gas used for obtaining the adsorption/desorption isotherms for the powders [20]. As per IUPAC conventions the porous materials can in general be described by 6 different isotherm types (Figure 3.1, Table 3.1). IUPAC also has an empirical classification of the hysteresis loops which gives information about the texture of the adsorbent (Figure 3.2, Table 3.2).

Specific surface area (SSA) for the specimens is obtained from the adsorption/desorption isotherms using the Brunauer-Emmett-Teller (BET) analysis method [19-21]. Barrett-Joyner-Halenda (BJH) analysis leads to pore-size distribution independent of external area (due to particle size of the sample) [22]. So BJH analysis is used to determine pore area and specific pore volume. The N_2 sorption studies for surface analysis of synthesized samples were conducted using a Tristar 3000 (Micromeritics) to determine the Brunauer–Emmett–Teller (BET) surface area, the pore size, and the pore volume at 77 K. Before the exposure to N_2 the samples are degassed at 120 °C for 2 h.

3.2.6 Electro chemical measurements

For most of the catalytic applications, nanoparticles are preferred due to inherent enhancement of expected active sites. In this work the different TaC synthesized samples are expected to possess different catalysis activities due to differences in size and carbon content both inside as well as outside the particles. The cyclic voltammetry technique (CV) and linear sweep voltammetry (LSV) are two of the most prevalent techniques for the electrochemical measurements.

Table 3.1: Classification of physical adsorption isotherms.

Type	Interpretation
I	Microporus material
II	Non-porous or macroporous material with a high energy of adsorption
III	Non-porous or macroporous material with a low energy of adsorption
IV	Mesoporous material with capillary condensation and with high energy of adsorption
V	Mesoporous material with capillary condensation and with low energy of adsorption
VI	Temperature is below the adsorptive triple point or multiple pore sizes.

Table 3.2: Interpretation of hysteresis loop types for physical adsorption isotherms.

Type	Interpretation
H1	Regular even pores without interconnecting channels
H2	Disordered pores with possible interconnecting channels
H3	Non-rigid aggregates of plate-like particles (slit-shaped pores)
H4	Slit-like pores for the type I adsorbent–adsorbate pair

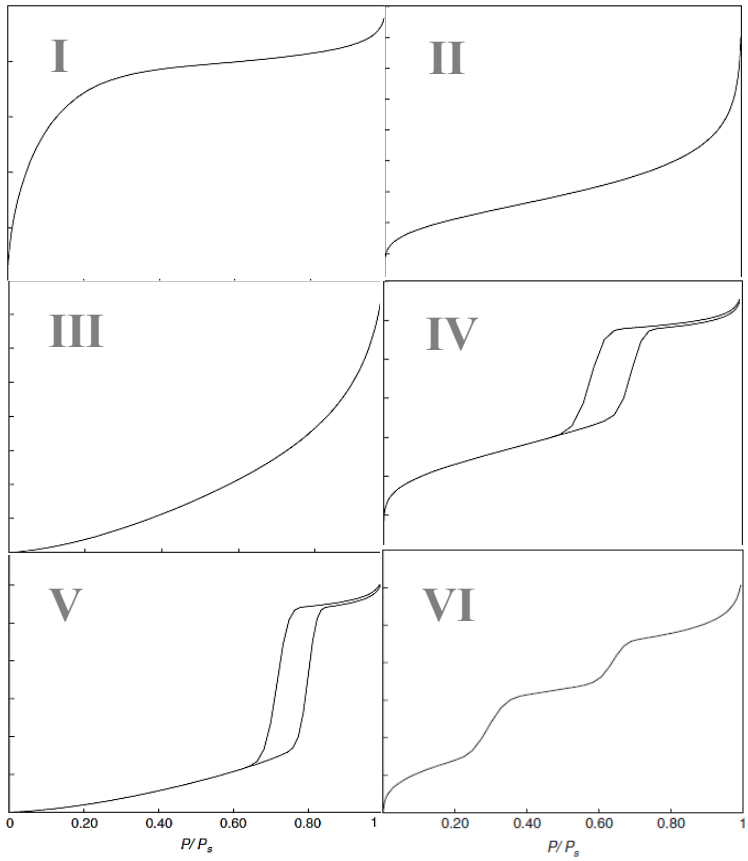

Figure 3.1: Physical adsorption isotherms from IUPAC [19].

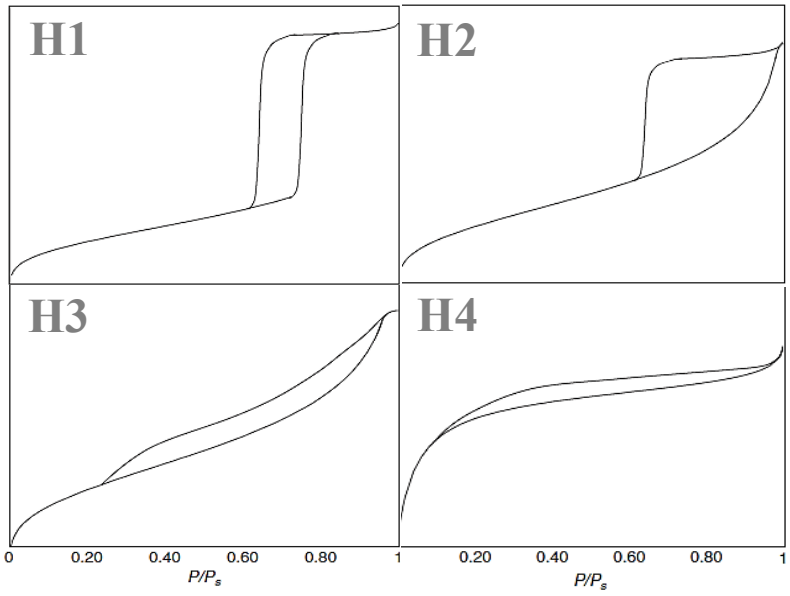

Figure 3.2: Hysteresis loops classification from IUPA [19].

In a typical experiment, the working electrode´s potential is controlled relative to a reference electrode (RE) such as a saturated calomel electrode (SCE) or reversible hydrogen electrode (RHE) and cycled linearly between two potential values at which the oxidation and the reduction occur. A CV curve is acquired by measuring the current at the working electrode during the potential scan [23]. It is a (mostly) reversible technique and the electrochemical properties of redox active species display a reversible wave within a specified wide potential range. The CV is widely used to diagnose the mechanisms of given electrochemical reaction, for the identification of species present in solution and for the semi-quantitative analysis of reaction rate constants and electrode reactions involving electron transfer. It provides a direct estimation of electrode reversibility, because the potentials at which oxidation and reduction occur are observed directly [24]. In LSV the voltage is swept linearly in time.

In current work, the electrochemical measurements were performed using the Bio-Logic EC Lab SP300 setup by standard three electrode electrochemical cell. For CV and LSV measurements sample/catalyst loaded glassy carbon electrode (GCE) with an area of 0.07065 cm^2 is used as working electrode. High purity graphite rod is used as the counter electrode and Reversible hydrogen electrode (RHE) as the reference electrode. The electrodes were immersed in 0.5 mol/L H_2SO_4 solution and LSV and CV curves were recorded at room temperature between -0.6 and +0.2 V with the scan rates of 2 mV/s and 5 mV/s respectively. Before the HER measurements, the electrodes were pre-treated by cycling the potential between -0.7 and +0.2 V at a sweep rate of 50 mV/s for 30 cycles to activate the catalysts, remove surface contamination and stabilize electrochemical current [25].

3.2.6.2 Electrode fabrication

The 3 mm diameter glassy carbon electrode (GCE) was pre-cleaned with emery paper and acetone. Typically 6 mg powder sample was mixed with 1mL of ethanol and treated ultrasonically for 20 min for uniform dispersion. 10 μL of this mixture was then dropped onto the top-surface of GCE and allowed to dry at room temperature. Finally a drop of 10 μL of Nafion® 117 solution (Sigma Aldrich) was dropped onto the top surface and left in air for overnight drying. This provides us with the loading of 0.63 mg/cm^2.

References:

[1]. A. Kumar, K. Singh, O.P. Pandey, *Physica E* **41** (2009) 677-684.

[2]. G. Singla, K. Singh, O.P. Pandey, *Ceram. Int.* **40** (2014) 5157–5164.

[3]. L.K. Brar, G. Singla, O.P. Pandey, *RSC Adv.* **5** (2015) 1406–1416.

[4]. L.K. Brar, G. Singla, O.P. Pandey *RSC Adv.* **6** (2016) 109174-109184.

[5]. V. Raghavan, *Materials Science and Engineering*, PHI learning Pvt. Ltd, Delhi, India (2015).

[6]. D. Balazar, In: R.L. Snyder, J. Fiala and H.J. Bunge, editors, *Defect and Microstructure Analysis by Diffraction* Oxford University Press, Oxford, UK (1999).

[7]. S. Vives, E. Gaffet, and C. Meunier, *Mater. Sci. and Eng. A* **366** (2004) 229–238.

[8]. G. Singla, K. Singh and O. P. Pandey, *Appl. Phys. A* **113** (2013) 237-242.

[9]. K. Santra, P. Chatterjee and S. P. S. Gupta, *Bull. Mater. Sci.*, 2002, **25** (2002) 251–257.

[10]. T.H. De Keijser, J.I. Langford, E.J. Mittemeijer, B.P. Vogels, *J. Appl. Cryst.* **15** (1982) 308-314.

[11]. H.G. Merkus *Particle Size Measurements: Fundamentals, Practice, Quality* Springer Science & Business Media B.V, Dordrecht, Netherland (2009).

[12]. A.L. Bowman, *J. Phys. Chem.* **65** (1961) 1596-1598.

[13]. P.J. Haines, *Principles of Thermal Analysis and Calorimetry* Royal Society of Chemistry, Cambridge, UK (2002).

[14]. H.K.F. Cheng, M.F. Chong, E. Liu, K. Zhou, L. Li, *J. Therm. Anal. Calorim.* **117** (2014) 63–71.

[15]. R. Díaz-Ayala, L. Arroyo-Ramírez, R.G. Raptis, C.R. Cabrera, *J. Therm. Anal. Calorim.* **115** (2014) 479–488.

[16]. M.E. Brown, *Handbook of Thermal Analysis and Calorimetry* Elsevier B.V., Amsterdam, Netherlands (1998).

[17]. P.R. Khangaonkar, *An Introduction to Materials Characterization* Penram International Publishing (I) Pvt Ltd, Mumbai, India (2010).

[18]. D.B. Williams, C.B. Carter, *Transmission Electron Microscopy: A Textbook for Materials Science* Springer, New York (2009).

[19]. J.B. Condon, *Surface Area and Porosity Determinations by Physisorption - Measurements and Theory* Elsevier B.V., Amsterdam, Netherlands (2006).

[20]. K. Sing, *Colloids Surf., A* **187–188** (2001) 3–9.

[21]. S.J. Gregg, K.S. W. Sing *Adsorption, Surface Area and Porosity* Academic Press Inc., London, UK (1982).

[22]. S. Lowell, J.E. Shields, *Powder Surface Area and Porosity* Chapman and Hall, London, UK (1984).

[23]. D.R. Crow, *Principles and Applications of Electrochemistry* Chapman & Hall/CRC, Boca Raton, USA (1994).

[24]. C.M.A. Brett, A.M.O. Brett, *Electrochemistry Principles, Methods, and Applications*, Oxford University Press, New York, USA (1993).

[25]. C. He and J. Tao, *Chem. Commun.*, **52 (**2016) 8810-8813.

CHAPTER 4
Nano TaC from Tantalum Ethoxide

Overview

This chapter presents the synthesis and characterization of the nano TaC from the Tantalum Ethoxide precursor. The line analysis results from the XRD data for the synthesized samples have been discussed. The lattice carbon content (***x***) of the TaC_x nanopowders, size and strain has been used to determine the evolution of the nanopowders with time as well as temperature. Based on XRD results the formation mechanism of the nano particles has been proposed. From the thermal analysis results, the stability of the synthesized powders over range of temperature(s) has been evaluated. FE-SEM and TEM results have been presented and discussed to analyse the microstructure of the synthesized powders and to confirm the crystal structure of product phase by measuring the lattice fringing using HRTEM. Surface area and pore size distribution of the synthesized samples have been analysed by BET technique.

4.1 Thermal analysis of Tantalum Ethoxide

Tantalum Ethoxide (Ta-E) was analysed by simultaneous DTA/TG in air to determine its thermal stability and oxidation behaviour. The DTA-TG-DTG curves obtained for Ta-E are given in Figure 4.1. Initial mass loss in TG is attributed to loss of water and other volatile adsorbates. The mass loss in TGA curve at 305 °C with corresponding exothermic DTA peak signals the decomposition of Ta-E with evolution of CO_2 and H_2O (Equation 4.1). The exothermic DSC peak corresponding to 765 ^{0}C is the signature of crystalline Ta_2O_5 formation [1].

$$Ta_2(OC_2H_5)_{10} + 30\ O_2 \rightarrow Ta_2O_5 + 20\ CO_2 + 25\ H_2O \qquad (4.1)$$

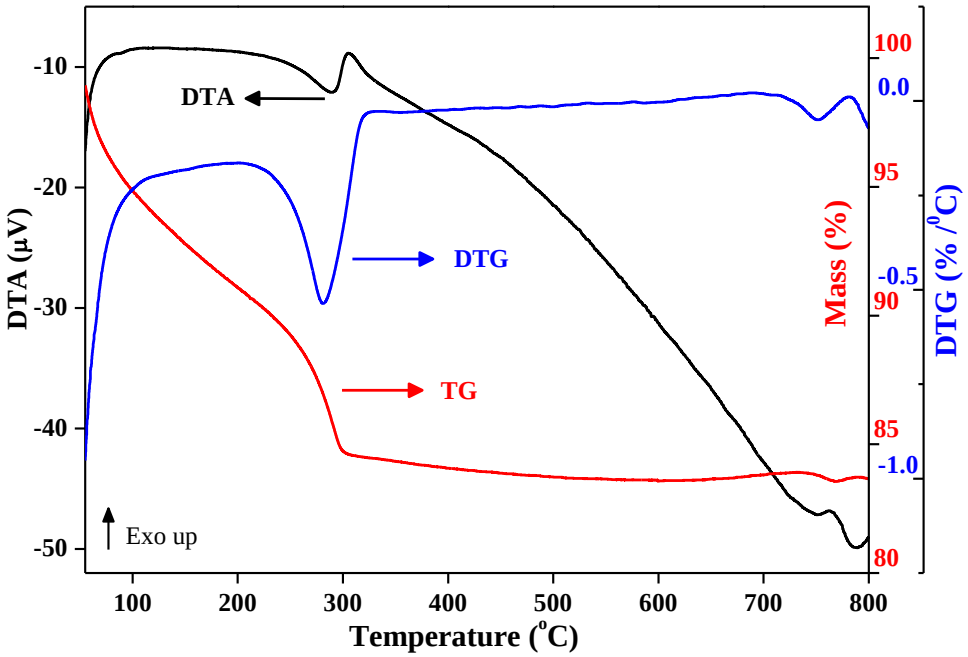

Figure 4.1: DTA-TG-DTG of Ta-Ethoxide in air showing different transition points.

From the above thermal analysis it is observed that the final phase transformation to Ta_2O_5, through dissociation of T-E, occurs at 765 °C. So to achieve the formation of TaC the reduction and carburization experiments were planned at 800 °C to ensure that the proper reaction temperature is achieved. Low temperature experiments have also been done to establish the mechanism of TaC formation. The details of this have been described in section 4.7.

4. 2 Samples

In order to perform the experiments as described in the previous section the synthesis parameters viz. time and temperature were varied. Table 4.1 gives the details of the synthesis conditions for the samples.

Table 4.1: List of the samples along with synthesis conditions.

Sample Name	Soaking Time (h)	Temperature (°C)
E02h5	02	500
E10h7	10	700
E02h8	02	800
E05h8	05	800
E08h8	08	800
E10h8	10	800
E12h8	12	800

4.3 X-ray diffraction analysis (XRD) of the synthesized product

The XRD data for the samples synthesized at 800 °C after acid leaching is shown in Figure 4.2. Cubic TaC (ICDD Pattern – 01-089-2870) is the dominant phase in all the samples. The minor phases are Ta_4O (ICDD Pattern – 00-015-0243) and hexagonal Ta_2C (ICDD Pattern – 00-032-1280). Table 4.2 gives details of the minor phases present for all the samples. All the synthesized samples also contain hexagonal carbon (ICDD Pattern – 00-026-1076). Increase in the soaking time results in change of the locations and widths of the peaks for the dominant phase as well as the concentration of minor phases.

XRD patterns reveal that nearly 90% conversion to TaC has taken place even for E02h8 sample. However, the absence of Ta_4O phase only for the E10h8 sample indicates that the complete conversion needs 10 h (9 h data shows small peak of Ta_4O, data not shown). The intensity of Ta_2C is also smallest for this sample. Further increase in soaking time results in

enhancement of the Ta_2C peak indicating the removal of carbon from the TaC and a corresponding increase in the concentration of Ta_2C phase.

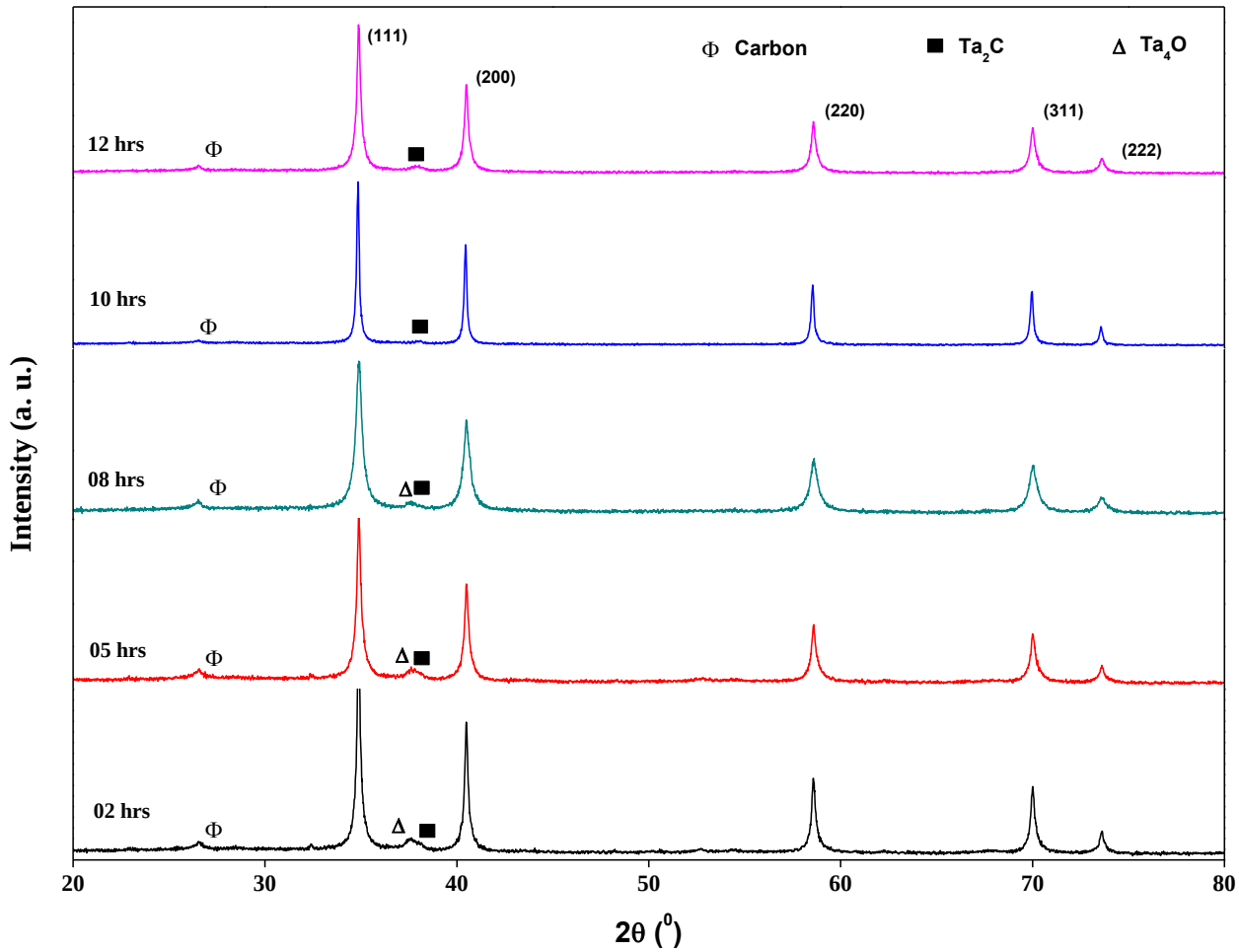

Figure 4.2: XRD results of acid leached samples synthesized from Ta-E precursor with different soaking times at 800 °C. TaC (peaks indexed) is the major phase formed for all the samples.

Table 4.2: The Minority phase(s), reliability factors for Rietveld refinement, lattice parameters and calculated lattice carbon content in TaC_x phase of the synthesized samples.

Sample Name	Minor Phases	χ^2	R_{wp}	a (nm)	*x*
E02h8	Ta_4O, Ta_2C	2.10	8.47	0.445547	0.990
E05h8	Ta_4O, Ta_2C	2.38	9.16	0.445557	0.991
E08h8	Ta_4O, Ta_2C	2.14	8.56	0.445533	0.989
E010h8	Ta_2C	1.99	7.57	0.445738	1.000
E12h8	Ta_2C	1.72	8.24	0.445532	0.985

Figure 4.3(a) gives the Rietveld refinement plots for the E10h8 sample. Table 4.2 gives the lattice parameter, ***a***, R_{WP} and χ^2 – values obtained from the Rietveld refinement of the XRD data. Table 4.2 also lists the lattice carbon content, ***x***, for TaC_x in each sample.

The data in Table 4.2 clearly shows that $TaC_{1.0}$ (ICDD – 01-089-2870) phase is formed for the E10h8 sample. Further increase in the soaking time decreases the lattice constant supporting the conjecture about the carbon loss from TaC as the soaking time is increased beyond 10 h.

Single line and double-Voigt integral breadth analysis methods have been used to determine the strain and size of the synthesized samples from the XRD profiles. Peak position (2θ), gaussian integral breadth (β_G) and lorentzian integral breadth (β_L) of the Bragg peaks from the XRD data were determined by profile fitting technique using pseudo-Voigt function. Figure 4.3(b) shows the results obtained from the fitting of pseudo-Voigt function for the (111) peak for the E10h8 sample. Figure 4.4 give the single line and double-Voigt integral breadth method analysis graphs for the E10h8 sample. Similar graphs have been used to analyse all the samples. Table 4.3 gives the details of the size and strain values obtained for the single line and double-Voigt integral breadth methods.

Table 4.3: Structural data of synthesized samples as determined from the single line and double-voigt integral breadth methods from XRD profile analysis. (D_v and D_s are the volume weighted and surface weighted sizes obtained from the double-voigt analysis)

	Single-Line Analysis			**Double-Voigt Analysis**	
Sample Name	**Crystallite size (nm)**	**Max Strain (x 10^{-4})**	**r.m.s. Strain (x 10^{-4})**	**D_v (nm)**	**D_s (nm)**
E02h8	72	2.14	1.71	22	13
E05h8	39	2.37	1.89	20	12
E08h8	39	0.71	0.56	21	8
E10h8	113	2.53	2.02	45	25
E12h8	49	2.30	1.83	21	12

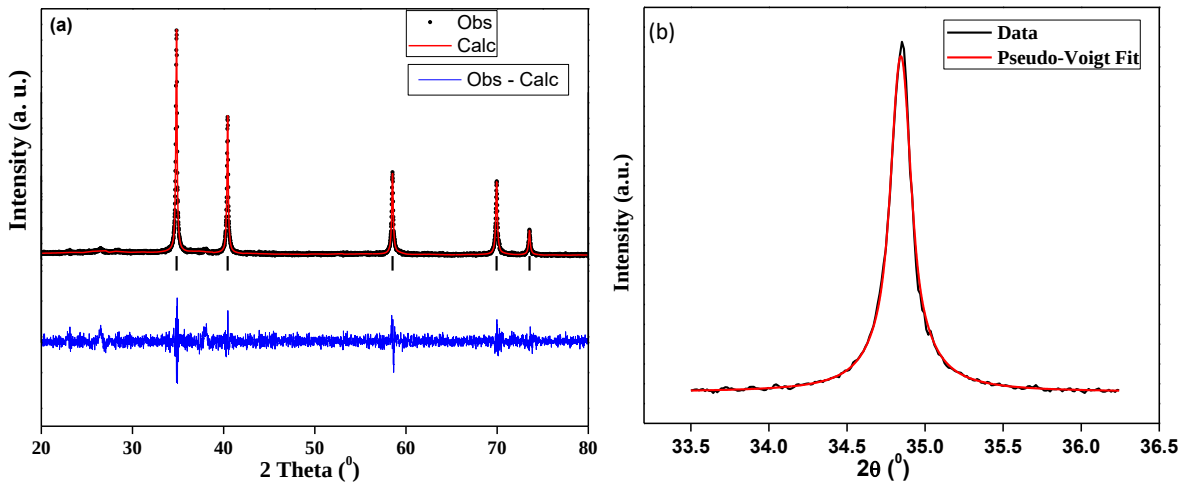

Figure 4.3: (a) Rietveld refinement plots for the E10h8 sample. Measured data are indicated by dots and calculated data by solid curve. The difference between the measured and calculated data is given below as a plot, and tick marks indicate allowed peak positions. (b) The result of the pseudo-Voigt curve fit routine for the (111) peak of E10h8 sample.

A comparison of the volume weighted particle sizes (D_V) and strains obtained from single line method and the double-Voigt method shows that the single line method which takes into consideration only the Lorentzian contributions to size and Gaussian contributions to strain ends up overestimating the size and underestimating the strain in the samples.From the single line analysis the strain obtained for the E08h8 sample is minimum and the size is comparable to 2 h and 5 h samples. This is counterintuitive since the peaks for 8h sample are broadest (Figure 4.2). Double-Voigt analysis shows that though the volume weighted column lengths for 2 h, 5 h and 8 h samples are comparable but the surface weighted column length is actually smallest for 8h sample (Figure 4.5(a)). This implies that the particle size and hence the surface area will be largest for 8h sample.

The XRD data (Table 4.2-3) clearly shows that the unit cell size, particle size and strain are maximum for the E10h8 sample. The double-Voigt method allows for the determination of the r.m.s. strain distribution *w.r.t.* size and direction so the strains for different planes within the particles for synthesized samples are compared. For the 2 h, 5 h, 8 h and 12 h samples the r.m.s. strains are isotropic. Inset in Figure 4.5(b) shows the variation of the strain in all the directions for E08h8 sample. But for the E10h8 sample the strain for the (111) plane is very large (Figure 4.5(b)) as compared to that for the other planes. The large amount of strain present in (111) plane may be due to complete filling of octahedral voids with carbon for this sample. The same may also be responsible for increasing the unit cell size and the particle size.

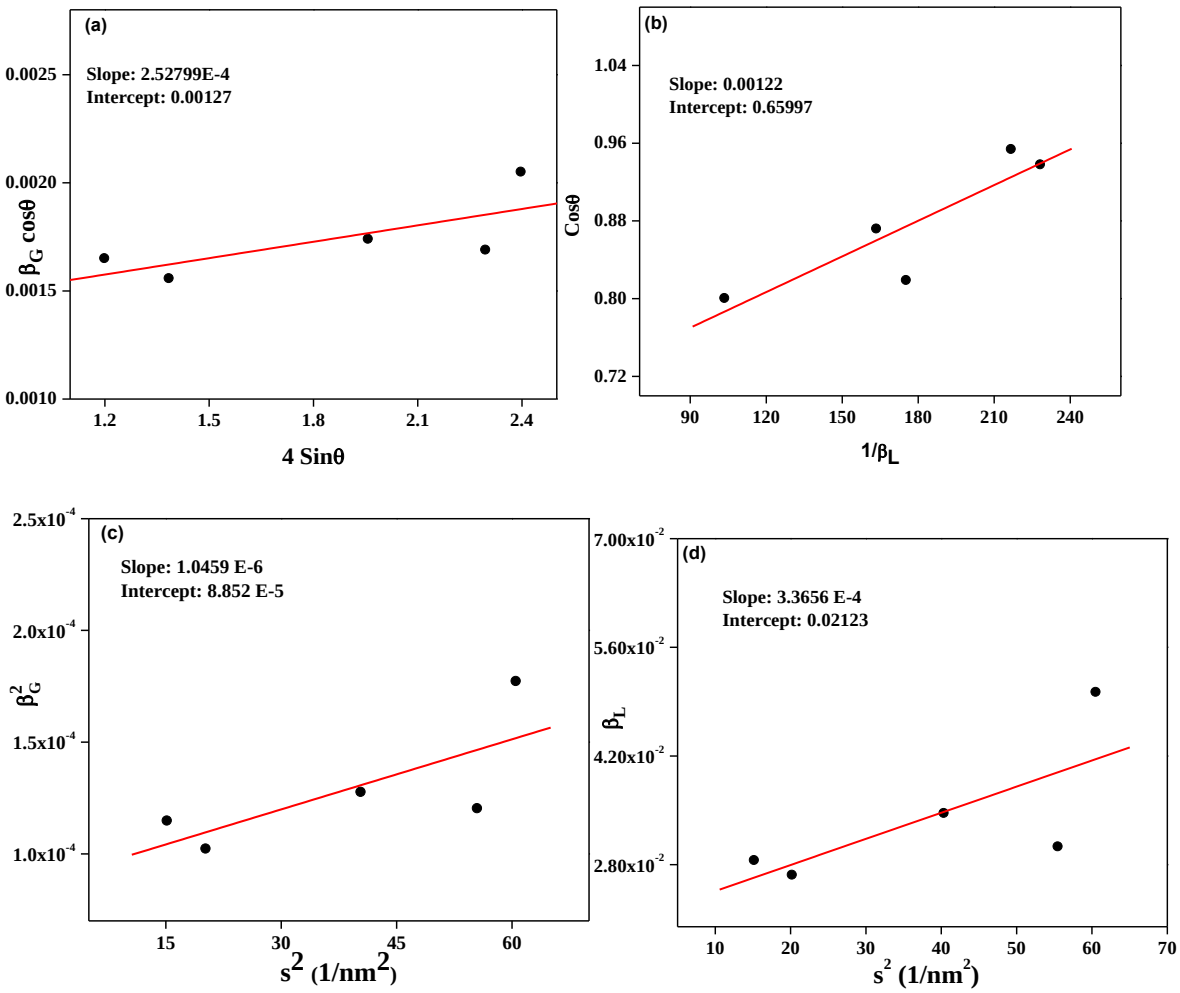

Figure 4.4: Single line integral breadth analysis graphs of E10h8 sample. Determination of: (a) maximum strain and (b) particle size. Double-Voigt Integral breadth analysis graphs ((c) and (d)) of E10h8 sample.

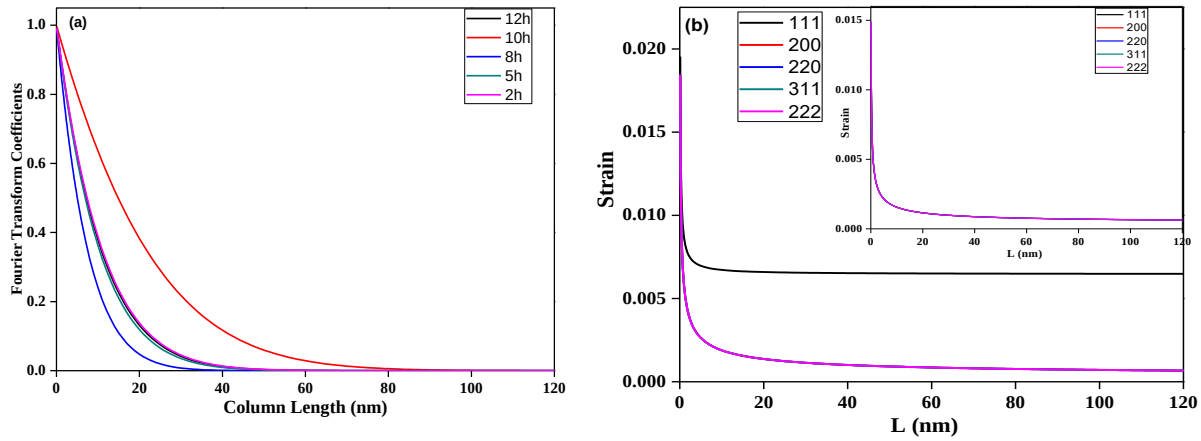

Figure 4.5: (a) Fourier transform coefficients as a function of column length (L) for all the synthesized samples. The initial slope of this graph is used to determine the surface weighted particle size. (b) Strain as function of column length (L) for all the indexed planes for the E10h8 sample. Inset shows isotropic nature of the strain in E08h8 sample.

The results of XRD data analysis show that both E08h8 and E10h8 samples are good prospective candidates for the electro-catalytic activities; the 10h sample due to its enhanced strain which makes it more reactive and the 8h sample due to its larger surface area which provides more reaction sites. The electrochemical activity of both the samples will need to be probed to assess the comparative importance of strain and surface area for the catalytic activities.

4.4 Thermal analysis

DSC/TG has been used to analyse the thermal stability and oxidation resistance of the synthesized powders. Figure 4.6 (a) shows the representative DSC-TG-DTG curves for all the synthesized samples except the E10h8 sample where the distinct decarburization and oxidation events are observed (Figure 4.6 (b)). The data obtained from analysis of the DSC-TG-DTG curves is given in Table 4.4.

For all the samples from room temperature onwards initial heating results in mass loss followed by mass gain. This initial mass loss is indicative of the amount of chemical species adsorbed onto the surface of the particles [2]. For these samples before start of the oxidation nearly 2 mass% of surface adsorbed species is removed. This corresponds to potentially large surface area available for adsorption. The start of mass gain in TG curve is an indicator of the stability of the synthesized samples as the weight gain in the samples is due to oxidation of TaC resulting in formation of Ta_2O_5 and CO_2 [3].

For the E10h8 sample the peaks for carbon removal and oxidation are well separated. The E02h8 and E05h8 samples have nearly the same oxidation stability (Table 4.4) but as the soaking time is increased the samples are becoming more stable. The E10h8 sample is most stable for oxidation in air with the weight gain in TG starting at around 339 °C (Figure 4.6 b)). The E12h8 sample shows the expected decrease in stability due to carbon deficient TaC.

The first peak in DTG with a corresponding exothermic peak in DSC and maximum mass gain in TG gives the temperature for the conversion of TaC into Ta_2O_5. This conversion is a two-step process: release of carbon from the TaC followed by oxidation. For the TaC_x ($x<1$) samples the two processes occur simultaneously as there are already carbon vacancies present in the system. But for the case where $x = 1$ (10 h sample) the oxidation occurs after the removal of carbon and the DSC as well as DTG curve show well defined peaks for the two processes: the carbon removal occurring at 573 °C followed by oxidation at 598 °C (Figure

4.6(b)). The ΔH values represent the amount of heat required for a reaction and were determined from the total area enclosed by the thermal analysis peak using the software package provided with the thermal analyzer. The ΔH for the two processes is 25.73 J/g and 21.2 J/g respectively. The high temperature peak (>700 °C) in DTG curve, with a corresponding peak/hump in DSC, occurs at nearly the same temperature for all the samples and is attributed to oxidation and combustion of the carbonaceous residue [4].

Table 4.4: The data obtained from the analysis of the DSC-TGA-DTG curves and BET analysis of the synthesized samples.

Sample Name	**Weight gain start (°C)**	**DSC main peak (°C)**	**DTG peak 1 (°C)**	**DTG peak 2 (°C)**	**Average Pore diameter (nm)**	**Surface Area (m^2/g)**	**Pore Volume (cm^3/g)**
E02h8	167	578	584	715	12.244	74.909	0.2293
E05h8	162	595	604	710	12.404	95.383	0.2958
E08h8	183	586	590.5	716	9.1541	159.67	0.3654
E10h8	339	573 598	576 601	720	14.023	44.851	0.1572
E12h8	206	580.4	581	721	14.199	56.113	0.1992

Oxidation of pure TaC results in 14.5% increase in mass. In present case this is never achieved. Maximum increase encountered is nearly 4.5 mass% after the initial weight loss stops for the E08h800 sample. This small increase in mass as compared with the expected value is due to the presence of carbonaceous content in the synthesized samples [3]. The presence of carbonaceous residue is indicated/supported by XRD data as well as TEM images. As the sample is heated the mass increase due to oxidation is being offset by the decrease in mass due to oxidation of carbonaceous residue. The residual mass at 800 °C for all the samples is 85-90%. This leads to the conclusion that the carbonaceous content in the samples ranges from 20-25 % [5]. All the TGA curves become nearly stable after 780 - 795 °C. Even heating up to 1200 °C further shows a loss of 1% indicating that carbonaceous substance is not removed completely (data not shown). So the determination of exact TaC content in the individual samples is not possible.

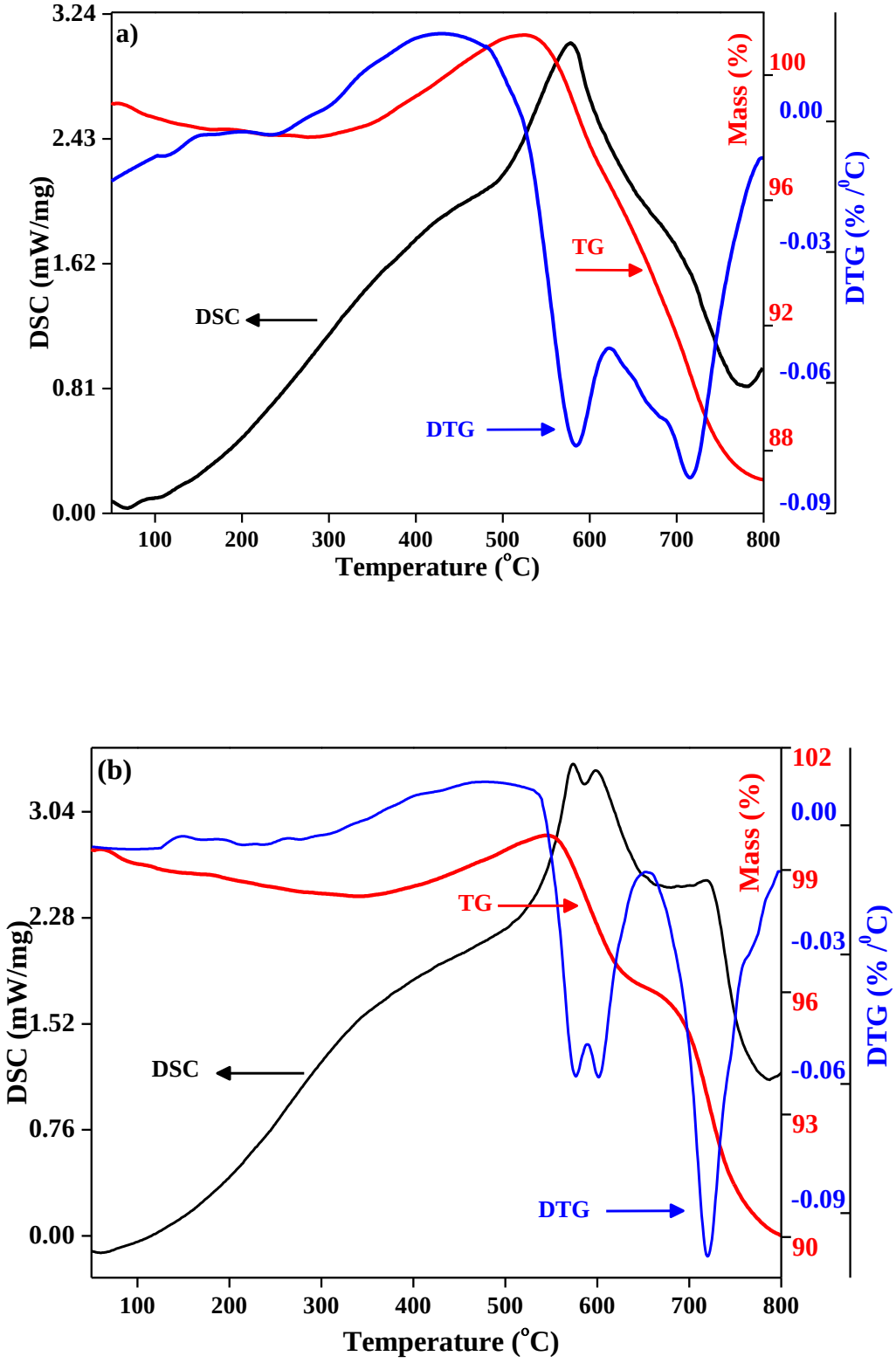

Figure 4.6: DSC-TG-DTG curves of sample (a) E02h8 (b) E10h8.

4.5 Microstructure analysis

Figure 4.7 shows the representative FE-SEM image of the final product synthesized for E10h8 sample. It is clear from the images that particles have inhomogeneous size distribution and a tendency to agglomerate. The analysis of the morphology of particles shows that most of the powders are faceted and their size varies from 60-100 nm.

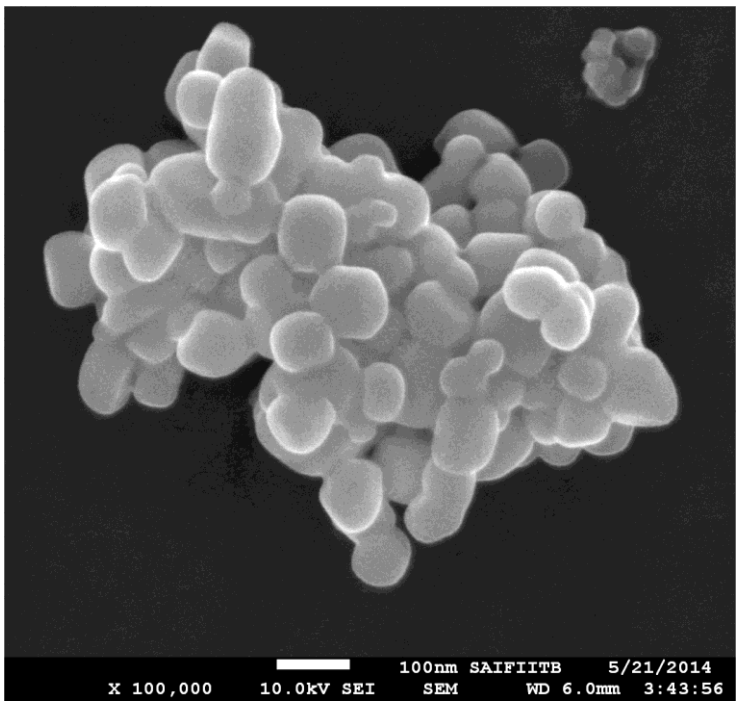

Figure 4.7: FE-SEM micrograph of TaC nanopowder for E10h8 sample showing faceted to spherical morphology.

Figure 4.8 (a-b) shows the representative TEM images of the synthesized TaC nanoparticles for E10h8 sample. The presence of carbon coating on the surface of each particle is clearly visible. Moreover, the morphology of carbon coated nanoparticles varies from faceted to spherical and they have a tendency to aggregate. Figure 4.8(c) gives the High Resolution-TEM (HRTEM) image of a single crystalline TaC nanoparticle and shows the (111) facets of the particle. The distance between the adjacent lattice fringes is the interplanar distance of cubic TaC (111), which is 0.26 nm (ICDD Pattern – 01-089-2870). This suggests that the synthesized TaC powder has cubic crystalline structure.

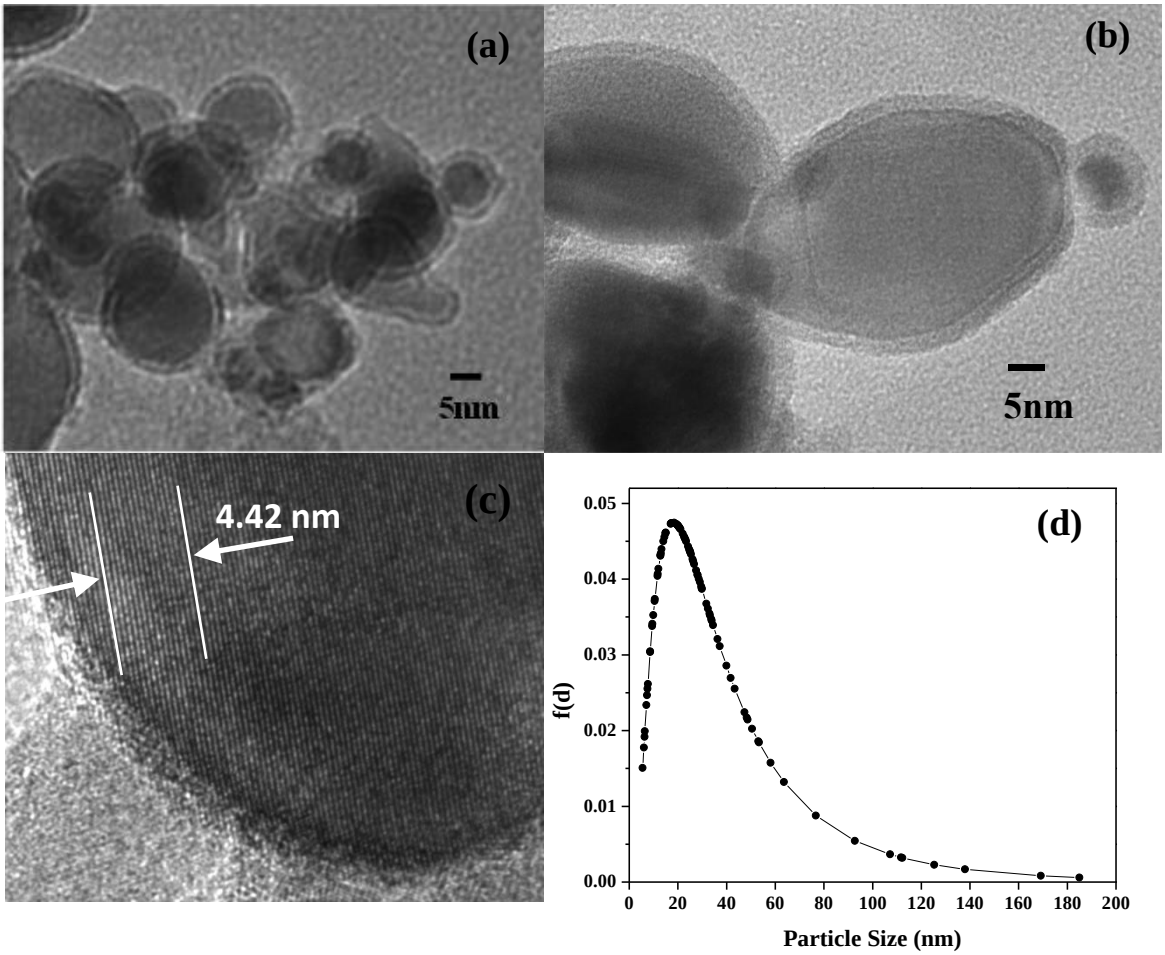

Figure 4.8: TEM morphology analysis for the E10h8 sample. (a-b) TEM micrographs of TaC nanopowder. The agglomerated particles have nearly spherical morphology and are evenly coated with a carbon layer. (c) HRTEM micrograph of TaC nanopowder showing lattice fringing. (d) Particle size distribution from TEM.

It is observed from TEM images that the particle size distribution is broad (Figure 4.8(d)). The particle size measurement was done on nearly 100 particles from different areas/scans and follows the well documented log-normal distribution [6]. The log-normal probability distribution (Figure 4.8(d)) is calculated by adopting the following equations:

$$f(d) = \frac{1}{\sqrt{2\pi}\, d\, log\sigma_g} \exp\left\{-\frac{(log\, d - log\, \mu_g)^2}{2(log\, \sigma_g)^2}\right\} \tag{4.2}$$

$$\log \sigma_g = \sqrt{\frac{\Sigma(logd_i - log\mu_g)^2}{\Sigma n_i}} \tag{4.3}$$

$$log\mu_g = \frac{\Sigma log d_i}{\Sigma n_i} \quad (4.4)$$

Where f(d) denotes the log-normal distribution, d the particle diameter, n_i the number of particles with diameter d_i, log μ_g the mean diameter and σ_g is the geometrical standard deviation, respectively. The average size of the prepared TaC nanoparticles is in the range of 20 to 40 nm for the reaction time of 10 h. The size obtained from the TEM is comparable to that obtained from the double-Voigt integral breadth analysis.

4.6 BET surface area analysis

The results of BET surface area obtained from the N_2 sorption studies of the synthesized powders are listed in Table 4.4. The data shows that initially the surface area of the product increased with increasing soaking time with maximum area of 159.67 m^2/g obtained for the 8h sample. A further increase in time results in decrease in the surface area. This is most likely due to increase in particle size for the E10h8 sample as is evident from the XRD analysis.

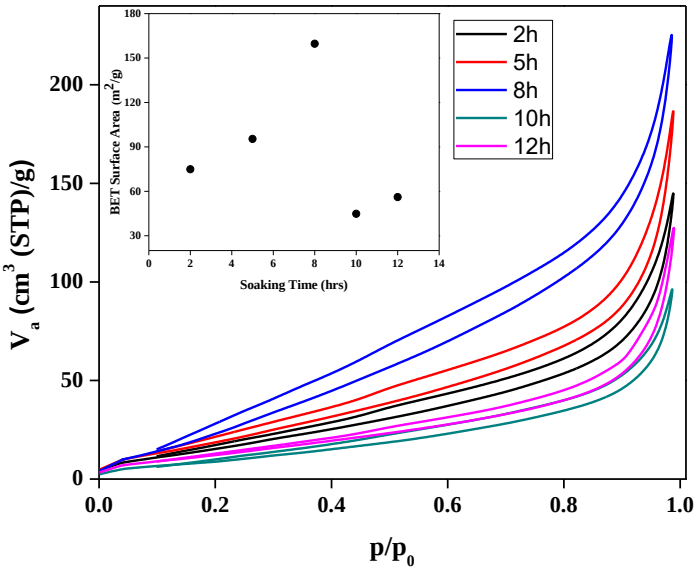

Figure 4.9: N_2 adsorption-desorption isotherms for the synthesized samples. Inset shows the variation of BET surface area for the synthesized samples with increasing soaking time.

Figure 4.9 shows the N_2 adsorption-desorption isotherms for the synthesized samples. The adsorption isotherms exhibit the characteristics of a type-II isotherm according to IUPAC classification [7,8]. As per the empirical classification of the hysteresis loops the isotherms for the samples show H-4 hysteresis characteristics [8,9]. This implies that due to the

agglomeration of particles in the synthesized product the powders are forming a complex structure with both micropores and mesopores.

4.7 Synthesis mechanism

During heating of the autoclave, Mg being highly reactive substance absorbs oxygen from the air present inside the autoclave and forms MgO. In conjunction with low temperature heating experiments (500 °C, 2 hrs, Figure 4.10) and earlier reported data about decomposition of Ta-E [10], the Ta-E decomposes initially into tetrahedral TaO (ICDD card no – 00-17-0709).

$$Ta_2(OC_2H_5)_{10} \rightarrow TaO + Gaseous\ Organic\ Intermediates \qquad (4.5)$$

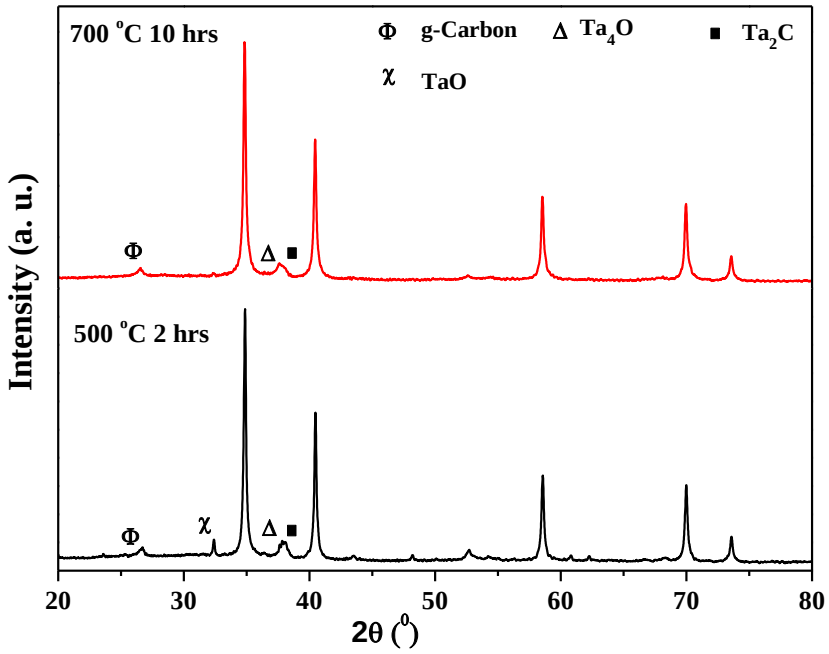

Figure 4.10: XRD data for E10h7 and E02h5 samples.

The decomposition of Ta-E is taking place in a closed oxygen deficient environment so the exact nature of the gaseous organic intermediate(s) cannot be determined. Since, MgO is one of the most active catalysts for reduction [11], so its presence results in reduction of the gaseous organic compounds to hydrogen and carbon.

The carbon is present in excess in Ta-E and is enough to completely coat the initially formed TaO powder. This carbon coating ensures the close proximity of the reactants and helps to increase the reaction rate for reduction and carburization. Moreover, the carbon coating also prevents the oxide particles from coalescing which ensures that the final product is in nanometer range [1]. The initially formed TaO transforms to TaC via formation of Ta_4O and Ta_2C (Figure 4.2, 4.10). In the entire set of experiments no evidence of Ta was found in any of the samples, rather Ta_2C was present. Since the carbon is present in sufficiently high concentration so it is possible that Ta obtained from reduced oxide may get converted into Ta_2C immediately and then to TaC. Figure 4.11 gives the schematic of the proposed mechanism. In the present system the formation of TaC starts with the reduction of TaO rather than Ta_2O_5 so this leads to lowering of reaction/formation temperature and time.

Reaction rate within the autoclave is also very high as is evident from the nearly 80-90 % conversion within 2 h for all the temperatures. However, the complete conversion needs 10 h at 800 ^{0}C (Figure 4.2 and 4.10). The higher time required for complete conversion is because of the fact that in the initial stage diffusion of carbon through the surface leads to formation of TaC on the outer surface of the particle and this formed TaC layer creates hindrance for further diffusion of carbon inside. The large concentration of carbon in the outer coating still facilitates the diffusion of carbon into inner unreacted core even through the TaC. However, the carbon atoms now need to travel longer distance which makes the final process time dependent as the diffusion path of carbon increases with time as the reaction progresses. In order to facilitate the entire process the travel rate of carbon can be made faster by increasing the holding temperature as is evident from Figure 4.10 where complete conversion is not taking place at 700 ^{0}C in the same time duration (10 h) as has been obtained at 800 ^{0}C (Figure 4.2).

The thermodynamic calculations have not been undertaken to check the proposed formation mechanism since the data for Ta_4O and Ta-E is not available.

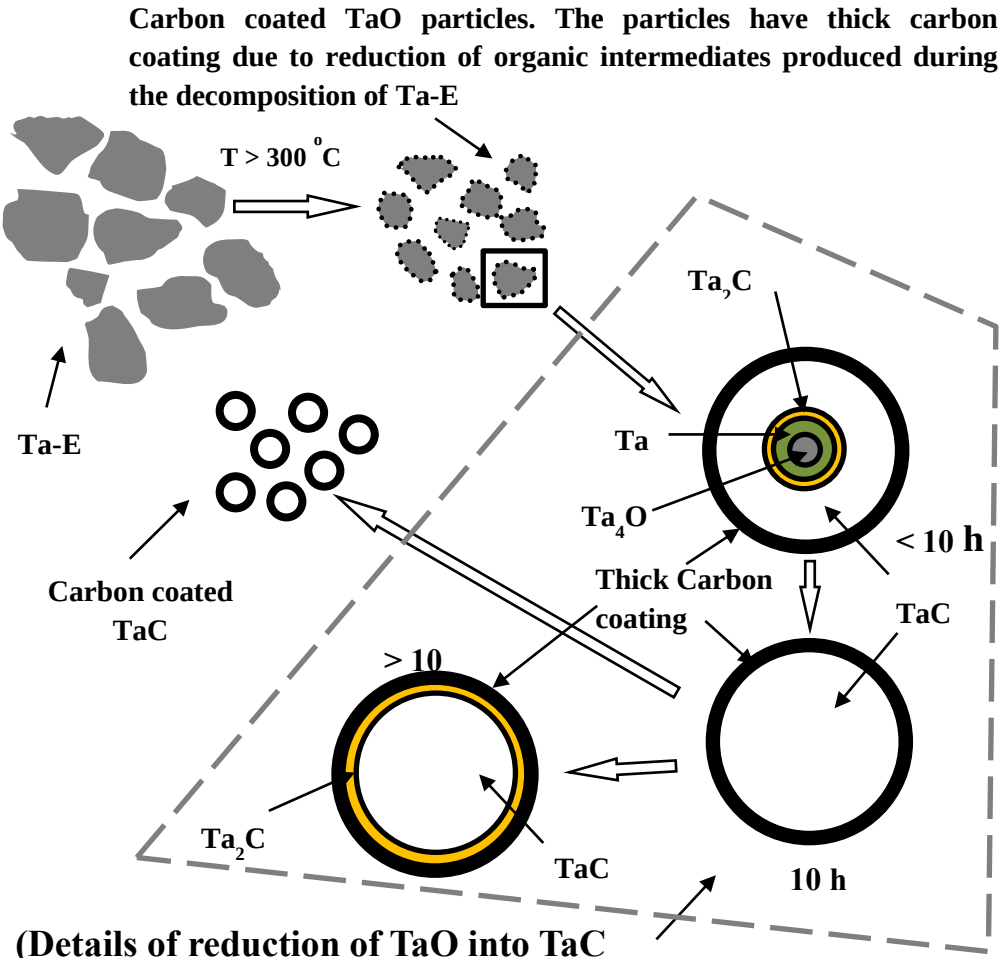

Figure 4.11: The proposed mechanism for transformation of Ta-E into carbon coated TaC nanoparticles.

References:

[1]. C. Huang, T.-E.Hsieh, *J. Appl. Polym. Sci*., **117** (2010) 1252–1259.

[2]. J.P. Kelly, O.A. Graeve, *J. Am. Ceram. Soc.*, **94** (2011) 1706–1715.

[3]. N.S. Alhajri, H. Yoshida, D.H. Anjum, A.T. Garcia-Esparza, J. Kubota, K. Domend, K. Takanabe, *J. Mater. Chem., A* **1** (2013) 12606-12616.

[4]. D.-H. Kwon, S.-H. Hong, B.-K. Kim, *Mater. Chem. Phys.* **93** (2005) 1–5.

[5]. A. L. Tomas-Garcia, Q. Li, J. O. Jensen, N. J. Bjerrum, *Int. J. Electrochem. Sci.* **9** (2014) 1016-1032.

[6]. B. Debalina, M. Kamaraj, S.R. Chakravarthi, N.J. Vasa, R. Sarathi, *Plasma Sci. Technol.* **15** (2013) 562-69.

[7]. Y.-J. Lee, S.H. Kima, T.-H. Lee, H.H. Nersisyanb, K.-H. Lee, M.-H. Hana, S.-U. Jeong, K.-S. Kang, K.-K. Bae, J.-H. Lee, *Chem. Eng. Sci.* **107** (2014) 227–234.

[8]. W. Wang, P. Liu, M. Zhang, J. Hu, F. Xing, *Open J. Compos. Mater.* **2** (2012) 104-112.

[9]. M. Thommes *Chem. Ing. Tech.* **82** (2010) 59-73.

[10]. H. He, K. Zhou, X. Xiong, B. Huang, *Mater. Lett.* **60** (2006)3409–3412.

[11]. V.K. Díez, C. R. Apesteguía, J.I. Di Cosim, *Lat. Am. Appl. Res.* **33** (2003)79–86.

CHAPTER 5

Nano-TaC from Tantalum (V) Oxide

Overview

This chapter presents the results obtained from the synthesis and characterization of the nano TaC obtained from Tantalum (V) oxide (Ta_2O_5) using acetone as a carbon source and Mg as catalyst. The XRD results of all the synthesized samples have been analysed and discussed. The size, strain and the lattice carbon content (***x***) of the TaC_x nanopowders has been used to determine the evolution of the powders with time as well as initial carbon (C) concentration. Based on XRD results and thermodynamics parameters, the formation mechanism of the nano TaC has been proposed. Also, the importance of Mg as a catalyst in lowering the synthesis temperature has been discussed. From the thermal analysis results, the stability of the synthesized powders over a range of temperature(s) as well as the external carbon content of the powders has been evaluated. FE-SEM and HRTEM results have been presented and discussed to analyse the microstructure of the synthesized powders and to confirm the crystal structure of product phase by measuring the lattice fringing. Surface area and pore size distribution of the synthesized samples has been analysed by BET technique.

5.1 Optimization of magnesium molar ratio

The Ta:Mg molar ratio is very important in lowering of the synthesis temperature of TaC. The ratio of Mg was varied as: 9, 11, 12, 22. For x = 9, 11 the pure phase TaC is not obtained even for initial C = 90, at 800 °C in 10 hrs (Figure 5.1). For Mg = 12 and 22 there was formation of pure phase TaC (Figure 5.1). The current series of experiments were performed for Mg ratio 12 as higher catalyst stoichiometry leads to larger agglomeration [1].

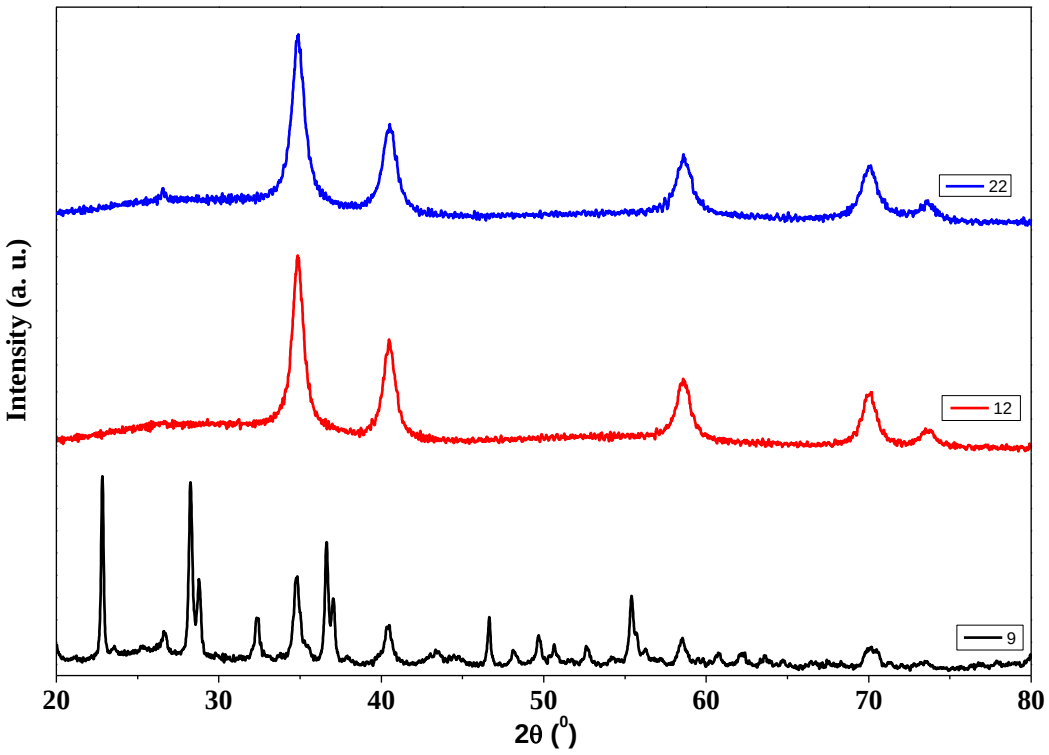

Figure 5.1: XRD results of the samples synthesized from Ta_2O_5 with different molar ratio of magnesium.

5. 2 Samples

The experiments for TaC formation were planned with Mg molar ratio = 12. The other parameters: initial carbon concentration, holding temperature and holding time, were varied to obtain single phase powders as well as to study the evolution of powders. All the single phase samples obtained using Ta_2O_5 and their synthesis parameters are listed in Table 5.1.

Table 5.1: Single phase samples synthesized using Ta_2O_5. (Magnesium molar ratio is 12 for all the samples)

Sample Name	Initial Carbon Conc. (Molar Ratio)	Time (h)	Temperature (°C)
Ox01C	1	2	800
Ox02C	2	2	800
Ox03C	3	2	800
Ox05p5C	5.5	2	800
Ox07p5C	7.5	2	800
Ox15C	15	2	800
Ox40C	40	2	800
Ox60C	60	2	800
Ox90C	90	2	800
Ox01Q	3	1	800
Ox01T	3	1	800
Ox02T	3	2	800
Ox07T	3	7	800
Ox10T	3	10	800
Ox15T	3	15	800

5.3 X-ray diffraction analysis (XRD) of the synthesized product

The XRD data for the initial Ta_2O_5 powder and the synthesized samples for the initial Ta:C molar ratio of 1:1 at various temperatures (soaking time 1 h) is shown in Figure 5.2. XRD data clearly shows that though the material remains Ta_2O_5 till 650 °C its particle size reduced as indicated by the broadened XRD peaks. This is followed by formation of pure cubic phase Ta (ICDD - pattern 00-004-0788) at 700 °C. The Ta particles formed at 700 °C are small in size as well as highly strained as evidenced by the broad XRD peaks shifted towards lower angles as compared to standard reference [2]. At 750 °C TaC (ICDD Pattern – 01-077-0205) and Ta_2C (ICDD – pattern 00-032-1280) coexist. The XRD data clearly shows that the pure phase cubic TaC is formed only at 800 °C. Based on these results and the thermal calculations the formation mechanism for TaC has been proposed (discussed in section 5.7).

The final soaking temperature of 800 °C was thus chosen for further studies: **a)** effects of changing initial carbon (C) concentration (molar ratio: 1 to 90) (Figure 5.3 Table 5.2) and **b)** evolution of TaC with soaking time (1 h to 15 h) (Figure 5.4, Table 5.3).

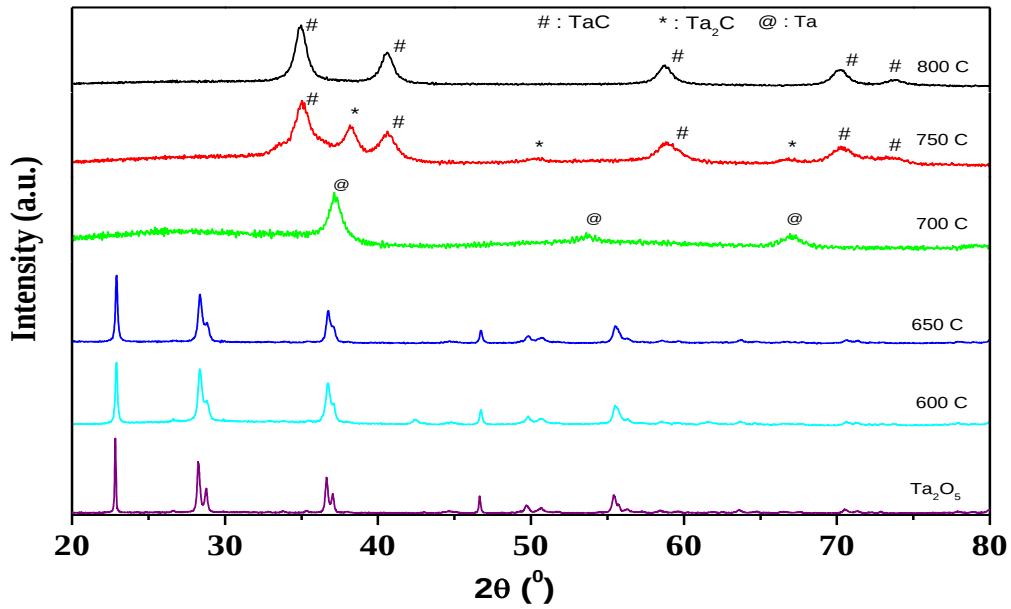

Figure 5.2: XRD results of the Ta_2O_5 powder and the acid leached samples synthesized from it with different soaking temperatures.

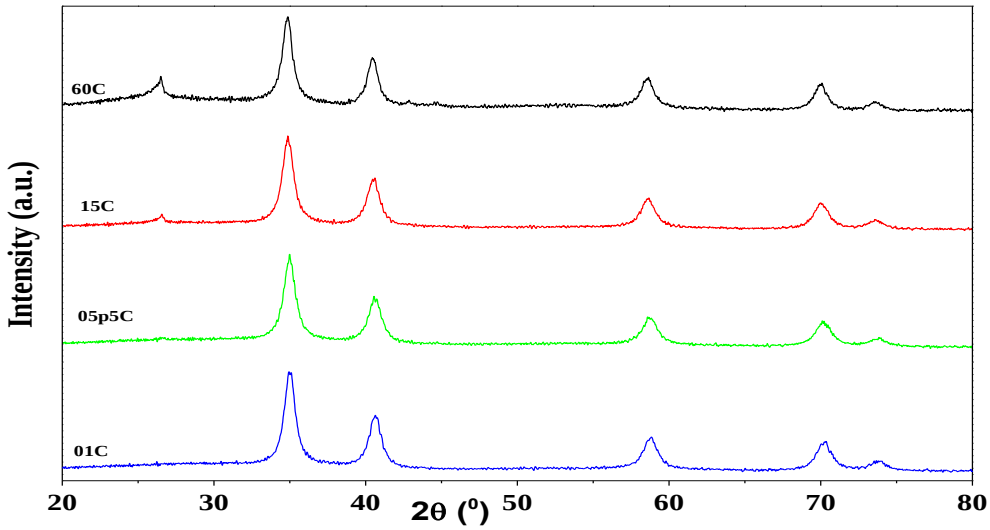

Figure 5.3: Selected XRD results of the TaC powders obtained for different initial carbon concentrations. (Only selected data have been plotted to ensure clear visibility of the increasing graphite peak).

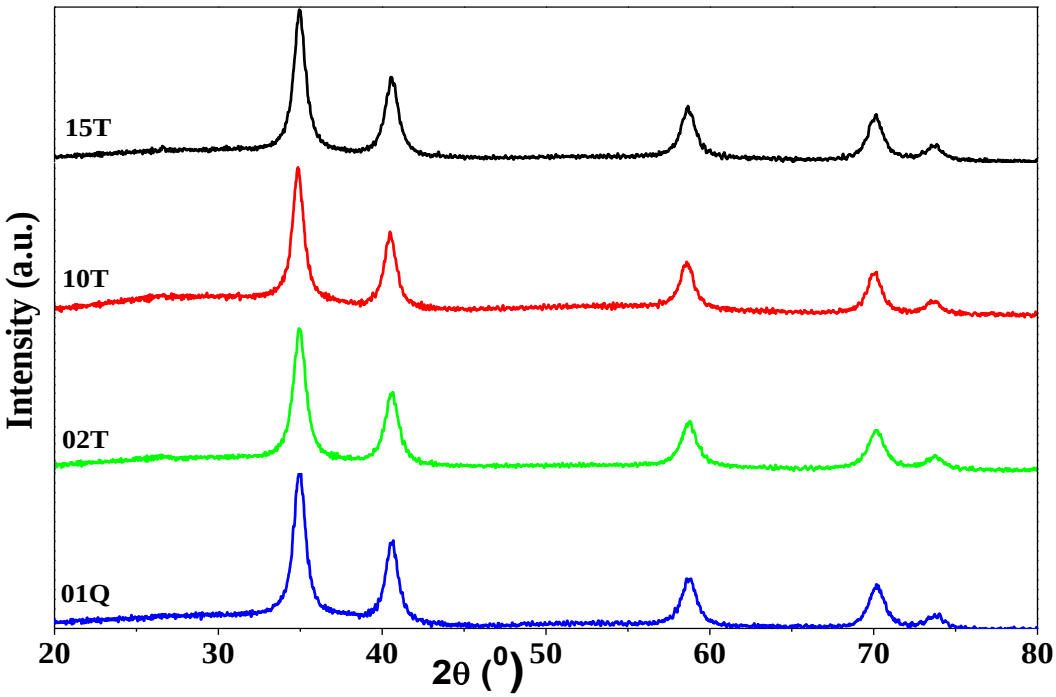

Figure 5.4: Selected XRD results of the TaC powders obtained for different soaking times.

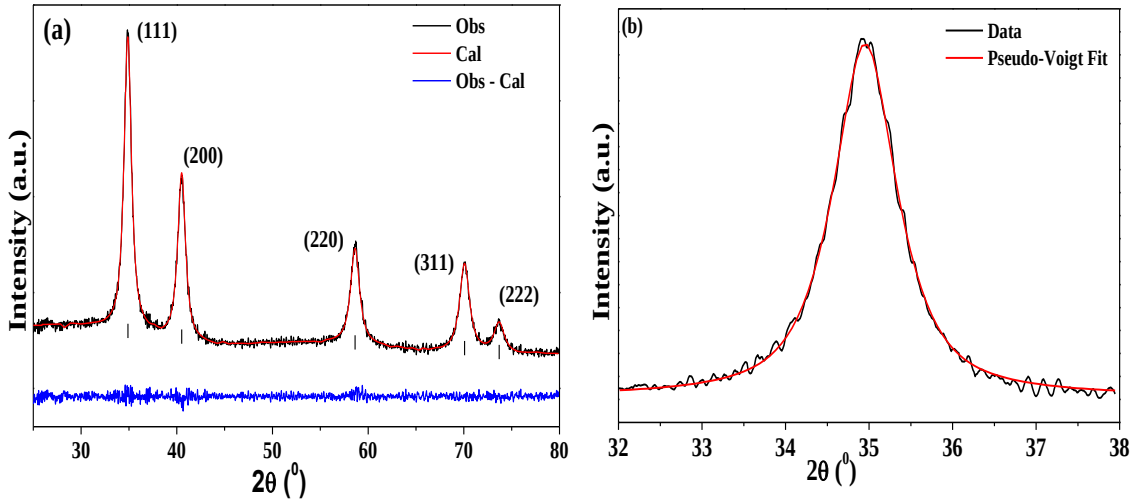

Figure 5.5: (a) Rietveld refinement plots for the Ox03C sample. Tick marks indicate allowed peak positions. (b) The result of the pseudo-Voigt curve fit routine for the (111) peak of Ox03C sample.

Table 5.2: Effect of initial Carbon (C) concentration (The soaking temperature for all the samples is 800 °C with 2 h soaking time, D_v and D_s are the volume weighted and surface weighted sizes obtained from the double-voigt analysis).

Sample Name	χ^2	R_{wp}	*a* (nm)	*x*	D_V (nm)	D_S (nm)	RMSS (x 10^{-3}) at 5 nm
Ox01C	0.510	4.20	0.44508	0.96	6.6	4.06	1
Ox02C	0.540	3.96	0.44498	0.95	6.8	4.1	2.19
Ox03C	0.565	4.09	0.44497	0.95	6.3	3.8	3.14
Ox05p5C	0.577	4.43	0.44496	0.95	7.1	4.1	5.31
Ox07p5C	0.744	4.75	0.44551	0.98	6.9	4.0	3.21
Ox15C	0.945	5.51	0.44555	0.99	6.2	3.8	4.34
Ox40C	1.55	7.10	0.44532	0.98	7.3	4.2	4.21
Ox60C	1.31	6.40	0.44534	0.98	6.6	4.0	4.37
Ox90C	1.46	6.88	0.44534	0.98	7.5	4.6	4.31

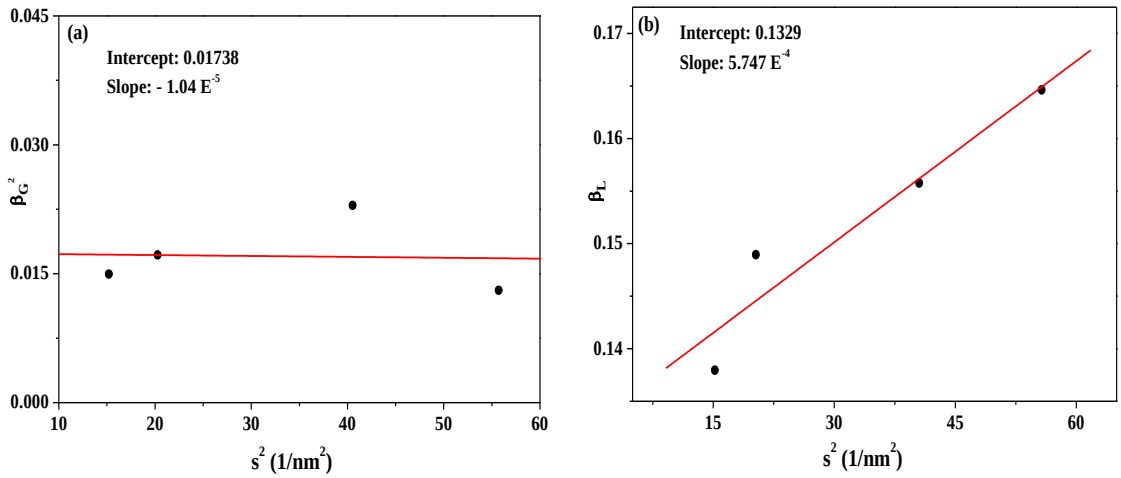

Figure 5.6: Double-Voigt Integral breadth analysis graphs ((a) and (b)) of Ox03C sample.

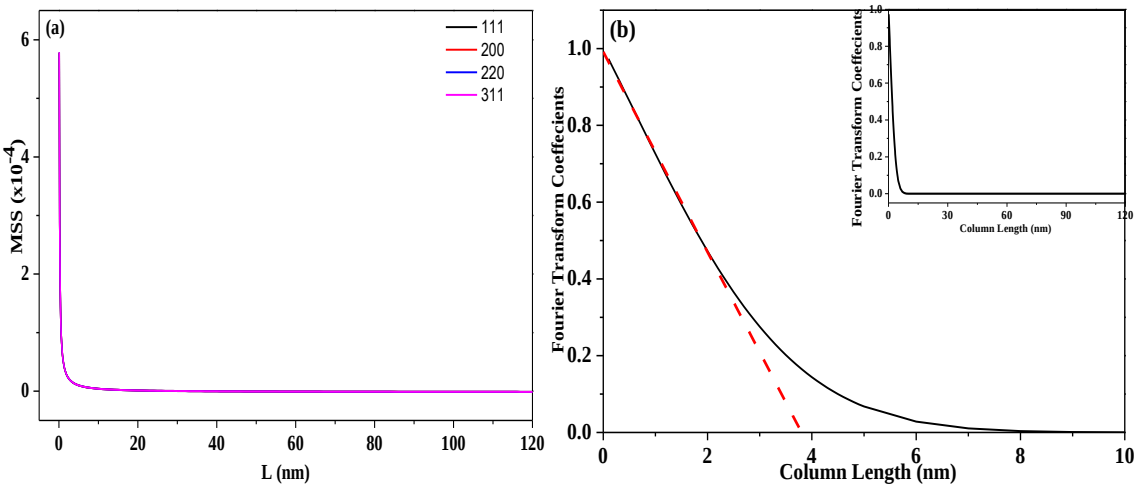

Figure 5.7: (a) Mean Square Strain (MSS) as function of column length (L) for all the indexed planes for the Ox03C sample showing the isotropic nature of the strain. (b) The initial slope of the Fourier transform graph is used to determine the surface weighted particle size. Inset shows the variation of Fourier transform coefficients with column length (L) for the Ox02T sample.

Figure 5.5 (a) gives the Rietveld refinement plots for the Ox03C sample. Figure 5.5 (b) shows the results obtained from the fitting of (111) peak with the pseudo-Voigt function for the Ox03C sample. The lattice parameter (***a***), R_{WP} and χ^2 – values obtained from the Rietveld refinement are listed in the Tables 5.2 and 5.3. Figure 5.6 gives the D-V integral breadth method analysis graphs for the Ox03C sample. Similar graphs have been used to analyse all the samples. Figure 5.7 shows the isotropic nature of the strain and variation of Fourier transform coefficients as a function of column length for Ox03C sample.

a) Effects of changing initial carbon (C) concentration: Increasing the initial C molar concentration (from 1 to 90) resulted in a slight change in the particle size (Figure 5.8 (a)). This variation lies within the error limits of the XRD analysis. More interesting picture about the role of initial C concentration emerges from the study of the variation of ***a*** (and hence the carbon within the carbide phase) and RMSS (Figure 5.8 (b)).

For the lower initial C concentration ($\leq$ 5.5) an increase in the C concentration results in a slight decrease in ***a*** and many fold increase in the strain. It is due to an increase in the thickness of the graphitic carbon outside the carbide phase which hindered the concentration induced diffusion of carbon into the particles. XRD data (Figure 5.3) clearly shows that with the increasing initial C concentration the graphitic carbon peak at $2\theta \sim 26$ ° slowly becomes more prominent. This result is also supported by the TG/DSC, SEM and TEM data (discussed

in following sections). Increase in initial C concentration beyond 5.5 results is sudden increase in the value of ***a*** and a corresponding decrease in RMSS. This indicates that now the concentration gradient in the system is sufficient enough to overcome the hindrance to diffusion from the graphitic layer and results in increased carbon within the carbide phase and lower strain. Further increase in the initial C results in saturation of ***a*** and RMSS to a constant value (Figure 5.8(b)). The final saturation value of ***a*** is slightly lower than the maximum value since the graphitic carbon layer is increasing many-fold on the outside of the particles. The existence of critical initial stoichiometry and its effect on the final powder properties has been discussed in literature earlier also for other synthesis methods [1].

Thus the diffusion of carbon into the particle and hence the final carbon content in the lattice of TaC is a complex function of initial C concentration since an increase in carbon concentration creates a diffusion enhancing gradient but at the same time the extra carbon forms graphitic carbon network outside the particles which hinders the diffusion of carbon into the particle.

b) ***Evolution of TaC with soaking time:*** For Ox01Q sample (sample is quench cooled outside the furnace after 1 h soaking) XRD pattern analysis shows the presence of single phase cubic TaC_x with $\boldsymbol{x}$ = 0.92. This means that at 800 °C the formation TaC, which is essentially a multistep reduction and carburization process, is very fast. This happens due to fast diffusion rate of C as well as the free energy considerations (the steps and the energy considerations are discussed in the subsequent section). So the carbon, which diffuses into the crystallites and reacts for the formation of TaC, either may not get sufficient time for diffusion or if diffused might not be in optimum locations. This is evidenced by the high strain in the samples.

Even the slow cooling of the system (Ox01T sample) allows only for more carbon to diffuse into the crystallites such that the particle volume weighted size as well as the strain increases. It is finally for the 2 h soaking time followed by slow cooling that the system attains a lower strain as well as the smaller crystallite size in spite of further increase in the lattice carbon content. The decrease in the crystallite size and strain is observed because the higher soaking time allows for the carbon within the TaC to finally achieve its best possible configuration. As the soaking time is further increased the diffusion of carbon into the crystallites continues.

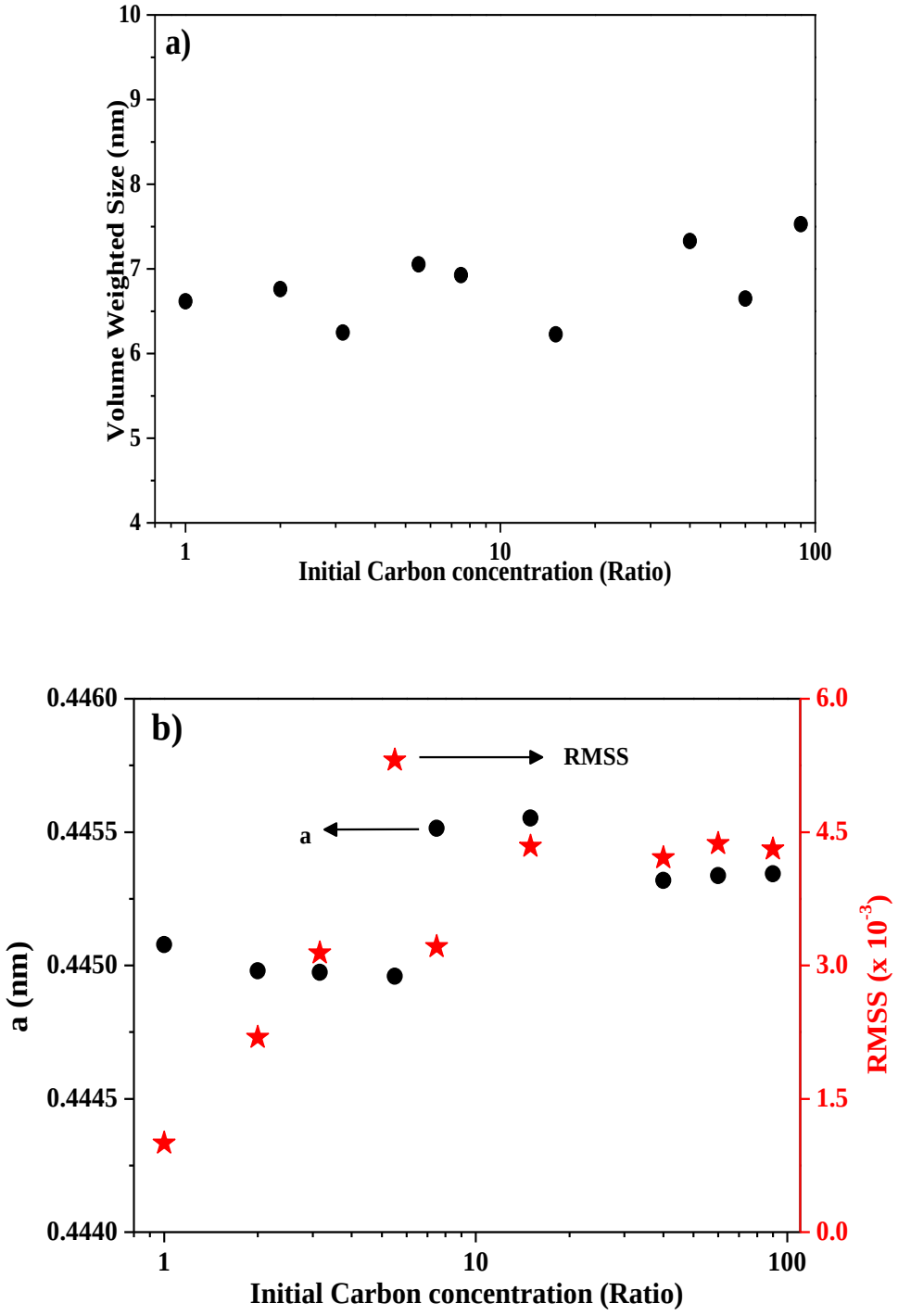

Figure 5.8: a) Particle size variation with the initial carbon concentration. b) Lattice constant variation with the initial carbon concentration. The x- axis (carbon concentration) is plotted on logarithmic scale for clarity of data at lower concentration.

A closer look at the time evolution of the size and strain data (Table 5.3) shows that the crystallites in turn are becoming smaller in size and strained followed by the larger size and lower strain. This is a clear indication that once the carbon inside the TaC crystallites have achieved the lowest energy configuration the further heating results in grain growth which seems to follow the simultaneous grain rotation and grain boundary (GB) migration model [3-5]. In this mechanism initially the grain boundaries grow/migrate resulting in decreased grain size and increased strain in the system. This is followed by the grain rotation across the lowest angle grain boundary resulting in larger grain as the GB between them vanishes. At the time of the grain shrinkage the GB becomes vastly enhanced so the samples show higher average strain and smaller grain size. An important consequence of this type of grain growth for TaC is that the manifold increase in strain just before rotation also results in expulsion of some of the carbon from the crystallites. So for these samples the lattice carbon content of the carbide phase also alternates with soaking time and grain growth.

In the present system the evolution of the TaC nanopowder with increasing soaking time at 800 °C can essentially be divided into two regimes: ***(i)*** the formation of low strain TaC followed by ***(ii)*** grain growth via simultaneous grain rotation and GB movement mechanism. Figure 5.8 show the proposed grain evolution mechanisms for TaC.

The surface weighted size for all the samples is smaller than the volume weighted size but follows the same trend as the volume weighted size for the time and carbon variation. This is believed to be an indicator for the temperature and time scales used in present setup the grains do not have anisotropic growth [6].

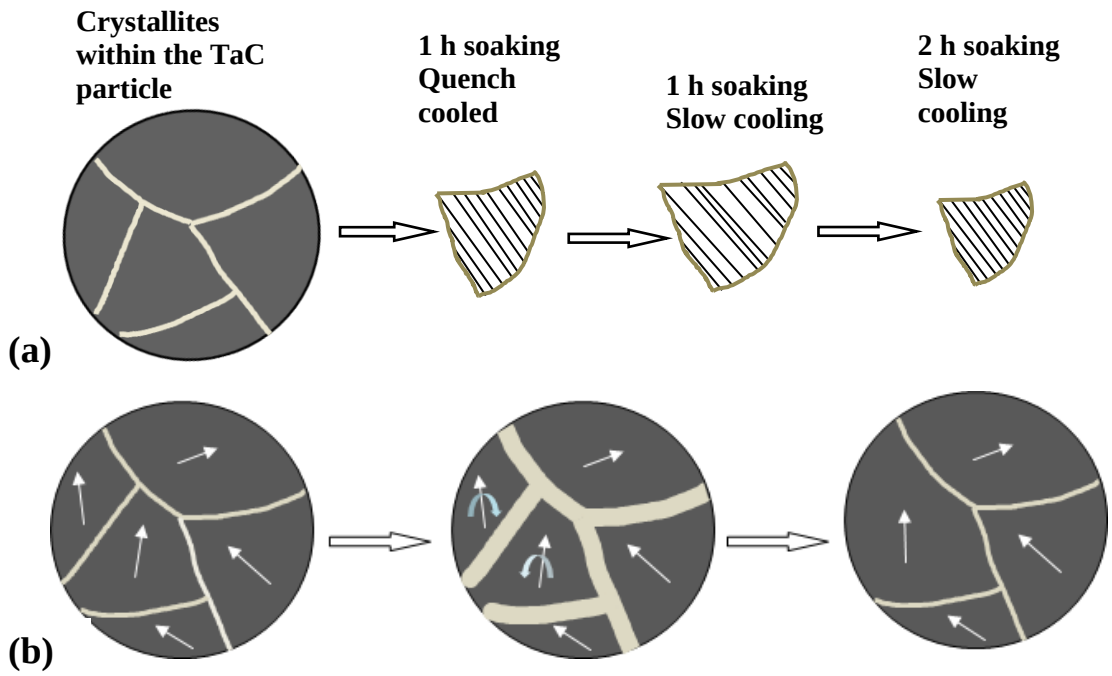

Figure 5.9: a) Initial growth mechanism leading to low strain samples of TaC. (The unequal distance between the planes inside the crystallite represents the presence of strain) b) Simultaneous GB migration/Grain rotation mechanism of grain growth mechanism for the low strain crystallites. (The arrow inside the crystallite represents the orientation)

Table 5.3: Evolution of TaC with soaking time (The soaking temperature for all the samples is 800 ^{0}C and initial carbon concentration is 3).

Sample Name	χ^2	R_{wp}	*a* (nm)	*x*	D_V (nm)	D_S (nm)	RMSS (x 10^{-3}) at 5 nm
Ox01Q	0.571	4.13	0.44445	0.92	6.5	4.1	6.22
Ox01T	0.575	4.12	0.44458	0.93	9.2	5.2	7.39
Ox02T	0.565	4.09	0.44497	0.95	6.3	3.8	3.14
Ox07T	0.534	4.03	0.44547	0.99	5.1	2.6	14.45
Ox10T	0.538	4.06	0.44485	0.95	7.4	4.4	1.34
Ox15T	0.542	4.26	0.44551	0.99	6.2	3.8	4.074

5.4 Thermal analysis

The thermal stability and oxidation resistance of the synthesized powders were analyzed by DSC/TG. The DSC-TG curves for the Ox01C sample (Figure 5.10) is representative for all the synthesized samples. The main observations from the data are: Initial heating results in mass loss followed by gain in mass. This initial mass loss is signature of the adsorbed species on the surface of the particles and hence gives information about the surface area of the powder samples [1]. For the present samples before oxidation nearly 3 mass% of surface adsorbed species is removed. This indicates the availability of potentially large surface area for adsorption. The start of mass gain in TG curve is an indicator of the initial stability of the synthesized samples (and hence the handling temperatures). The maximum mass gain peak in TG is due to the conversion of TaC into Ta_2O_5 [7]. This conversion is a two step process: release of carbon from the TaC followed by oxidation. The temperatures for these are indicated by the two peaks in DSC. The high temperature inflection point (≥700 °C) in TG curve, with a corresponding peak/hump in DSC, occurs at nearly the same temperature for all the samples and is attributed to oxidation and combustion of the carbonaceous residue [8]. The data obtained from the detailed analysis of the DSC/ TG curves for the select samples is listed in table 5.4.

In case the sample consists of pure TaC, its oxidation will result in 14.5 % increase in mass. In the present samples this is never achieved. Here the maximum increase encountered is 2 - 8 mass % after the initial weight loss stops. The TG curves become stable for all the samples at ~800 ^{0}C. The residual mass at these temperatures is used to calculate the free carbon content in the synthesized samples using the formula [9]:

$$\%\ free\ carbon = 100 \times \left[1 - 2 \times \frac{m_i M_{TaC}}{m_f M_{Ta2O5}}\right] \quad (5.1)$$

Where,

m_i: initial mass, m_f: final mass, M_{Tac}:molecular mass of Tac, M_{Ta2O5}: molar mass of Ta_2O_5.

The smaller increase in mass for these samples as compared with the expected value is due to the presence of carbonaceous content (graphitic as well as amorphous) in the synthesized samples [7]. As the sample is heated, the mass increase due to oxidation is being offset by the decrease in mass due to oxidation of carbonaceous residue. This implies that if more free carbonaceous content exists in the sample, the % mass gain will be smaller. The data in Table

5.4 shows that if initial carbon concentration is increased the % free carbon in the synthesized samples increase and hence a corresponding decrease in % mass gain in TG curves.

Table 5.4: The data obtained from the analysis of the DSC/TG curves for the synthesized samples.

Sample Name	Initial Stability (°C)	C removal Peak (°C)	Oxidation Peak (°C)	Mass Gain (%)	Final Mass (%)	Free Carbon (%)	Initial mass loss (%)
Ox02T	255	305	434	5.9	91	20.4	5.3
Ox10T	238	482	582	1.9	89	22	4.7
Ox01C	212	330	507	7.6	102	10.7	2.7
Ox02C	185	313	462	7.5	102	10.7	2.2
Ox03C	255	305	434	5.9	91	20.4	5.3
Ox20C	195	342	572	4.3	73	35.9	2.2
Ox60C	211	325	556	1.06	46	59.7	2.3

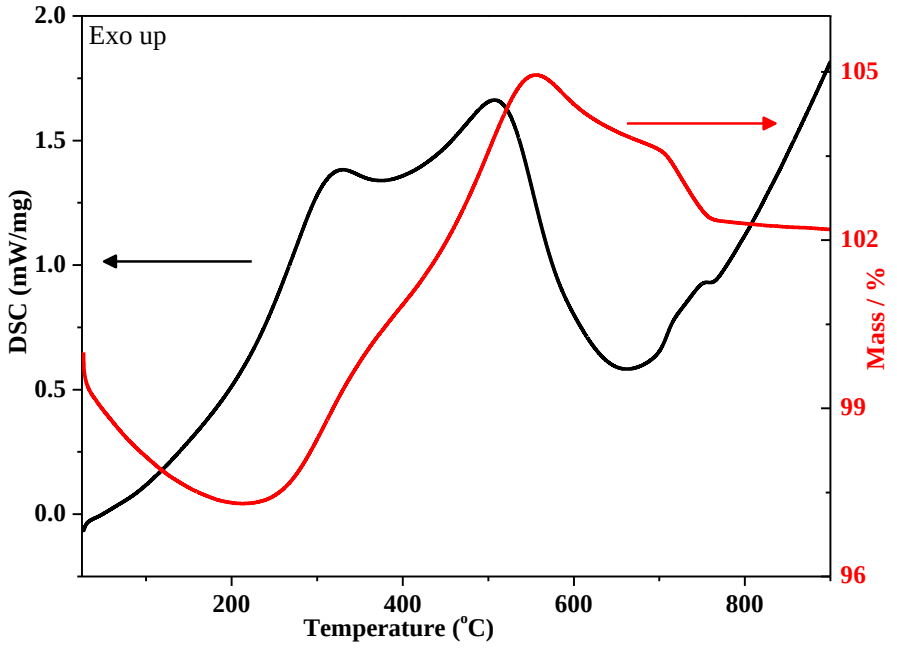

Figure 5.10: DSC-TG curves of Ox01C sample.

As the initial C concentration is increased, the net stability of the synthesized samples (the location of the C removal and oxidation peaks in DSC) decreases. This can be attributed to smaller size and increased strain in the particles (Table 5.2). When the initial C concentration was increased from 2 (Ox02C) to 3(Ox03C), the free carbon content in the samples nearly doubled whereas the carbon within the TaC remained the same (Table 5.3). Thus this thermal data supports the earlier conjecture that extra initial C forms a thick carbonaceous network around the particles which prevents the movement of carbon into the particles. The large initial mass loss for Ox03C sample corresponds with the smallest surface weighted size for this sample (Table 5.2). When the soaking time for the sample is increased (Ox02T to Ox10T) the locations of the DSC peaks indicate that the particles are more stable against oxidation. This is supported by the XRD data which shows that the sample consists of low strain large sized particles. The decrease in the initial stability for Ox10T sample is due to the increased free carbon content. This conjecture is further supported by the thermal data for the Ox20C and Ox60C. For both the cases the initial stability of the sample decreases as the free carbon content increases. Thus for a nano-carbide sample initially the increased free carbon content increases the initial stability of the powders but on further increase (>20%) it decreases. Comparing Ox01C and Ox60C samples it can be said that very high free carbon content in the system is detrimental to the quality of the sample by reducing not only the amount of the useful material but also deceasing the stability. Complete analysis of XRD and thermal data from Table 5.2-4 indicates that the initial stability and hence the handling temperature of the samples depends on the free carbon content whereas the oxidation stability depends on the carbon content within the lattice of the carbide phase as well as the size of the particles.

5.5 Microstructure analysis

Figure 5.11 (a) shows the representative FE-SEM images of the Ox01C sample. Agglomeration and carbon network are clearly visible, latter becoming denser for Ox03C sample (Figure 5.12). The average size calculated from Ox01C sample images is in the range of 7-10 nm.

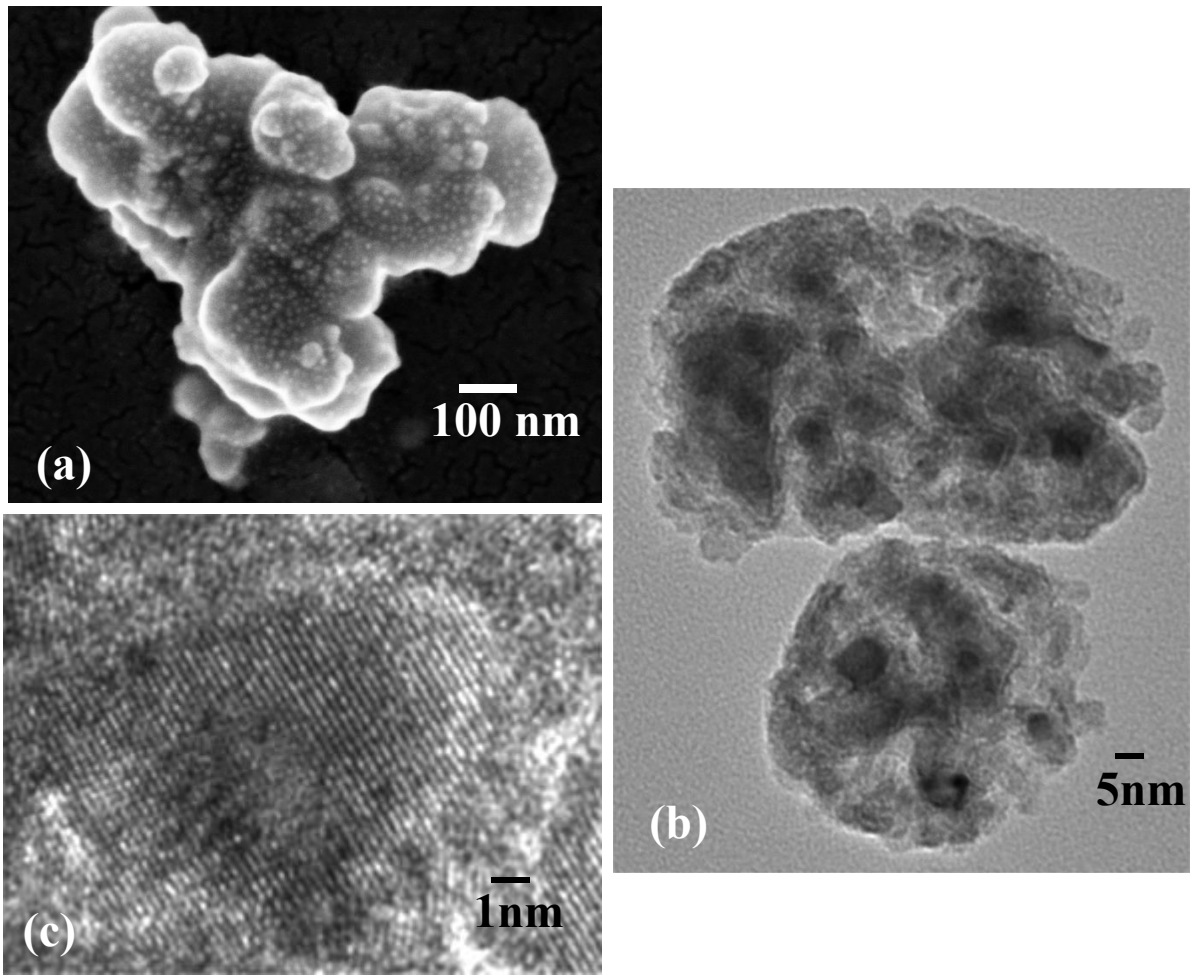

Figure 5.11: a) FE-SEM, b) TEM and c) HR-TEM images for the Ox01C sample.

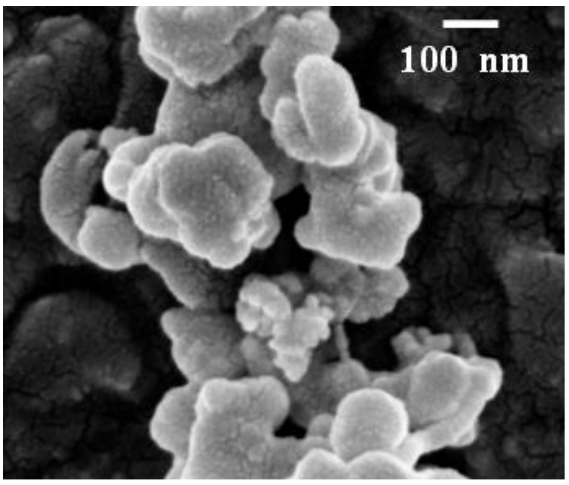

Figure 5.12: FE-SEM images for the Ox03C sample

Figure 5.11 (b) shows the representative TEM images of the synthesized TaC nanoparticles for Ox01C sample. The presence of carbon coating on the surface of each individual particle is clearly visible. Also the carbonaceous network in which the particles are embedded is seen. The morphology of carbon coated nanoparticles varies from faceted to spherical and these have a tendency to aggregate. Figure 5.11 (c) gives the High Resolution-TEM (HRTEM) image of a single crystalline TaC nanoparticle where the (111) facets of the particle is shown. The distance between the adjacent lattice fringes is the interplanar distance of cubic TaC (111), which is 0.26 nm (ICDD Pattern – 01-077-0205). This suggests that the synthesized TaC powder has cubic crystalline structure.

5.6 BET surface area analysis

N_2 sorption studies were done to obtain the BET surface area of the synthesized samples. Figure 5.13 shows the N_2 adsorption-desorption isotherms for the samples with increasing soaking times. The adsorption isotherms exhibit the characteristics of a type-II isotherm according to IUPAC classification [10,11]. An empirical classification of the hysteresis loops which gives information about the texture of the adsorbent has also been given by IUPAC and the isotherms show H-4 hysteresis characteristics [11,12]. This implies that the powders are forming a complex structure with both micropores and mesopores. This behaviour is because of the agglomeration of particles in the synthesized product.

The results are listed in Table 5.5. All the samples show large BET surface area. Analysis of the BET and XRD data shows that the largest surface area and the smallest pore diameter is for the samples with smallest size and it decreases with increasing size/soaking time.

Table 5.5: The data obtained from the analysis of the BET curves for the synthesized samples.

Sample Name	**BET Surface Area (m^2/g)**	**Average pore Diameter (nm)**	**Pore volume (cm^3/g)**
Ox01C	54.81	8.26	0.097
Ox02C	56.4	10.52	0.083
Ox03C	72.97	6.78	0.112
Ox01Q	78.53	8.14	0.139
Ox02T	72.97	6.78	0.112
Ox10T	61.07	8.31	0.122

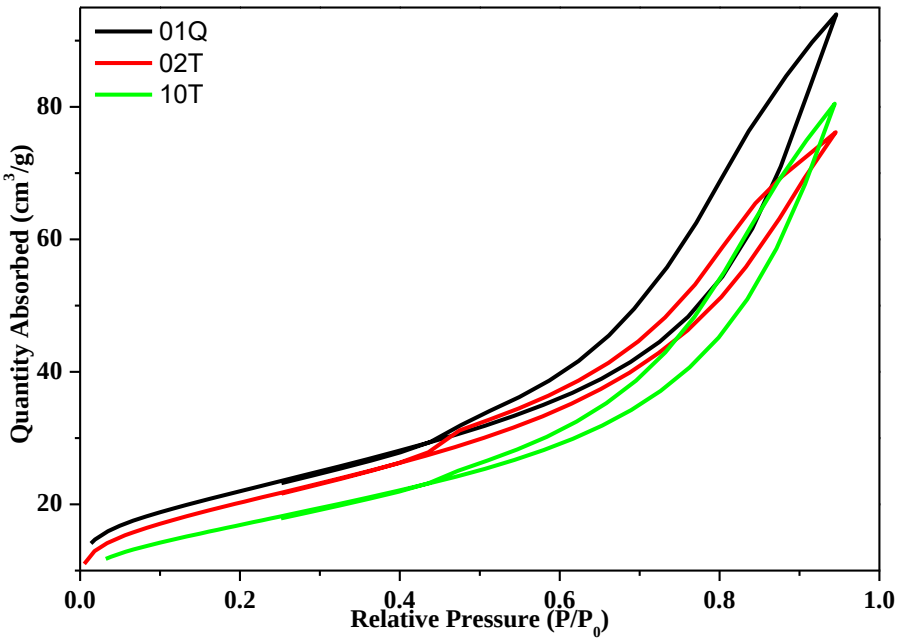

Figure 5.13: N_2 adsorption-desorption isotherms for the synthesized samples with increasing soaking times.

5.7 Thermodynamic analysis and synthesis mechanism

During heating of the autoclave, Mg being highly reactive substance absorbs oxygen from the air present inside the autoclave and forms MgO. MgO, being one of the most active catalysts for reduction, results in reduction of the acetone to hydrogen and carbon above 200 °C [13]. The decomposition of acetone leads to an excess of C and H_2 within the autoclave. The carbon (C) and hydrogen (H_2) produced as a result of decomposition along with Mg can act as reducing agents for Ta_2O_5. The first step in reduction of Ta_2O_5 occurs via conversion to TaO_2. Four possible reduction reactions can be expressed as:

$$2Ta_2O_5 + C \rightarrow 4TaO_2 + CO_2 \quad (5.2)$$

$$Ta_2O_5 + C \rightarrow 2TaO_2 + CO \quad (5.3)$$

$$Ta_2O_5 + H_2 \rightarrow 2TaO_2 + H_2O \quad (5.4)$$

$$Ta_2O_5 + Mg \rightarrow 2TaO_2 + MgO \quad (5.5)$$

The ΔG values for the above reactions at the standard pressure at different temperatures can be calculated by:

$$\Delta G = \Delta G^0 + \Delta H - T\Delta S \quad (5.6)$$

$$\Delta H = \int_{T_r}^{T} C_p dT \quad (5.7)$$

$$\Delta S = \int_{T_r}^{T} \frac{C_p}{T} dT \quad (5.8)$$

$$C_p = \Delta a + \Delta b\, T + \Delta c\, T^{-2} \quad (5.9)$$

Where, Δa, Δb, and Δc are the thermodynamic data of reactants and products at the standard state.

The variation of ΔG with temperature for the Ta_2O_5 reduction with C, H_2 and Mg is shown in Figure 5.14(a). The curves show that although all the reactions are non-spontaneous (ΔG > 0), the reduction becomes more favorable as the temperature increases. The reaction involving Mg is more favourable at all temperatures. The reduction reactions involving Mg and C are a solid-solid reaction whereas that for H_2 is solid-gas reaction [14].

The H_2 being a small molecule has a large diffusion coefficient. So it is able to diffuse into the Ta_2O_5 particles whereas C coats the outside of the Ta_2O_5 particles. Even at lower temperatures (< 650 °C) the reduction due to hydrogen (which is exothermic) is possible due to the size of the initial powder (130-220 nm) which allows for large contact and solid-gas nature of the reaction [15]. This reduction is extremely small in amount and only occurs for the diffused hydrogen because of low partial pressure of H_2O inside [14,15]. The exothermic reduction reaction leads to formation of steam which fragments Ta_2O_5 powders. This conjecture is supported by the broadened XRD peaks at lower temperatures and no signature of TaO_2. The small final size of the synthesized powders in present work is attributed to this initial reduction of size for Ta_2O_5 [2].

The fragmented Ta_2O_5 gets coated immediately with carbon present in the autoclave. This carbon coating prevents the fragmented oxide particles from coalescing. The carbon coating also helps to increase the reaction rate for reduction and carburization by ensuring the close

proximity of the reactants. For the fragmented Ta_2O_5 the reduction process proceeds at a faster rate due to reduced size and higher surface area of fragmented particles.

The decrease in the transformation temperature seen here is a combined effect of the reduced size of the Ta_2O_5 as well as addition of Mg which is energetically more favourable reductant. This is supported by existence of critical initial stoichiometry of Mg needed for complete transformation into TaC at 800 °C. Once the reaction starts the reduction proceeds via C and H_2 reduction pathways as well as Mg. This will be expected since the C and H_2 are in more intimate contact with the initial powders whereas Mg is in the form of solid powder [16]. Also, all the reactions are exothermic so once the reaction starts the local temperature will increase making all reaction pathways possible [2]. The detailed morphology of the Mg powder may also have an effect on its critical stoichiometry and needs to be studied further. As the temperature increases the reduction reactions become more favourable increasing the reaction rate.

For the further reduction of TaO_2 the following reactions are possible:

$$TaO_2 + C \rightarrow TaO + CO \quad (5.10)$$

$$TaO_2 + H_2 \rightarrow TaO + H_2O \quad (5.11)$$

$$TaO_2 + Mg \rightarrow TaO + MgO \quad (5.12)$$

$$TaO_2 + 2C \rightarrow Ta + 2CO \quad (5.13)$$

$$TaO_2 + 2H_2 \rightarrow Ta + 2H_2O \quad (5.14)$$

$$TaO_2 + 2Mg \rightarrow Ta + 2MgO \quad (5.15)$$

Figure 5.14(b) clearly shows that reduction of TaO_2 to Ta in single step is a spontaneous process with reduction reactions involving C and H_2 being comparable but that for Mg being more probable from the energy point of view at the temperature of interest (≤ 700 °C). Since the TaO_2 particles are smaller in size as well as encapsulated in carbon so this reaction

proceeds at a faster rate and the Ta particles formed will be strained. This is supported by the XRD data which clearly shows the formation of pure cubic phase highly strained Ta nanoparticles at 700 °C.

The final possible carburization reactions are:

$$Ta + C \rightarrow TaC \tag{5.16}$$

$$Ta + C \rightarrow Ta_2C \tag{5.17}$$

$$Ta_2C + C \rightarrow 2TaC \tag{5.18}$$

Reactions 5.16 and 5.17 are competing reactions. Thermodynamic calculations show that the formation of Ta_2C is more favourable (Fig. 5.14(c)). So the Ta nanoparticles are carburized initially to Ta_2C and finally to TaC. Both these reaction steps will be very fast as both the reactions are spontaneous. This is supported by the XRD data where Ta_2C and TaC are formed simultaneously for the 750 °C sample. But the complete conversion to TaC takes place only at 800 °C. This indicates that the diffusion of carbon inside the particles is the reaction rate hindrance step. Increase in temperature increases the diffusion and results in complete final phase formation in 1 hour.

So the complete reaction pathway for the synthesis of TaC from Ta_2O_5 is:

$$Ta_2O_5 \longrightarrow TaO_2 \xrightarrow{700\,C} Ta \xrightarrow{750\,C} Ta_2C + TaC \xrightarrow{800\,C} TaC$$

The formation mechanism is depicted in Figure 5.15.

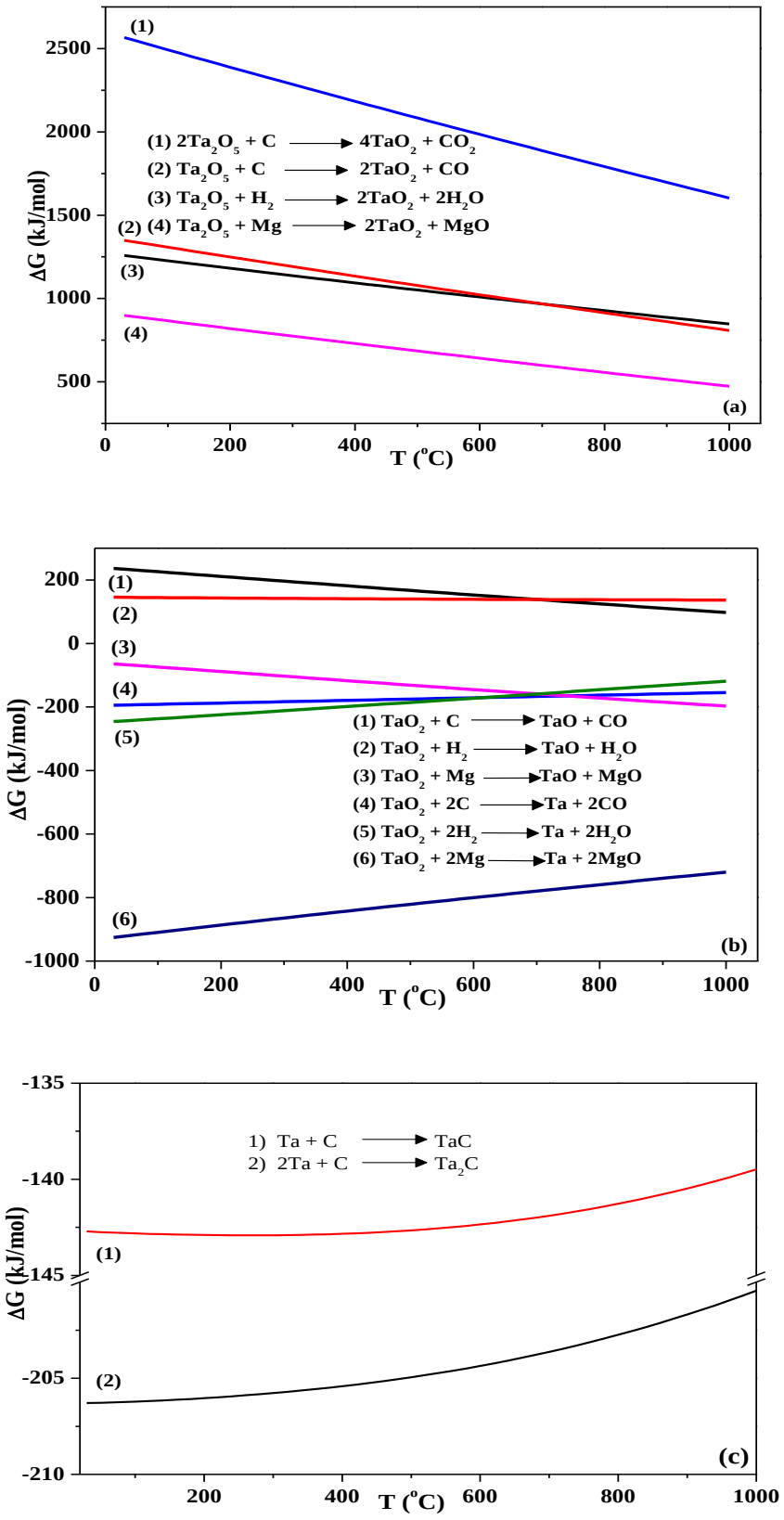

Figure 5.14: Thermodynamic calculations for the possible reactions during reduction and carburization.

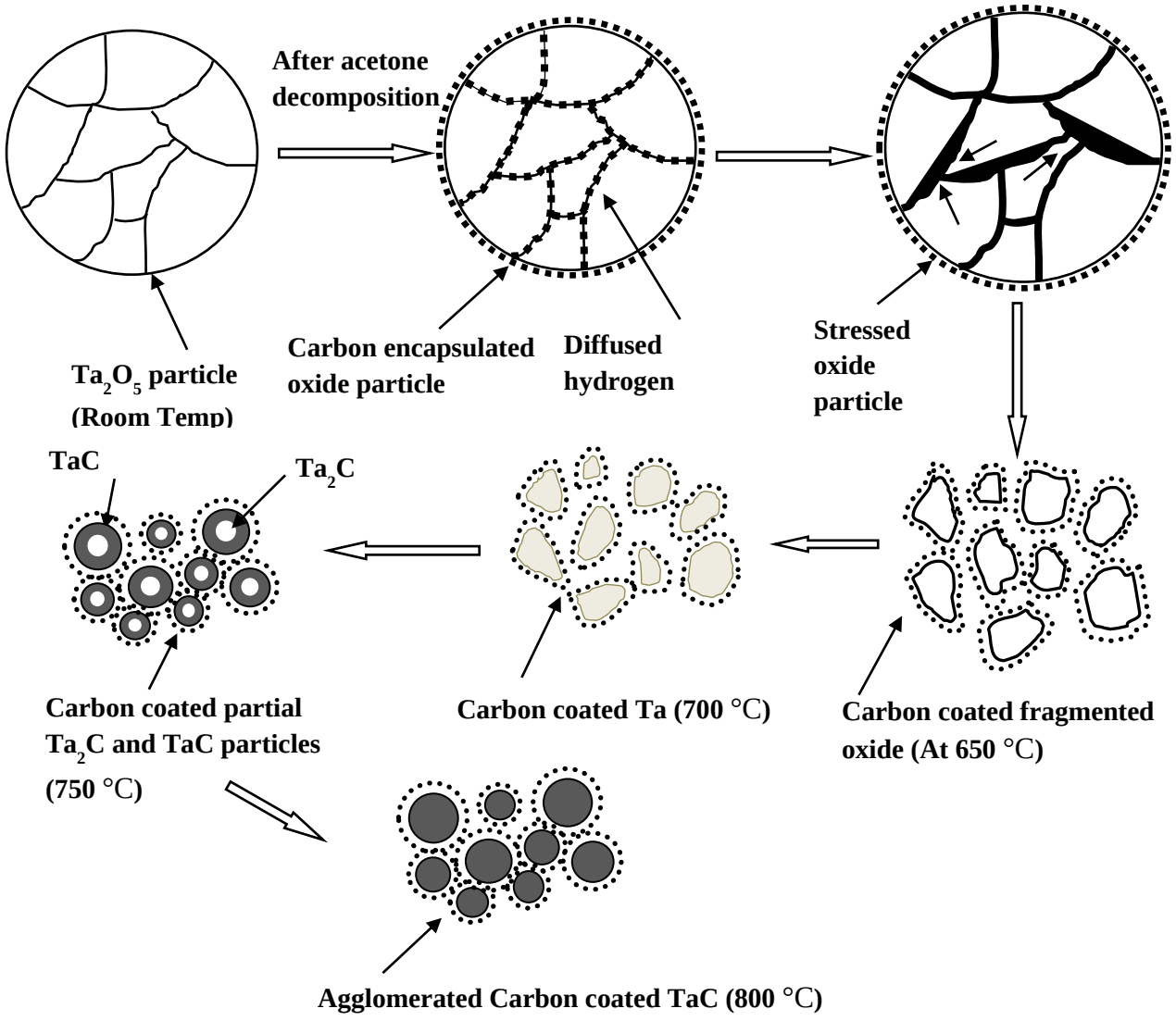

Figure 5.15: The mechanism for transformation of Ta_2O_5 into TaC nanoparticles (The arrows within the stressed oxide particle represent the beginning of cracks).

References:

[1]. J.P. Kelly, O. A. Graeve, *J. Am. Ceram. Soc.* **94** (2011)1706–1715.

[2]. L.K. Brar, G. Singla, N. Kaur, O.P. Pandey, *J Therm Anal Calorim*. **119** (2015) 175-182.

[3]. A.J. Haslam, S.R. Phillpot, D. Wolf, D. Moldovan, H. Gleiter, *Mater. Sci. and Eng., A* **318** (2001) 293-312.

[4]. D. Moldovan, D. Wolf, S. R. Phillpot and A. J. Haslam, *Acta Mater.*, **50** (2002) 3397–3414.

[5]. R. Chaim, *Scripta Mater.* **66** (2012) 269–271.

[6]. H.G. Merkus *Particle Size Measurements: Fundamentals, Practice, Quality* Springer Science & Business Media B.V, Dordrecht, Netherland (2009).

[7]. N.S. Alhajri, H. Yoshida, D.H. Anjum, A.T. Garcia-Esparza, J. Kubota, K. Domend, K. Takanabe, *J. Mater. Chem., A* **1** (2013) 12606-12616.

[8]. D.-H. Kwon, S.-H. Hong, B.-K. Kim, *Mater. Chem. Phys.* **93** (2005) 1–5.

[9]. A.L. Tomas-Garcia, Q. Li, J.O. Jensen, N.J. Bjerrum, *Int. J. Electrochem. Sci.* **9** (2014) 1016-1032.

[10]. Y.-J. Lee, S.H. Kima, T.-H. Lee, H.H. Nersisyanb, K.-H. Lee, M.-H. Hana, S.-U. Jeong, K.-S. Kang, K.-K. Bae, J.-H. Lee, *Chem. Eng. Sci.* **107** (2014) 227–234.

[11]. W. Wang, P. Liu, M. Zhang, J. Hu, F. Xing, *Open J. Compos. Mater.* **2** (2012) 104-112.

[12]. M. Thommes, *Chem. Ing. Tech.* **82** (2010) 1059-1073.

[13]. V.K. Díez, C.R. Apesteguía, J.I. Di Cosim, *Lat. Am. Appl. Res.* **33** (2003) 79–86.

[14]. A. Kumar, K. Singh and O.P. Pandey, *J. Mater. Sci. Technol*. **30** (2014) 112-116.

[15]. S. Luidold, H. Antrekowitsch, *J. Minerals Metals & Mater. Soc*. **59** (2007) 20–26.

[16]. T.H. Kim, J.H. Yu, J.S. Lee *NanoStuct. Maters*. **9** (1997)213-216.

CHAPTER 6

Nano-TaC from Tantalum (V) Chloride

Overview

In this chapter the synthesis and characterization of the nano TaC from Tantalum chloride is discussed. The XRD results of all the samples synthesized at different temperatures and times are described. The lattice carbon content of the TaC nanopowders, size and strain has been used to determine the evolution of the nanopowders with time as well as temperature. Based on XRD results, the formation mechanism of the nano particles has been proposed. From the thermal analysis results, the stability of the synthesized powders over range of temperature(s) has been evaluated. FE-SEM and TEM results have been discussed to analyse the microstructure of the synthesized powders and to confirm the crystal structure of product phase by measuring the lattice spacing using HRTEM. Surface area and pore size distribution of the synthesized samples has been analysed by BET technique.

6.1 Samples

The experiments to obtain single phase TaC were planned by varying holding temperature and holding time. The initial carbon concentration and magnesium content were kept constant. All the single phase samples obtained using $TaCl_5$ and their synthesis parameters are listed in Table 6.1.

Table 6.1: Single phase samples synthesized using $TaCl_5$ (Initial carbon concentration = 3, Magnesium molar ratio = 9 for all the samples)

Sample Name	Time (h)	Temperature (°C)
Cl08h650	8	650
Cl10h650	10	650
Cl12h650	12	650
Cl08h700	8	700
Cl10h700	10	700
Cl12h700	12	700
Cl01h800	1	800
Cl02h800	2	800
Cl05h800	5	800
Cl08h800	8	800
Cl10h800	10	800
Cl12h800	12	800

6.2 X-ray diffraction (XRD) analysis

XRD data of few selected samples obtained from soaking the autoclave for different durations at temperatures (500 °C – 800 °C) is presented in Figure 6.1. XRD data clearly shows that the cubic TaC phase is present even for 2 h soaking at 600 °C but the conversion in not complete. Increasing the soaking time decreases the intensity of the oxide peaks but the conversion is not complete even for 12 h sample. For the samples soaked at 650 °C and 700 °C pure cubic phase TaC is formed only for soaking of 8 h and above. At 800 °C the pure cubic phase TaC (ICDD Pattern – 01-077-0205) is formed even for 1 h soaking. A detailed analysis of the partially converted samples has been done to propose the formation mechanism for TaC (section 6.6).

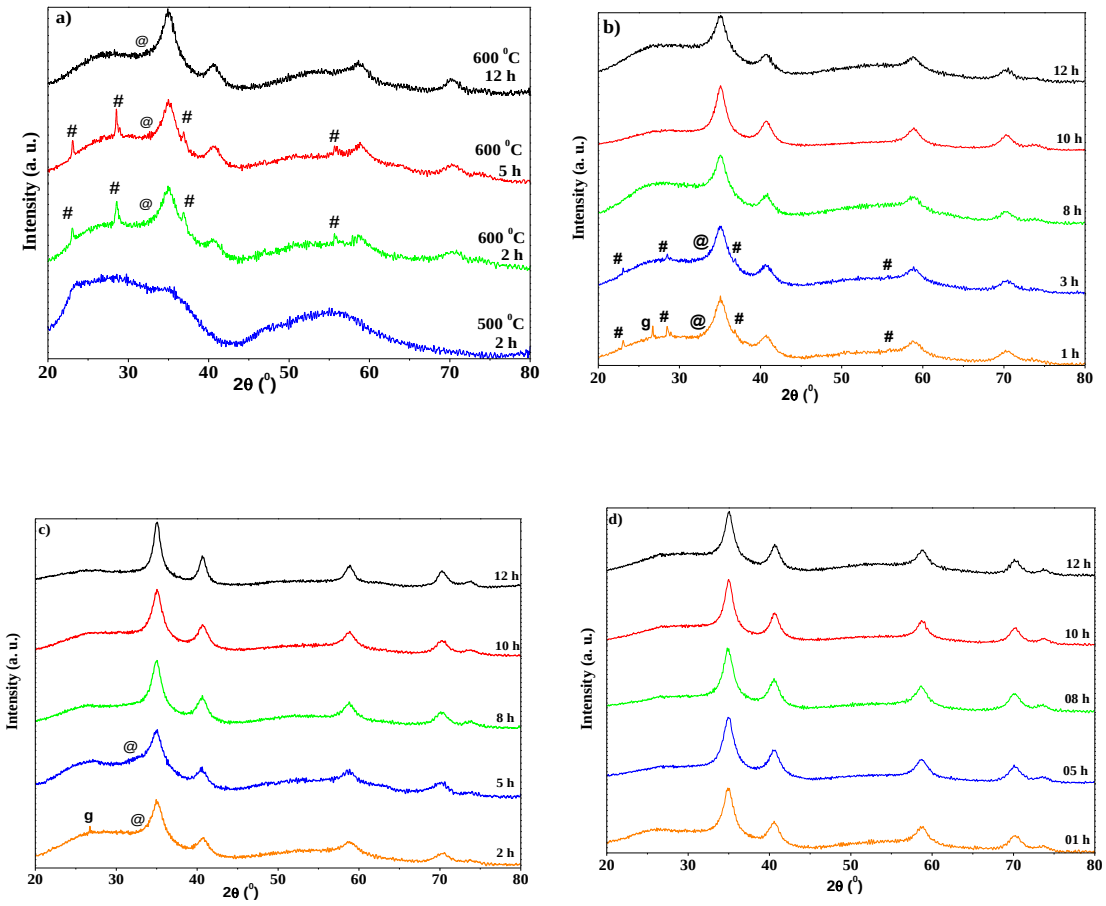

Figure 6.1: XRD line profiles for the selected synthesized sample at different temperatures a) 500 °C and 600 °C b) 650 °C c) 700 °C d) 800 °C . (#: h-Ta_2O_5 (ICDD – 00-018-1304), @: c-T_2O(ICDD – 00-018-1302), g: graphitic carbon)

Figure 6.2 – 6.4 show the representative graphs obtained for the Rietveld and the double-Voigt integral breadth analysis for the single phase samples. The results obtained from the Rietveld analysis (***a***, ***x***, $\boldsymbol{\chi^2}$, $\mathbf{R_{wp}}$) and double-Voigt integral breadth method analysis of the XRD line profiles (volume weighted size (D_V), surface weighted size (D_S), strain) are given in Table 6.2. From Table 6.2 it is clear that all the single phase samples have the lattice carbon content (***x***) of 0.89 or more. The time evolution of ***x***, strain and size for the samples soaked at 800 °C is presented in Figure 6.5.

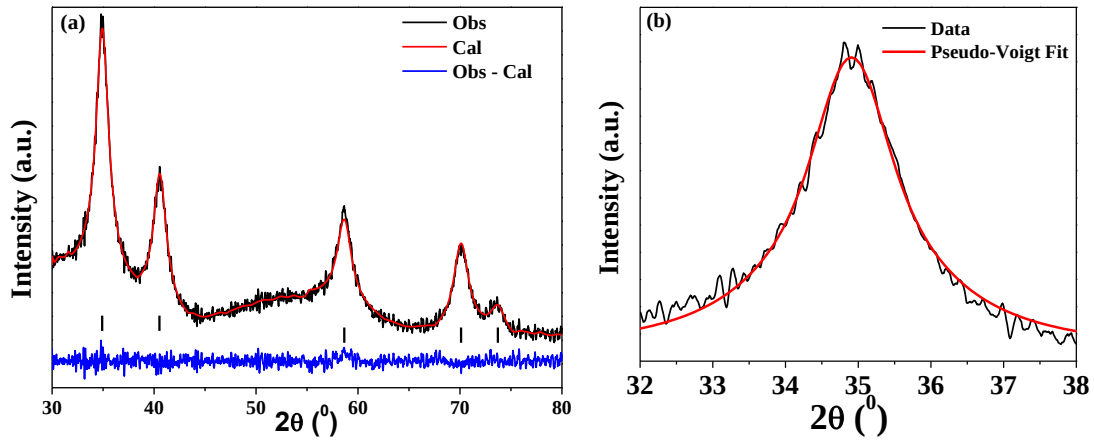

Figure 6.2: (a) Rietveld refinement plots for the Cl08h800 sample. Tick marks indicate allowed peak positions. (b) The result of the pseudo-Voigt curve fit routine for the (111) peak of Cl08h800 sample.

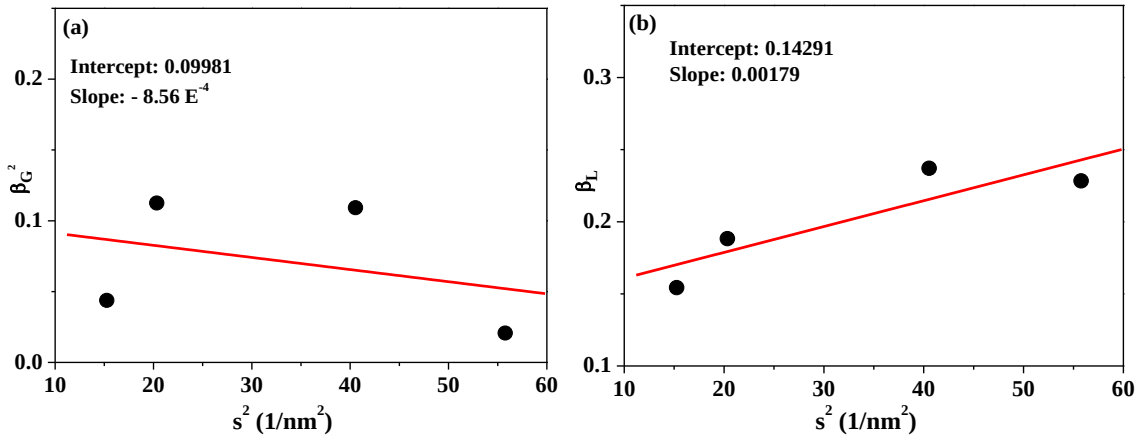

Figure 6.3: Double-Voigt Integral breadth analysis graphs ((a) and (b)) of 12h800 sample.

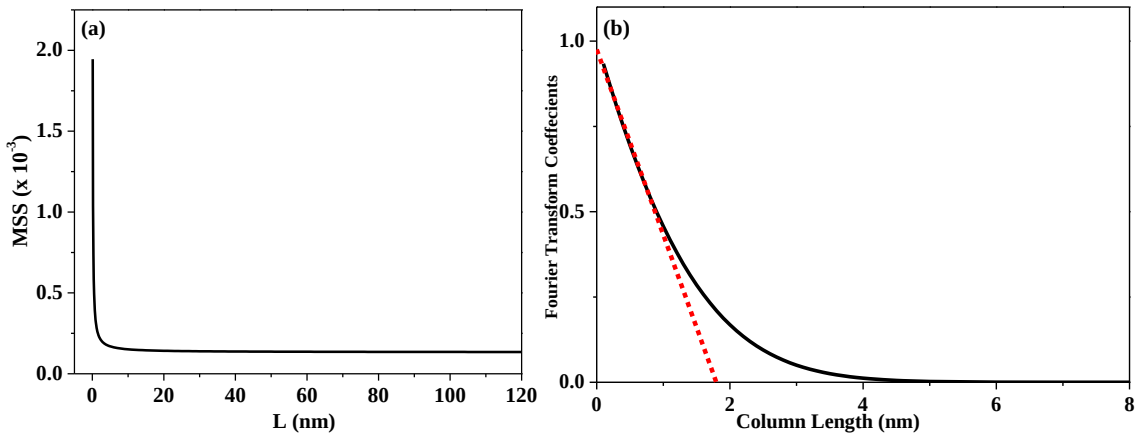

Figure 6.4: (a) Mean Square Strain (MSS) as a function of column length (L) for (111) plane for Cl12h800 sample. All the samples were isotropic in nature. (b) The initial slope of the Fourier transform graph is used to determine the surface weighted particle size for TaCl08h800 sample.

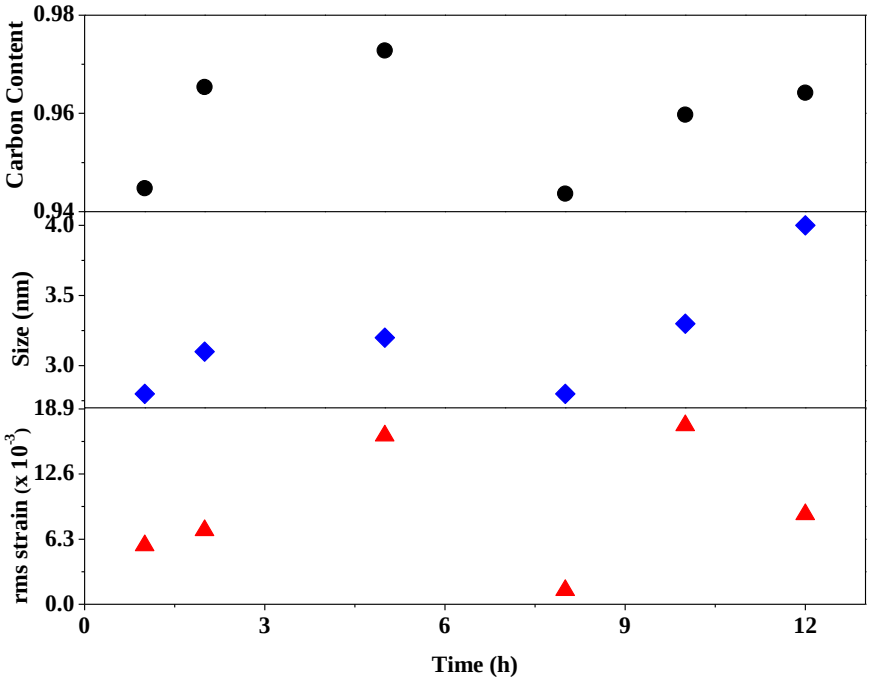

Figure 6.5: Time evolution of powder characteristics for samples synthesized at 800 °C .

Table 6.2: XRD analysis results from the D-V line analysis.

Sample Name	*a* (nm)	*x*	χ^2	R_{wp}	D_V (nm)	D_S (nm)	RMSS (x 10^{-3}) at 3 nm
Cl08h650	0.44541	0.98	0.38	2.22	3.5	1.8	18.2
Cl10h650	0.44465	0.93	0.47	2.34	3.2	1.9	5.58
Cl12h650	0.44522	0.97	0.42	2.31	5.1	1.7	20.3
Cl08h700	0.44492	0.95	0.43	2.28	2.8	1.8	4.77
Cl10h700	0.44500	0.96	0.40	2.23	3.8	1.9	14.0
Cl12h700	0.44406	0.89	0.50	2.37	4.3	2.2	14.5
Cl01h800	0.44484	0.94	0.44	2.43	2.8	1.9	5.69
Cl02h800	0.44516	0.97	0.55	2.45	3.1	1.9	7.15
Cl05h800	0.44528	0.97	0.40	2.23	3.2	1.8	16.3
Cl08h800	0.44482	0.94	0.44	2.44	2.8	1.8	1.36
Cl10h800	0.44507	0.96	0.40	2.29	3.3	1.8	17.3
Cl12h800	0.44514	0.96	0.40	2.26	4.1	2.2	8.71

Initially as the soaking time is increased there is no appreciable change in the size but the ***x*** as well as strain within the particles increases. For the 8 h sample there is a simultaneous decrease in strain and lattice carbon content. Further increase in soaking time results in grain growth. Absence of grain growth initially in spite of increase in ***x*** and strain implies that the TaC formation at 800 °C is fast and the single phase particles formed need to stabilize, which happens for 8 h soaking. This result is different than that for powders synthesized from Ta_2O_5 where the stability is achieved for 2 h soaking. This increase in time to achieve complete stabilization happens because of the present Ta precursor. Due to the faster rate of carbon diffusion at 800 °C the crystallization of Ta_2O_5 as well as TaC formation happens simultaneously which leads to inherently more unstable particles. This conjecture is supported by the low temperature synthesis where the rate of carbon diffusion is slow and single phase powders are formed only for 8 h. For these powders (Cl08h650, Cl08h700) the lattice carbon content is high and the grain growth starts immediately even though the excess carbon is expunged at a later stage.

The surface weighted size for all the samples is smaller than the corresponding volume weighted size and does not change appreciably for any of the samples.

6.3 Thermal analysis

The thermal stability and oxidation resistance of the synthesized powders was analyzed by DSC/TG/DTG. Figure 6.6 shows the DSC-TG-DTG curves for the Cl10h800 sample which are representative for all the synthesized samples.

The main observations from the thermal analysis of the samples are as follows: Initial heating of the samples from room temperature results in mass loss due to loss of the surface adsorbed species from the particle surface. This is followed by gain in mass. The mass gain is due to the conversion of TaC into Ta_2O_5 [1]. This conversion is a two-step process: release of carbon from the TaC followed by oxidation. However, due to the small size of the particles and the sub-stoichiometric carbon content within the carbide lattice ($\boldsymbol{x} < 1.0$) both the processes occur simultaneously as indicated by observation of a single peak in DSC. The start of mass gain is an indicator of the initial stability of the synthesized samples (and hence the handling temperatures). The handling temperature for the given sample is obtained from the point where the slope of initial mass loss changes/decreases indicating the start of mass gain.

This is determined from DTG. The temperature of maximum mass gain in TG is a signature of the overall stability of the samples. High temperature inflection point (≥700 °C) in TG curve, with a corresponding peak/hump in DSC, occurs at nearly the same temperature for all the samples and is attributed to oxidation and combustion of the carbonaceous residue [2].

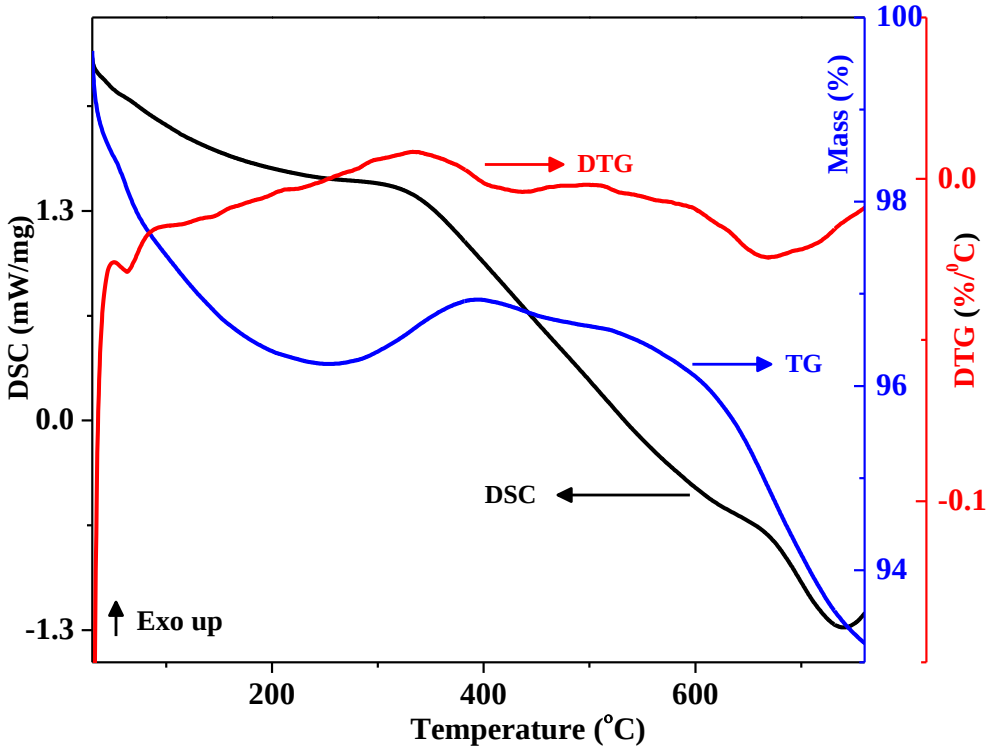

Figure 6.6: DSC-TG-DTG curves of Cl10h800 sample.

Table 6.3: Thermal analysis results for the TaC powders synthesized from $TaCl_5$.

Sample Name	Handling temperature °C	Max stability °C	Mass gain %	Final mass %	% free C
Cl10h650	142	430	1.6	92.15	19.5
Cl10h700	119	355	0.6	93.70	18.2
Cl10h800	107	392	0.7	93.23	18.5
Cl02h800	135	360	0.5	92	19.6

Table 6.3 gives the data obtained from the detailed analysis of the DSC/ TG/ DTG curves for the selected samples. If a sample consists of pure TaC, its oxidation will result in 14.5% increase in mass. In our samples this is never achieved. For our samples the maximum

increase encountered is 0.5 - 2 mass% after the initial weight loss stops. The smaller increase in mass for our samples as compared with the expected value is due to the presence of carbonaceous content (graphitic as well as amorphous) in the synthesized samples [1]. As the sample is heated the mass increase due to oxidation is being offset by the decrease in mass due to oxidation of carbonaceous residue.

The TG curves become stable for all the samples at ~800 °C. The residual mass at these temperatures is used to calculate the free carbon content in the synthesized samples using the formula [3]:

$$\%\ free\ carbon = 100 \times [1 - 2 \times \frac{m_i M_{TaC}}{m_f M_{Ta2O5}}] \quad (6.1)$$

Where,

m_i: initial mass, m_f: final mass, M_{Tac}:molecular mass of TaC, M_{Ta2O5}: molar mass of Ta_2O_5.

The final mass and hence the % free carbon in all the samples is nearly same so the thermal behaviour of the system is a signature of the size and strain of the powders. As is evident from the comparison of Tables 6.2 and 6.3, the low strain sample Cl10h650 is most stable, inspite of smaller size and low lattice carbon content. The stability trend follows the sample strains. The exception is 10h800 sample. This sample has higher final stability as compared to the 02h800 sample in spite of the higher strain. This increase in stability is attributed to the fact that the Cl02h800 and Cl10h800 samples lie on the different sides of the point where the synthesized samples released the initial strain and achieved the stable configuration. This result strengthens/confirms our earlier conjecture from XRD data analysis where the TaC samples are formed within 1 hr at 800 °C, the system needs time to stabilize/relax.

6.4 Microstructure analysis

Figure 6.7 (a, b) show the representative FE-SEM images for the TaC powders. Agglomeration of particles is clearly visible. Figure 6.7 (c, d) show the representative TEM images of the synthesized TaC powders. The agglomeration, carbon coating of individual particles and the carbonaceous network in which the nanoparticles are embedded are visible. The particles have irregular to faceted morphology. Figure 6.7 (e) gives the High Resolution-TEM (HRTEM) image of a single crystalline TaC nanoparticle and shows the (111) facets of the particle. The distance between the adjacent lattice fringes is the interplanar distance of cubic TaC (111), which is 0.256 nm (ICDD Pattern – 01-077-0205). This suggests that the

synthesized TaC powder has cubic crystalline structure. The same is also confirmed by the analysis of the ring pattern from the SAED (Figure 6.7 (f))

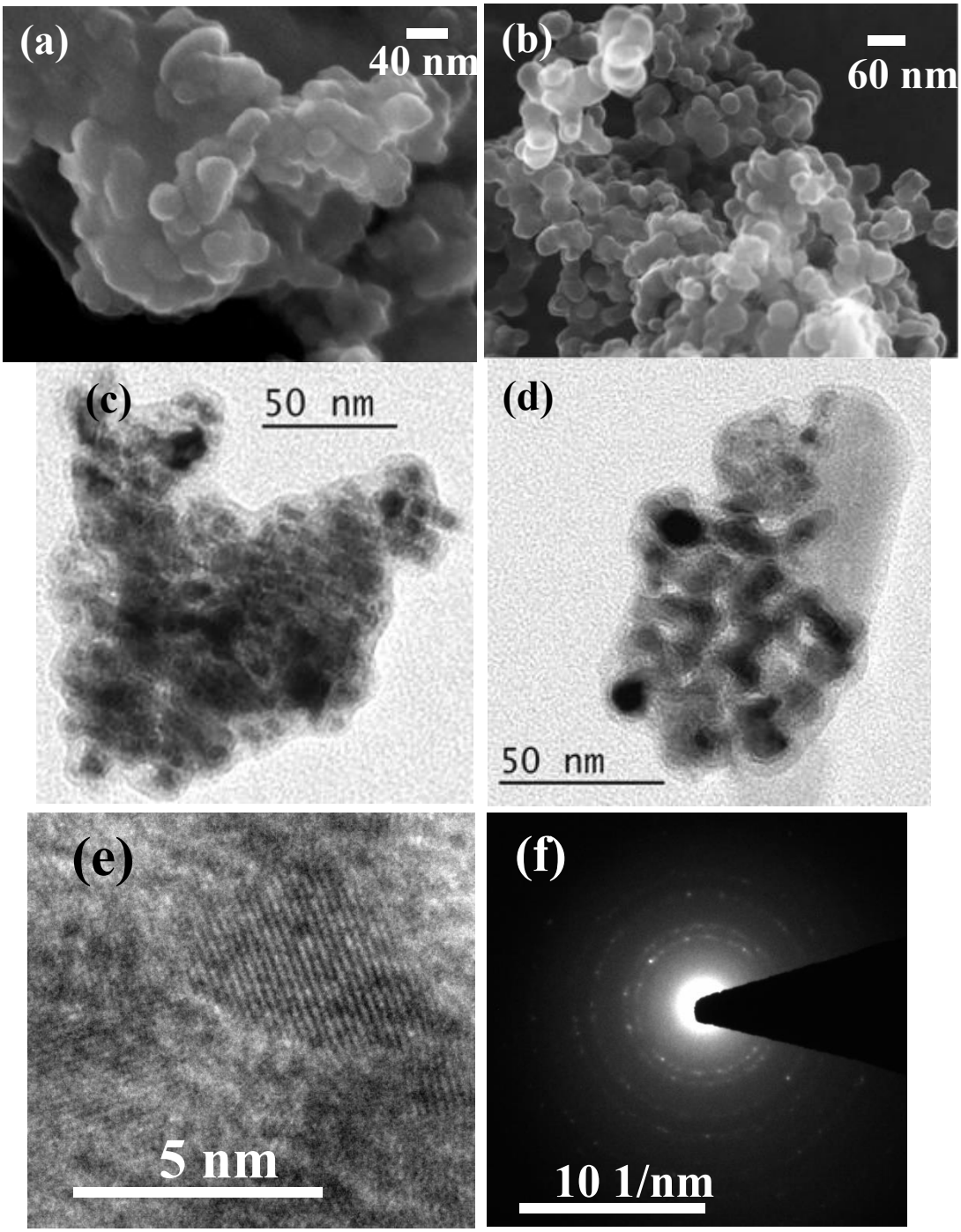

Figure 6.7: Morphological characterization: FE-SEM images for the samples soaked for 10 h at a) 800 °C b) 650 °C. TEM images for the samples soaked for 10 h at c) 800 °C d) 650 °C. e) HR-TEM image f) SAED pattern for the TaC nanopowder.

6.5 BET surface area analysis

N_2 sorption studies were done to obtain the BET surface area of the synthesized samples. All the adsorption isotherms exhibit the characteristics of a type-II isotherm according to IUPAC classification [4,5]. The hysteresis of the loops, which gives information about the texture of the adsorbent, has also been classified empirically by IUPAC. In the present case the isotherms show H-4 hysteresis characteristics [5,6]. This implies that because of the agglomeration of particles in the synthesized product the powders are forming a complex structure with both micropores and mesopores. Figure 6.8 shows the N_2 adsorption-desorption isotherms for the samples with increasing soaking times at 800 °C.

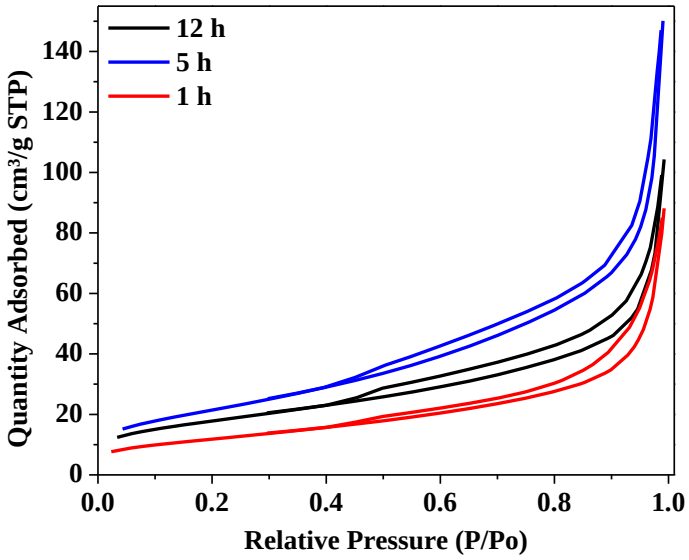

Figure 6.8: N_2 adsorption-desorption isotherms for the synthesized samples with increasing soaking times at 800 °C.

The results obtained from the analysis of the N_2 sorption studies are listed in Table 6.4. Analysis of the BET and XRD data shows that even though the surface weighted sizes of all the samples is nearly same there is difference in the observed BET surface area values. For same soaking time with increasing temperature the change in BET surface area is not significant but when the soaking time is increased at constant temperature, the maximum surface area is for the sample with maximum strain (Cl05h800). It is believed that this is a signature of the fact that the strain in the particles along with the particle size is an important parameter for determining the adsorption properties of the synthesized powders at this length scale [7].

Table 6.4: The data obtained from the analysis of the N_2 adsorption-desorption isotherms for the synthesized samples.

Sample Name	BET Surface Area (m^2/g)	Average pore Diameter (nm)	Pore volume (cm^3/g)
12h650	58.4	8.9	0.130
12h700	54.1	12.4	0.166
01h800	43.2	12.0	0.129
05h800	75.1	12.3	0.231
12h800	59.6	10.4	0.155

6.6 Synthesis mechanism

During heating of the autoclave, Mg being highly reactive substance absorbs oxygen from the air present inside the autoclave and forms MgO. MgO, being one of the most active catalysts for reduction, results in reduction of the acetone to hydrogen and carbon above 200 °C [8]. In air $TaCl_5$ decomposes at 240 °C via formation of Ta_2O_5 and HCl and/or Cl_2. Within the autoclave we expect it to form Ta_2O_5, $MgCl_2$ and HCl. From the initial time data for low temperatures (Figure 4.26 (a)) it is clear that only for holding temperature T >500 °C the crystalline Ta_2O_5 (ICDD – 00-018-1304) is formed. Since the reaction takes place inside the enclosed atmosphere of an autoclave so it is not possible to predict the exact steps/temperatures for the conversion and the reaction products formed. The $MgCl_2$ was present in all the unleached, as synthesized powders. Ta_2O_5 thus formed is completely covered by the carbon produced during the decomposition of acetone. The carbon coating helps to increase the reaction rate for further reduction and carburization by ensuring the close proximity of the reactants. Moreover, the carbon coating also prevents the oxide particles from coalescing which ensures that the final product is in nanometer range [9]. Initial time data also clearly shows that the Ta_2O_5 conversion to TaC takes place via initial reduction to Ta_2O (ICDD – 00-018-1302). In the entire set of experiments no evidence of Ta or Ta_2C was found in any of the samples. Since the carbon is present in sufficiently high concentration so it is possible that Ta obtained from reduced oxide may get immediately converted into Ta_2C and further to TaC. This conjecture is supported by the thermodynamic calculations which indicate that the carburization reactions are spontaneous (Figure 5.14 (c), chapter 5). So the complete reaction pathway for the synthesis of TaC from $TaCl_5$ is:

$$TaCl_5 \xrightarrow{>500\ C} Ta_2O_5 \longrightarrow TaO_2 \longrightarrow TaC$$

Reaction rate within the autoclave is very high as is evident from > 70 % conversion within 2 hrs for all the temperatures > 600 °C. However, the complete conversion needs 8 hrs at 650 °C (Figure 6.1 (b)). The higher time required for complete conversion proves that the carbon diffusion is the rate determining step for the reaction. In order to facilitate the entire process the travel rate of carbon can be made faster by increasing the soaking temperature as is evident from Figure 6.1 (d) where complete conversion is taking place at 800 °C in 1 h. Figure 6.9 gives the schematic of the proposed mechanism.

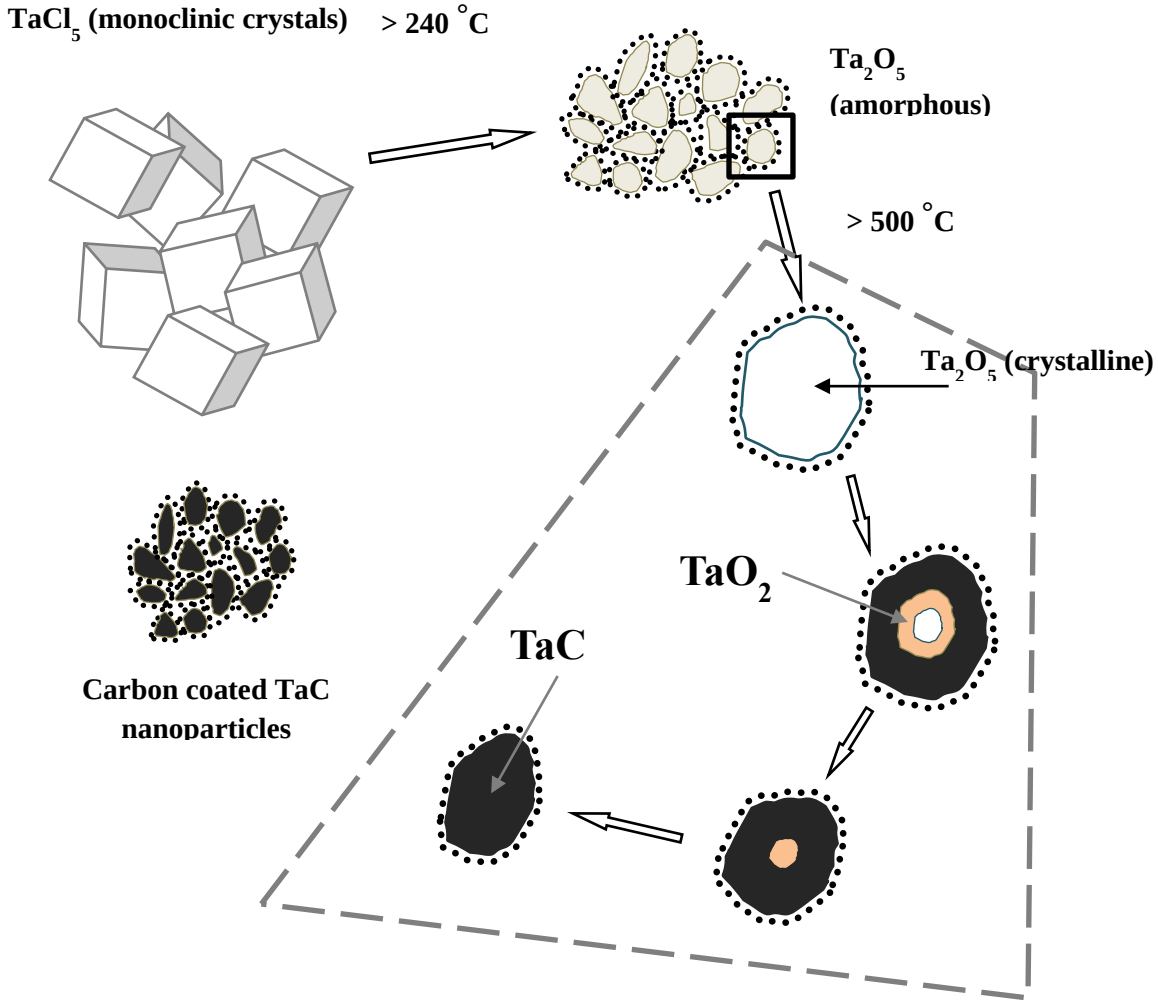

Figure 6.9: The mechanism for transformation of $TaCl_5$ into TaC nanoparticles.

References:

[1]. N.S. Alhajri, H. Yoshida, D.H. Anjum, A.T. Garcia-Esparza, J. Kubota, K. Domend, K. Takanabe, *J. Mater. Chem., A* **1** (2013) 12606-12616.

[2]. D.-H. Kwon, S.-H. Hong, B.-K. Kim, *Mater. Chem. Phys.* **93** (2005) 1–5.

[3]. A.L. Tomas-Garcia, Q. Li, J.O. Jensen, N.J. Bjerrum, *Int. J. Electrochem. Sci.* **9** (2014) 1016-1032.

[4]. Y.-J. Lee, S.H. Kima, T.-H. Lee, H.H. Nersisyanb, K.-H. Lee, M.-H. Hana, S.-U. Jeong, K.-S. Kang, K.-K. Bae, J.-H. Lee, *Chem. Eng. Sci.* **107** (2014) 227–234.

[5]. W. Wang, P. Liu, M. Zhang, J. Hu, F. Xing, *Open J. Compos. Mater.* **2** (2012) 104-112.

[6]. M. Thommes, *Chem. Ing. Tech.* **82** (2010) 1059-1073.

[7]. I. Goikoetxea, J.I. Juaristi, R. Díez Muiño, M. Alducin, *Phys. Rev. Lett.* **113** (2014) 066103 1-5.

[8]. V.K. Díez, C.R. Apesteguía, J.I. Di Cosim, *Lat. Am. Appl. Res.* **33** (2003) 79–86.

[9]. L.K. Brar, G. Singla, N. Kaur, O.P. Pandey, *J Therm Anal Calorim*. **119** (2015) 175-182.

CHAPTER 7
HER Electro Chemical Measurements

Overview

Hydrogen Evolution Reaction (HER) is an important reaction both for environment friendly production of hydrogen by water splitting as well as for fuel cells. The development of high performance electro catalyst which can replace or reduce the loading of Pt in HER is of paramount importance. The TMCs have emerged as good candidates for the replacement of Pt showing advantages in terms of activity, selectivity and resistance to poisoning w.r.t. their parent metals. Various parameters which affect the final performance of TMCs are size, strain, lattice carbon content as well as the surface condition of the particles. In the present work TaC is used as a model system to delineate the effects of various parameters such as lattice carbon content of the powders (***x***, in TaC_x), strain, initial carbon concentration (C) and phase purity on HER performance of TMCs.

7.1 Hydrogen evolution reaction

Clean energy sources and utilization efficiency improvement of the available resources is the need of the hour to sustain long term growth of the society. Electrochemical energy storage is the most common method used in energy storage devices for clean energy. The main devices utilized for this are the fuel cells and various other electrochemical energy storage devices such as supercapacitors etc. [1]. The fuel cells have also emerged as one of the main contenders for fulfilling the power needs of the future due to their ability to: use clean fuels, deliver higher efficiency than Carnot cycle devices, low emissions and high performance [1, 2]. A fuel cell converts chemical energy of the 'fuel' into electrical energy. Among the low temperature fuel cells hydrogen and methanol are the most popular fuels for the anode with the oxygen and/or air being supplied to the cathode. Hydrogen with its compatibility with the CO_2 emission free electrochemical process as well as highest gravimetric energy density is an attractive choice for future fuel applications [3]. The requirement for high activity at low temperatures and the highly acidic conditions limit the electro catalysts which can be used in fuel cells to noble metals such as Pt and Ru, which in turn increases the cost. The reduction of Pt loading or its replacement with low cost, high performance and stable material is very important for ensuring an increase in the practical usage of the fuel cells. Within the fuel cell the oxygen-reduction reaction (ORR)/hydrogen-evolution reaction (HER) occur at cathode and the hydrogen oxidation reaction (HOR)/oxygen evolution reaction (OER) occur at anode. The cathode electro catalyst reactions have slower reaction kinetics and hence cathode has larger amount of Pt as compared to anode. So the new technological developments for the cathodic electrocatlyst will be more impactful [2]. Apart from the fuel cells hydrogen evolution reaction (HER, $2H^+ + 2e \rightarrow H_2$) is also important for production of hydrogen from water in an environment friendly way.

The HER in acidic aqueous medium occurs through the following steps [1,3,4]:

Discharge step/Volmer Reaction: An intermediate state of hydrogen atom is generated by transfer of an electron to the proton at the catalyst surface on the cathode:

$$H^+(aq) + e^- \rightarrow H_{ads} \qquad (7.1)$$

Volmer Reaction is followed by either Electrochemical desorption step (Heyrovsky´s reaction) or Proton recombination (Tafel recombination reaction).

Electrochemical desorption step/ Heyrovsky´s reaction:

$$H_{ads} + H^+(aq) + e^- \rightarrow H_2(g) \quad (7.2)$$

Proton recombination/Tafel recombination reaction:

$$H_{ads} + H_{ads} \rightarrow H_2(g) \quad (7.3)$$

Tafel slope is used as an indicator to determine the rate determining step for the given system. The Tafel slopes for above three reactions are 116 mV/dec, 40 mV/dec and 30 mV/dec respectively. A good HER electro catalyst has small Tafel slope and large exchange current density.

7.2 Transition metal carbides for HER applications

For HER catalyst the activation energy is decreased due to interaction between the d band situated at the Fermi level with the adsorbate and broadening of its valence orbital. As discussed earlier (chapter 1) the presence of carbon in the interstitial spaces modifies the band structure of the transition metal carbides (TMCs) and makes them suitable for applications as HER catalysts. In addition, TMCs also show advantages in terms of activity, selectivity and resistance to poisoning w.r.t. their parent metals. Over the years large amount of work has been done in characterization and optimization of TMCs for HER activity, as catalyst and also as catalyst support materials [1-3].

One of the well documented important parameter that has emerged while evaluating the performance of TMCs for HER is the requirement for large specific surface area per unit volume. This is achieved by using nano-sized, mesoporus samples [1,3]. Apart from specific surface area, the catalytic properties of the TMCs are strongly dependent on the location of the d-band which in turn is dependent on the amount of carbon present within the particles as well as the strain in the system [5-7]. Any modification in these parameters should reflect in the HER behaviour of the material. Since catalytic behaviour is a surface phenomenon so the condition of the surface also plays an important role in determining the final catalytic properties [8]. This includes any external carbon available on the outside of particles [9]. TaC is an interstitial TMC and can exist at various stable sub stoichiometric compositions as TaC_x. This means that TaC can be used as model system to study and delineate the effects of various parameters which affect the HER performance for TMCs. This will help to design the

better electro catalysts for future use. Many studies of the TaC HER catalytic activity are available [4,8-11]. In some of the papers the authors have discussed the effect of parameters such as surface composition and lattice carbon content (***x***). but in all the literature available at a given time only one parameter has been discussed while no attention has been paid to the variation of other parameters across the samples [8].

In this chapter the results obtained for the electrocatalytic HER experiments of selected nano TaC samples synthesized from Ta_2O_5, $TaCl_5$ and Ta-E are presented. The synthesis and characterization of these samples have been discussed in earlier chapters. The samples for the present study were selected based on the need to delineate the effects of different parameters such as lattice carbon content within the TaC particles (***x***), strain present in the samples and initial carbon (C) concentration of the samples. All these parameters have very strong effect on the electrochemical properties. In the present study the effects of these parameters on HER has been evaluated in an individual manner.

Table 7.1: Details of the samples analysed for HER catalytic behaviour.

Sample Code	**Precursor**	**Size (nm)**	**Initial C conc.**	***x*** **(lattice C content)**	**Strain ($\times 10^{-3}$)**	**Tafel slope (mV/dec)**	**j (mA/cm^2)**
A / Ox02T	Ta_2O_5	6.3	3	0.95	3.14	158	0.366
B / Ox15T	Ta_2O_5	6.2	3	0.99	4.10	147	0.514
C / Ox03C	Ta_2O_5	7.4	3	0.95	1.34	258	0.084
D / Ox15C	Ta_2O_5	6.2	15	0.99	4.34	125	4.400
E / Ox90C	Ta_2O_5	7.5	90	0.98	4.31	140	2.055
F / Ox07T	Ta_2O_5	5.1	3	0.99	14.45	150	0.351
G / Cl01h800	$TaCl_5$	2.8	3	0.95	5.69	148	0.178
H / Cl02h800	$TaCl_5$	3.1	3	0.97	7.15	150	0.728
I / Cl05h800	$TaCl_5$	3.2	3	0.97	16.3	160	0.935
J / Cl12h700	$TaCl_5$	4.3	3	0.89	14.5	137	0.721
K / E10h8	Ta-E	45	10	1	6.5	261	0.185
L / E08h8	Ta-E	21	10	0.99	1.1	154	1.099

7.3 Results and discussion

Figure 7.1 gives some of the CV curves obtained for sample **L** (Table 7.1) for 30 successive cycles. This data is a typical representation of data obtained for all the samples. The curves

obtained do not change appreciably after 10th cycle. The polarization curves used for analysis are taken after the stabilization. The higher over potential Tafel slopes and the current densities (obtained at -0.6V) for the HER experiments are listed in Table 7.1 along with the precursor, size, amount of initial carbon (C), carbon content within the TaC lattice (***x***, TaC_x) and strain for the analysed samples. The values for Tafel slope and over potential are comparable with those available in literature for TaC [4]. These values clearly indicate that the rate limiting step for HER in this case is the Volmer reaction (equation 7.1) [4,9]. For the Ta-E samples the initial C concentration has been calculated from the empirical formula. No external carbon source has been used in this case (Chapter 4).

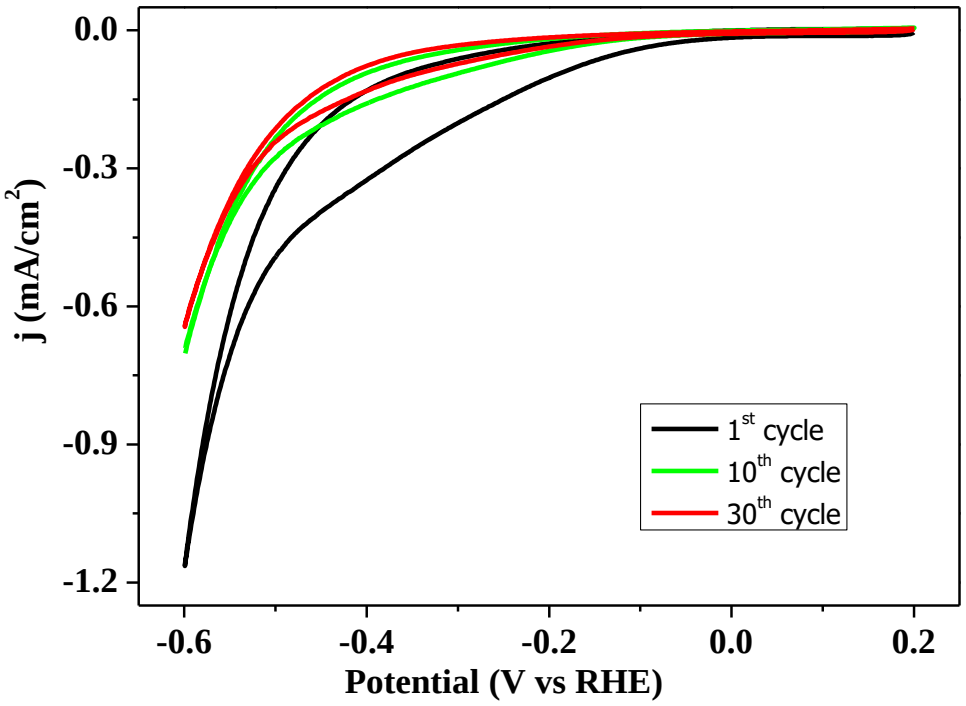

Figure 7.1: The CV curves obtained for sample **L**.

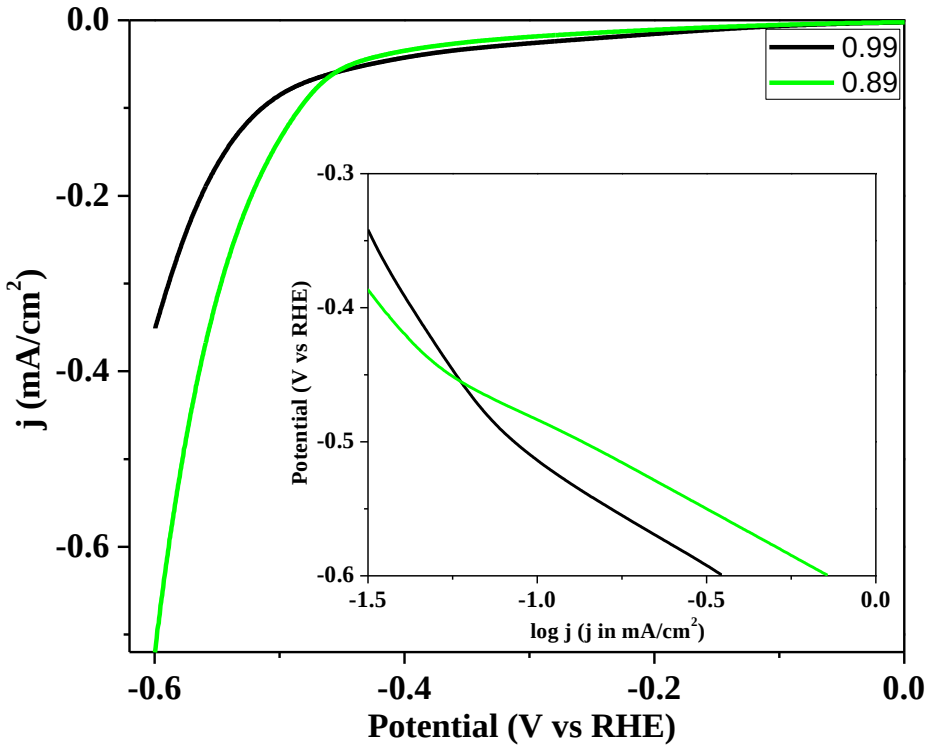

Figure 7.2: The polarization curves for samples **F** (***x*** = 0.99) and **J** (***x*** = 0.89) showing the effect of lattice carbon content on HER activity of TaC. Inset shows the Tafel slope curves.

7.3.1 Effect of lattice carbon content

To check the effect of lattice carbon content, ***x***, of the samples on HER the polarization curves for two samples **F** (***x*** = 0.99) and **J** (***x*** = 0.89) synthesized from different precursors having same initial carbon concentration (for the reaction) and similar strains and sizes were compared (Figure 7.2). The results clearly show that the samples with lower lattice carbon content (***x***) and hence more carbon vacancies have lower Tafel slope and higher current densities indicating faster reaction kinetics. These results are in tune with the earlier reports that sub stoichiometric TaC_x, with more carbon vacancies, shows increased catalytic adsorption properties [8]. The increase in Tafel slope for higher ***x*** indicates that for higher lattice carbon content the hydrogen absorption is becoming the rate limiting step. The increased adsorption of hydrogen for sub-stoichiometric TaC_x is a clear support for the earlier reported conjecture that charge transfer from tantalum 5d to carbon 2p states which results in enhanced hydrogen adsorption (Pt like properties) is dependent on sub-stoichiometric carbon content within the lattice [8].

7.3.2 Effect of strain

To study the effect of strain on the HER reaction we chose samples having nearly same size (within XRD error limit), lattice carbon content (***x***) and same initial carbon concentration for the synthesis. Figure 7.3 (a) and (b) depict polarization curves showing the effects of strain for two different sets of samples (**A**, **B** and **G**, **H**, **I**). The curves show that current is suppressed for the low strained samples. As the strain decreases the suppression increases. The Tafel slope curves indicate that even though the increasing strain limits the hydrogen adsorption but it also lowers the over potential values resulting in overall favourable effect on the HER activity .

This result is in accordance with the literature available for TMCs that the gas adsorption properties as well as the surface electronic properties are affected by strain [12,13] and that for early transition metals like Ta the tensile strain leads to a down shift of the d-band centre resulting in decreased interaction with the adsorbates [14]. It is believed that for the strained samples the enhanced current densities are result of enhanced surface reactivity as indicated by lower overpotential values.

7.3.3 Effect of initial carbon concentration

Samples **C**, **D** and **E**, are used to compare the effect of initial carbon concentration on the electro catalytic properties of the final samples for HER. The polarization curves (Figure 7.4) show that increasing the initial C concentration results in lowering of overpotential values as well as an enhancement of the final current densities. Table 7.1 shows that for sample C the combination of low strain and low initial carbon results in it being unusable for HER. Comparing with data obtained for samples A and B clearly shows that strain is an important parameter for determining the HER activity of the samples. Another interesting result which emerges is that sample **D** having lower initial C in comparison with sample **E** still has lower over potential, more current density and lower Tafel slope. It is believed that this is a result of the change in the nature of interaction between the graphitic network and the TaC nanoparticles in samples **D** and **E**. This conjecture is supported by our earlier results (Chapter 5) where we have shown that at very high initial C concentration (>15) further addition of C results in enhancement of graphitic network. This large graphitic layer maybe supressing the interaction of TaC with the surrounding liquid for sample **E**.

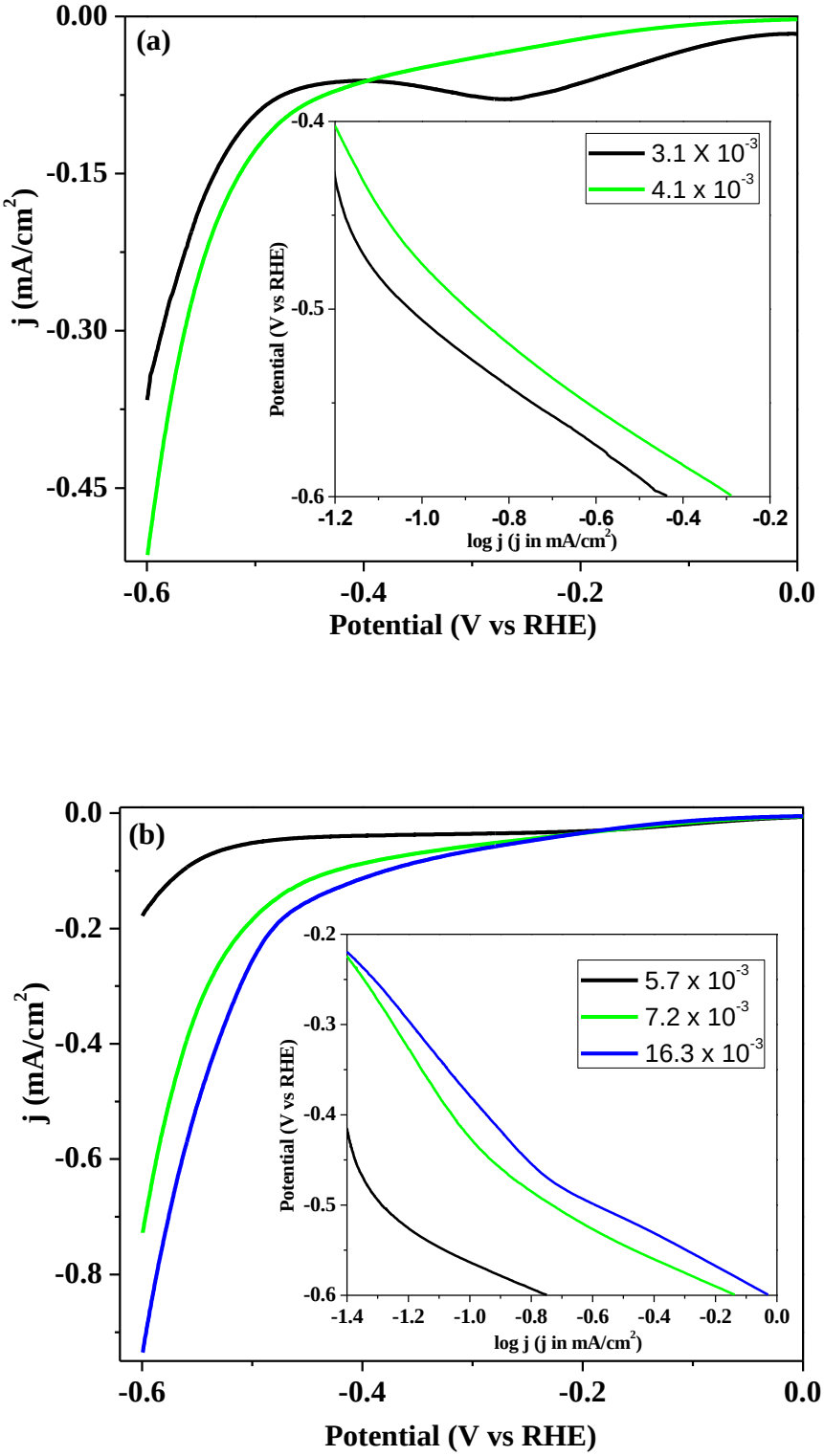

Figure 7.3: The polarization curves showing the effect of strain for samples synthesized from (a) Ta_2O_5 and (b) $TaCl_5$. Insets show the Tafel slope curves.

These results are very significant in highlighting the importance of initial C concentration used for the synthesis of TaC and also the nature of interaction between the nano TaC and the external C in the final product for deciding the HER properties. It is believed that the carbon network and TaC are synergistically connected leading to enhanced HER performance. These synergetic effects arise for the samples since the synthesis of TaC in the present system happens within the carbon network formed due to acetone decomposition [15]. The synergistic effects of as formed nano-systems with graphite are well documented [9, 16-18]. The exact nature of the TaC and graphitic network interactions needs to be studied further for our samples.

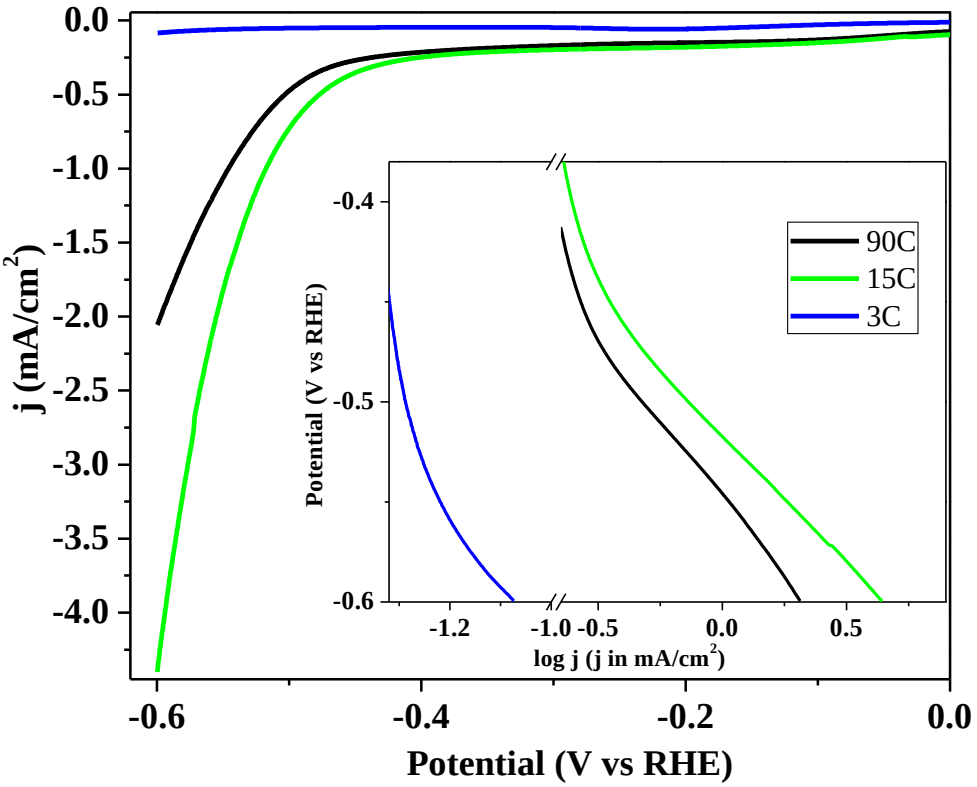

Figure 7.4: The polarization curves showing the effects of initial C concentration for the samples synthesized form Ta_2O_5. Inset shows the Tafel slope curves.

7.3.4 Effect of phase purity and sample particle size

Samples **K** (single phase, TaC, 45 nm) and **L** (mixed phase, 21 nm) have been compared to determine the effect of the phase purity and particle size of the samples on HER. The polarization curves clearly show that the small sized sample **L** has much higher current

density as well lower over potential value in spite of the low strain values. Sample **K** in spite of pure phase, high initial carbon and high strain does not have a HER activity due to its larger size (Table 7.1).

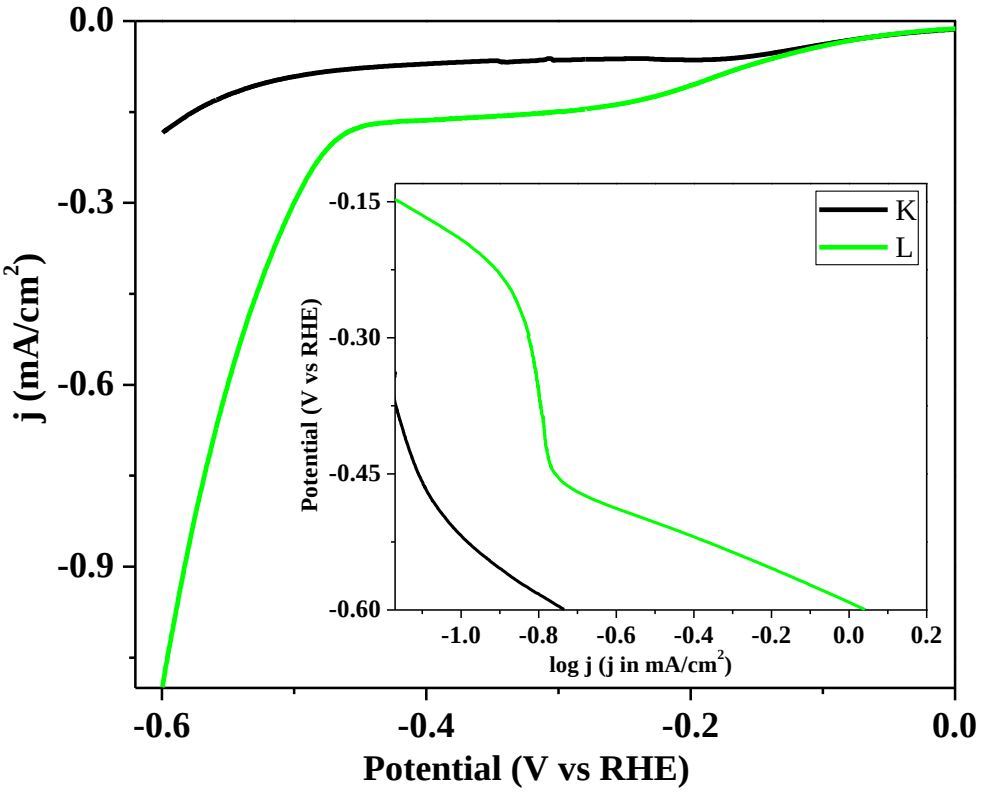

Figure 7.5: The polarization curves showing the effect of phase purity and sample particle size on the HER. Inset shows the Tafel slope curves.

The electrocatalytic activity of TaC is strongly dependent on the carbon content of the powders; inside the lattice as well as outside. The increase in latter strongly affects the current density by increasing it many fold whereas the low carbon content in the TaC lattice is more favourable for HER. Also, high strain as well small sized samples show enhanced activity for HER.

References:

[1]. Y. Zhong , X. Xia, F. Shi , J. Zhan , J. Tu, H.J. Fan, Adv. Sci. 2016, **3**, 1500286 1-28.

[2]. D.J. Ham, J.S. Lee, *Energies* **2** (2009) 873-899.

[3]. W.-F. Chen, J. T. Muckerman, E.Fujita, *Chem. Commun*. **49** (2013) 8896-8909.

[4]. N.S. Alhajri, H. Yoshida, D.H. Anjum, A.T. Garcia-Esparza, J. Kubota, K. Domend, K. Takanabe, *J. Mater. Chem., A* **1** (2013) 12606-12616.

[5]. H.O. Pierson, *Handbook of refractory carbides and nitrides*, Noyes Publications, New Jersey, USA (1996).

[6]. A.I. Gusev, A.A. Rempel, A.J. Magerl, *Disorder and Order in Strongly Nonstoichiometric Compounds - Transition metal carbides, nitrides and oxides*, Springer-Verlag Berlin Heidelberg, New York, USA (2001).

[7]. S. V. Didziulis, K.D. Butcher *Coord. Chem. Rev.* **257** (2013) 93– 109.

[8]. J.-G. Choi, *J. Porous. Mater.* **20** (2013) 1059-1068.

[9]. C. He, J. Tao, *Chem. Commun.* **52** (2016) 8810-8813.

[10]. E.J. Rees, K. Essaki, C.D.A. Brady, G.T. Burstein, *J. Power Sources* **188** (2009) 75-81.

[11]. D.M. Li, R. Hernberg, T. Mantyla, *Diamond Relat. Mater.* **7** (1998) 1709-1713.

[12]. P. Jakob, M. Gsell, D. Menzel, *J. Chem. Phys.* **114** (2001) 10075-10085.

[13]. D.I. Bazhanov, I.V. Mutigullin, A.A. Knizhnik, B.V. Potapkin, A.A. Bagaturyants, L.R.C. Fonseca, M.W. Stoker, J. Appl. Phys. **107** (2010) 083521 1-6.

[14]. Sebastian Schnur, Axel Groß, Phys. Rev. B **81** (2010) 033402 1-4.

[15]. L.K. Brar, G. Singla, O.P. Pandey *RSC Adv.* **6** (2016) 109174-84.

[16]. N.M. Julkapli, S. Bagheri, *Int. J. Hydrogen Energy* **40** (2015) 948-979.

[17]. Y.Li, H.Wang, L. Xie, Y. Liang, G. Hong, H.Dai, *J. Am. Chem. Soc.* **133** (2011) 7296–7299.

[18]. B.Wang, G.Wang, H.Wang, *J. Mater. Chem., A* **3** (2015) 17403–17411.

CHAPTER 8

Conclusions and Future Scope

Overview

This chapter summarizes the work done on the synthesis of TaC_x nano powders using different Ta precursors, viz., tantalum ethoxide, tantalum oxide and tantalum chloride. The evolution of the TaC_x with variation in precursors as well as the reaction conditions like the temperature, time and initial carbon concentration has been characterized using different techniques: XRD, DSC/TGA, BET, FE-SEM and TEM. The role of strain, lattice carbon content, external carbonaceous content and phase purity on the HER electrochemical performance of the synthesized carbides is summarized and concluded in this chapter. At the end, the future scope of this work is also presented.

8.1 Conclusions

TaC is a group V interstitial transition metal carbide (ITMC) which finds applications in diverse fields such as: ultra-high temperature (UHT) structural applications, thermo mechanical applications and as a prospective electro catalyst material for hydrogen evolution reaction (HER). The synthesis of pure phase nano TaC is of paramount importance for all the applications. TaC is strongly non-stoichiometric compound. Its properties are strongly dependent on size as well as the carbon content within the lattice (stoichiometric carbon content, ***x***, TaC_x). In order to prepare the samples of varying size and stoichiometry a number of experiments were performed using variety of precursors at different temperatures and reaction times. The following conclusions can be drawn from the work done in the present investigation.

Tantalum precursors are of paramount importance in determining the size and morphology of the final powders. The average size of the TaC powders synthesized from different Ta precursors in the present study is 40 nm (tantalum ethoxide), 8 nm (tantalum oxide) and 3 nm (tantalum chloride). This difference arises from the different thermal behaviour of the individual precursors under the reaction conditions inside the autoclave. Temperature as well as the holding time plays an important role in the final phase formation. TaC formation is a multistep process involving reduction to Ta followed by carburization to TaC. Initial reduction to tantalum using C and H_2 is a non spontaneous reaction. However, the addition of magnesium catalyses the reaction to proceed in the forward direction at low temperatures like 600 $^{\circ}$C or so. Carbon diffusion rate is the limiting parameter in the formation of TaC. The complete transformation can be achieved either by increasing the temperature or holding time. For all the samples the complete phase transformation to TaC has been achieved for a maximum temperature of 800 $^{\circ}$C. The time, temperature and transformation behaviour depends on the precursor used: 10 h (tantalum ethoxide), 1 h (tantalum oxide) and 1 h (tantalum chloride). For the tantalum chloride precursor the single phase TaC is also achieved at 650 $^{\circ}$C in 8 h. It was established using the thermal parameter calculations and experimental results that final conversion reactions are very fast and hence the formed TaC powders have high strain for the small synthesis time samples (1 h holding time). This strain is released by increasing the holding time. Once the strain is removed further heating results in grain growth. For the closed environment of autoclave the grain growth follows the simultaneous grain boundary migration and grain rotation model. Variation of strain in the TaC powders is

due to interplay of carbon content in the lattice of TaC and external carbonaceous content of the samples. While the former is decided by the holding time and temperature of the samples, the latter is a function of initial carbon concentration added in the synthesis mixture. Strain in the powders makes them thermally more unstable. For all the high strain samples the thermal oxidation occurs at lower temperatures. All the synthesized samples (irrespective of precursor) exhibit agglomerated morphology where the individual particles are coated with thin carbon layer which help in enhancing the electro catalytic activities as well as prevent coalescence of particles. Apart from the layered carbon coating of the individual TaC particles, it is observed that these particles are embedded in the graphitic network. The initial carbon in the synthesis mixture determines the external carbonaceous content of the final samples as well as the carbon content within the lattice of TaC. Analysis brought forward the prediction of the existence of the critical concentration of the initial carbon in the synthesis mixture (>5) which enhances diffusion of carbon into the TaC lattice.

The HER activity of the pure phase TaC_x synthesized using different Ta precursors has been measured and effects of different parameters have been delineated. The powders with smaller size have shown better electro catalytic performance. The amount of initial carbon used during synthesis modifies the HER performance of the final TaC powders. An increase in the initial carbon concentration results in decrease in Tafel slope, smaller overpotential and enhanced current density indicating that the interaction between that TMC particles and carbon is modifying the reaction kinetic pathways. For single phase powders having same size and external carbon content, the carbon content within the lattice and strain emerge as important parameters. Low lattice carbon content (x, TaC_x) and high strain samples show enhanced HER performance with high current density and low Tafel slope. The latter affects former so the two are not completely independent but particle strain also depends on the thermal history of the powders and so can be tailored. The carbon content of the TMCs cannot be decreased arbitrarily as the carbon vacancies also modify the energy band diagram for the material. So, the lower limit on the carbon content would be set by the variation of d band.

8.2 Future Scope

The present work demonstrates the possibility of synthesizing TaC at low temperature in single step from three different commercially available Ta precursors. The effects of time, temperature and carbon on the evolution of TaC have been studied. However, only one

carbon source has been used to obtain the samples. Other carbon sources, especially waste materials like agricultural waste or polythene etc, can be used to synthesize single phase nano sized TaC. This work has been planned and is being done for other carbides and can be extended for TaC also. Moreover the synthesis of TaC from the Ta ore can also be planned. The effects of different powder characteristics on HER activity of TaC have been studied. The ORR reactions also need to be studied. The synthesized powder can also be investigated further as a support material for HER as well as ORR reactions.